Laboratory studies of the self and cross reactions of atmospheric peroxy radicals

Thesis by

Aaron Craig Noell

In Partial Fulfillment of the Requirements
for the Degree of
Doctor of Philosophy

California Institute of Technology

Pasadena, CA

2010

(Defended November 18, 2009)

Acknowledgements

It has been a privilege and a pleasure to work with my advisors Stan Sander and Mitchio Okumura. Their insight, patience, and good humor made my time at JPL and Caltech immensely rewarding. They also attracted many other good people to work with them who have helped me in too many ways to count. Current and former Okumura group members Andrew Mollner, David Robichaud, Kana Takematsu, Laurence Yeung, Matt Sprague, Kathleen Spencer, and David Long all provided concrete help reading and editing my work at times, but more importantly they provided constant friendship and support. At JPL my postdoc mentor Leah Alconcel, and graduate student replacement Aileen Hui, both taught me a lot, and I am a better scientist for working with them both. For technical and spiritual help David Natzic could not be beat, and lunches without him will not be the same. Lance Christensen never tired of questions about work he did years ago, leaving me in his debt as well.

Working with Stan and Mitchio also means great collaborations with scientists outside their groups, and a large part of my thesis work was done this way. David Osborn and Craig Taatjes at Sandia National Lab were very generous in inviting me to work with them at the Advanced Light Source, and I am very thankful for that opportunity. Professor Fred Grieman from Pomona College spent his sabbatical at JPL, and working with him was one of the most productive and enjoyable periods of my time here. I am also grateful to the other members of my committee, Geoff Blake, Rudy Marcus, and Jack Beauchamp for seeing me through the major milestones of a chemistry department Ph.D.

Of course my friends and family are the ones who really made a good professional situation into a great situation period. Mom, Dad, and Cliff, I know your love is never far when I need it, even if I’m on the other side of the country. To my fellow TAs, my roomies, my quasi-roomies, my travelling buddies, my hanging out people, my ski bums, my beach bums, and my surfers: you all are wonderful.

Raquel, words are not enough, but your love has given a deeper meaning to my life, and makes me happy every day. Lastly, pequeñita, you are a very good motivator and my heart cannot wait to meet you.

Abstract

My studies focused on the self and cross reactions of peroxy radicals (RO_2). These are important gas phase reactions in the atmosphere when concentrations of nitrogen oxides are low. Hydroperoxide products of these reactions can undergo further reaction to form aerosol precursors, making RO_2 reactions critical to aerosol formation as well. The occurrence of multiple simultaneous reactions is frequently unavoidable when working with radical reactions. Self reactions of RO_2 further complicate matters by producing another peroxy radical (HO_2) through one of their product channels. Time resolved spectroscopic probes in the ultraviolet and near-infrared, specifically targeting each reactant, were used to measure the rate coefficients for the self and cross reactions of HO_2 and ethyl peroxy radicals ($C_2H_5O_2$). In addition the product branching fraction leading to HO_2 was determined for the $C_2H_5O_2$ self reaction with results very different from the literature.

Further work on the self reaction branching fractions of methyl peroxy, ethyl peroxy, and propyl peroxy was done to try and resolve the discrepancy with the literature. A photoionization mass spectrometry technique was used to monitor all of the stable reaction products on the timescale of the reaction. The literature work had used end product studies after the reactions had completed to measure all of the stable products. Results from the photoionization studies appear to agree with the spectroscopic work for the $C_2H_5O_2$ self reaction, indicating that additional secondary chemistry may have skewed the results in the literature.

Aerosol nucleation observed in low temperature experiments on the HO_2 self reaction was another area of work. Radical chemistry is the main driver of gas phase atmospheric cycles, but is not currently thought to be at the center of new particle formation. Radical-molecule complexes between HO_2 and a number of species including methanol, water, and acetone could act as particle seeds at low temperature due to the stability of their hydrogen bonds. Most of the nucleation work described is on the HO_2 - methanol complex, but all three were investigated. Lastly, the experimental calibrations and general procedures that went on throughout all this work are described.

Table of Contents

1 Introduction 1-1
1.1 A brief history and motivation 1-1
1.2 Thesis work 1-5
1.3 Challenges ahead 1-6
1.4 References 1-8

2 Near-IR kinetic spectroscopy (IR-KS) of the HO_2 and $C_2H_5O_2$ self and cross reactions 2-1
2.1 Introduction 2-1
2.2 Experimental 2-4
2.3 Results and analysis 2-10
2.4 Discussion 2-24
2.5 Conclusion 2-36
2.6 References 2-40

3 Peroxy radical self reactions studied by photoionization mass spectrometry 3-1
3.1 Introduction 3-1
3.2 Experimental 3-2
3.3 Results and analysis 3-9
3.4 Discussion 3-43
3.5 Conclusion 3-54
3.6 References 3-56

4 Photoinduced nucleation of low temperature hydroperoxy radical chemistry 4-1
4.1 Introduction 4-1
4.2 Experimental 4-3
4.3 Results 4-5
4.4 Discussion 4-17
4.5 Conclusion 4-20
4.6 References 4-22

5 Experimental work 5-1
5.1 Experimental setup 5-1

5.2 Absorption measurements 5-3

5.3 Pressure dependence of the HO_2 and RO_2 self reactions 5-13

5.4 Summary of path length, pressure dependence, and CH3OH effect 5-27

5.5 NIR probe 5-28

5.6 Sensitivity of UV and NIR probes 5-36

5.7 References 5-37

List of Figures

Chapter 2

Figure 2-1. (A)–(B) Example fit of NIR and UV data, respectively, for HO_2 + $C_2H_5O_2$ (C)–(D) Example fit of IR and UV data for the $C_2H_5O_2$ self reaction 2-13

Figure 2-2. Plot of k_2 vs. $[C_2H_2O_2]_0$ / $[HO_2]_0$ for T 221-296 K. Error bars are examples of data precision.. 2-15

Figure 2-3. (A)–(B) Fits to the NIR and UV data, respectively, for $C_2H_5O_2$ self reaction while holding α at three different values 2-16

Figure 2-4. Comparison of k_2 with previous work... 2-17

Figure 2-5. Comparison of k_{3obs} 2-20

Figure 2-6. Comparison of α with previous work. 2-22

Figure 2-7. Comparison of the fitted values for k_2 using either the previous recommendation for α or the value measured in this study. 2-25

Chapter 3

Figure 3-1. Schematic of experimental system. 3-3

Figure 3-2. Four stable products of the $C_2H_5O_2$ self reaction....................................... 3-13

Figure 3-3. (A) 1-D mass spectrum from the PIE data set. (B) PIE of acetaldehyde and ethene. (C) Mass contamination appears to have caused a discrepancy in the ethanol PIE. (D) PIE of ethyl hydroperoxide... 3-14

Figure 3-4. 1-D mass spectrum of four different pressures 3-15

Figure 3-5. Some of the unidentified products and their likely parents........................ 3-18

Figure 3-6. (A) Removing acetaldehyde mass contamination from m/z 45 PIE. (B) A comparison of the PIE curves for the larger masses and some of their possible dissociation products 3-19

Figure 3-7. Ratio of CH_3CHO counts to C_2H_5OH counts and α values 3-21

Figure 3-8. Ratios of [CH_3CHO] / [C_2H_5OOH] and [C_2H_5OH] / [C_2H_5OOH] 3-22

Figure 3-9. Expected products and reactants of $C_2H_5O_2$ self reaction using the DEK precursor chemistry 3-24

Figure 3-10. 1-D mass spectra from the DEK chemistry.. 3-25

Figure 3-11. Stable products of the 6 Torr, 248 nm, high O2 data set in Run 2........... 3-26

Figure 3-12. The 1-D mass spectra in the m/z 4X range from the four data sets taken during Run 2 3-27

Figure 3-13. m/z 90 was not observed in every data set in Run 2 3-28

Figure 3-14. *R* plotted for the four data sets of Run 2 3-30

Figure 3-15. The ratios [CH_3CHO] / [C_2H_5OOH] and [C_2H_5OH] / [C_2H_5OOH] for the four data sets in Run 2 3-32

Figure 3-16. Mass resolution in the 4X range for Run 3 3-34

Figure 3-17. The three major products -HCHO, CH_3OH, and CH_3OOH- along with the reactant CH_3O_2 from the methyl peroxy self reaction.................................... 3-35

Figure 3-18. PIE scan of major reactants and products for the CH_3O_2 self reaction..... 3-36

Figure 3-19. (A) Mass resolution of the major reactants and products was good. (B) *R* for the CH_3O_2 self reaction 3-37

Figure 3-20. Major products and reactants for $C_3H_7O_2$ self reaction using the OxCl precursor chemistry. 3-38

Figure 3-21. PIE of major products and reactants from $C_3H_7O_2$ self reaction using OxCl precursor chemistry. 3-40

Figure 3-22. Other masses of interest from the $C_3H_7O_2$ reaction using OxCl precursor chemistry. 3-41

Figure 3-23. Major products and reactants using DPK chemistry for $C_3H_7O_2$............. 3-42

Figure 3-24. PIE identification using DPK precursor chemistry for $C_3H_7O_2$............... 3-43

Figure 3-25. Comparison of α measurements 3-52

Chapter 4

Figure 4-1. UV absorbance from the HO_2 self reaction and the unexpected large absorbance at longer time scales. 4-6

Figure 4-2. Temperature dependence of the extinction in both the NIR and UV.......... 4-7

Figure 4-3. Dependence of the UV extinction on CH_3OH concentration.......... 4-8

Figure 4-4. Dependence of the peak UV extinction on $[CH_3OH]$ at three different initial radical concentrations.......... 4-9

Figure 4-5. Extinction in both the NIR and UV increases as a function of initial radical concentration. 4-10

Figure 4-6. Peak UV extinction as a function of initial radical concentration for various RH_{CH3OH}.......... 4-11

Figure 4-7. Comparison of extinction between the UV and NIR at higher $[HO_2]_0$. 4-12

Figure 4-8. Changing the chemistry of the nucleation to include $C_2H_5O_2$ provided some insight into the seed molecule 4-14

Figure 4-9. Greater extinction was observed in the absence of O_2, suggesting polymerization of the CH_2OH radical. 4-16

Chapter 5

Figure 5-1. IRKS apparatus. 5-1

Figure 5-2. Setup for penray lamp experiments.......... 5-5

Figure 5-3. Curvature in the absorbance plot for N_2O was seen when using the PMT with the bialkali photocathode, but not when using the Cs-I photocathode.......... 5-7

Figure 5-4. $[CH_3OH]$ measured by the Hg lamp agrees with the concentration determined by the flows when the bubbler pressure is above 300 Torr.......... 5-9

Figure 5-5. Initial radical dependence of the HO_2 self reaction in the UV. Low initial concentrations were influenced by other removal processes 5-14

Figure 5-6. Initial radical dependence of the HO_2 self reaction in the NIR.......... 5-15

Figure 5-7. Pressure dependence of k_{HO2} in both the UV and NIR compared with the literature value. 5-16

Figure 5-8. Pressure dependence of $k_{HO2}(UV)$ under conditions where no purge gas was used and the path length was fixed by the window - window distance. 5-17

Figure 5-9. RO_2 self reaction dependence on initial radical concentration. 5-19

Figure 5-10. Pressure dependence of $C_2H_5O_2$ self reaction did not change with or without the purge gas.. 5-21

Figure 5-11. A comparison of the different k_{HO2} values from the work in Chapter 2 depending on whether the UV, IR, or UV and IR together were fit. 5-24

Figure 5 12. Diagram of the wavelength modulation setup for the NIR diode laser..... 5-29

Figure 5 13. HO_2 spectrum after background ratio. 5-31

Figure 5 14. Baseline dip in HO_2 + HO_2 chemistry.. 5-33

Figure 5 15. DC signal from the detector after the excimer fires. 5-34

Figure 5 16. A signal is evident at the HO_2 frequency with only Cl_2 and O_2 present. A good baseline is also shown, determined by looking at its behavior while not on the HO_2 absorption line. 5-35

List of Tables

Chapter 2

Table 2-1. Chemical model used for fitting HO_2 and $C_2H_5O_2$ system of reactions....... 2-12

Table 2-2. Measured rate constant values for $HO_2 + C_2H_5O_2$ 2-18

Table 2-3. Summary of results for the $HO_2 + C_2H_5O_2$ reaction rate constant 2-18

Table 2-4. Results of $C_2H_5O_2$ self reaction at all temperatures and pressures 2-21

Table 2-5. Summary of experimental conditions for the determination of the $HO_2 + C_2H_5O_2$ reaction rate constant... 2-38

Table 2-6. Summary of previous experiments on $C_2H_5O_2 + C_2H_5O_2$ 2-39

Chapter 3

Table 3-1. All the reproducible masses identified in Runs 1A and 2 as well as their species assignment and a description of how their time trace appeared. 3-20

Table 3-2. Conditions and α values measured for each of the data sets in Run 2. 3-31

Chapter 5

Table 5-1. Summary of all the molecules and λ where absorption measurements were made. 5-5

Table 5-2. Path length measurements at different residence times, pressures, and amount of purge flow as a percentage of the total reactant flow. 5-10

Table 5-3. Simulation of purge effect on $k_{HO2}(UV)$. 5-26

1 Introduction

1.1 A brief history and motivation

Atmospheric chemistry has had a remarkably successful history given the scale and complexity of the subject. The foundation of that success lies in the synergy between the three branches of the field: Observational measurements, laboratory experiments, and atmospheric models. Each branch depends on and supports the other leading to a robust interwoven system for verification or dismissal of new hypotheses. The laboratory branch of atmospheric chemistry started to make significant progress in the 17th –19th centuries with the pneumatic chemists such as Antoine Lavoisier, Joseph Priestly, Daniel Rutherford, and Henry Cavendish. Cavendish was the first to recognize that air was made up of 1 part phlogisticated and 4 parts dephlogisticated air, i.e., ~20% oxygen (O_2) and ~ 80% nitrogen (N_2).[1] He was also able to identify another component that made up no more than 1/120 of the total volume. That component would later be identified as argon (Ar), an unknown element at the time. These major components of the atmosphere were all known early on, but it would be a while until the impact of trace species well beyond their small concentrations could be appreciated.

One of the next discoveries came in the late 19th and early 20th century with the discovery of the ozone (O_3) layer. Ozone absorption in the atmosphere was first proposed by William Hartley after his laboratory experiments on O_3 provided a candidate that matched the absorption in the atmosphere observed by Cornu.[2,3] Careful measurements and observations by Charles Fabry and Henri Buisson confirmed the assignment as well as estimated a thickness of the layer.[4] Lastly, Sydney Chapman developed the first model of how and where the O_3 formed in the atmosphere; the Chapman mechanism shown below is the first example of an atmospheric cycle.[5]

$$O_2 \xrightarrow{hv} 2O(\,^3P) \tag{1.1}$$

$$O(\,^3P) + O_2 \xrightarrow{M} O_3 \tag{1.2}$$

$$O_3 + O(\,^3P) \longrightarrow 2O_2 \tag{1.3}$$

Ozone would be more infamously discovered as one of the main photochemical components of atmospheric smog through the research of Arie Haagen-Smit in the 1940 – 50s.[6,7] This work combined observational studies of pollution effects on crops and rubber in the Los Angeles area, with laboratory studies to recreate the main component of the pollution.[8] Haagen-Smit's work was the first to recognize that the combination of trace hydrocarbons, nitrogen oxides, and light led to photochemical O_3 pollution.

The importance of stratospheric O_3 came to dominate the public's understanding of O_3 from the 1980s onward due to the observation and explanation of the polar stratospheric "ozone hole," through the combined efforts of all the branches of atmospheric science. The unraveling of the chemistry and dynamics involved in polar stratospheric O_3 loss combined with the political implementation of scientific recommendations remains one of the best examples of rigorous scientific work positively influencing public policy.[9,10]

At the same time work continued on understanding the mechanism for O_3 production in the troposphere. One irony of the field is that similar cycles determined to consume O_3 up in the stratosphere where it is beneficial to life, were determined to produce O_3 in the troposphere where it is hazardous to life. The central cycle to the production of O_3 in the troposphere is the coupling of NO_x (NO and NO_2) and odd oxygen (O_3 and $O(^3P)$) through reactions (1.4) – (1.6) and the Chapman mechanism.[11,12] Photolysis of NO_2 provides oxygen atom in its ground electronic state, O (^3P).

$$\mathrm{NO_2} \xrightarrow{hv} \mathrm{NO} + \mathrm{O}(\,^3\mathrm{P}) \tag{1.4}$$

$O(^3P)$ then forms O_3 through reaction (1.2) or a null cycle occurs if NO reacts with O_3 to reform NO_2.

$$\mathrm{NO} + \mathrm{O_3} \longrightarrow \mathrm{NO_2} + \mathrm{O_2} \tag{1.5}$$

Together these reactions during the daytime lead to a photostationary state O_3 concentration given by equation (1.6),

$$[\mathrm{O_3}] = \frac{j_{\mathrm{NO_2}}[\mathrm{NO_2}]}{k_{1.5}[\mathrm{NO}]} \tag{1.6}$$

where j_{NO2} is the first-order rate coefficient for photodissociation of $NO_{2.}$ The implication of equation (1.6) is that any production of NO_2 which does not come from reaction (1.5) will lead to a net production of O_3. Hydrocarbons (RH) and their resulting peroxy radicals (RO_2) form a critical link in smog formation by acting as oxidants to recycle NO back to NO_2 through reaction (1.7) without the consumption of O_3.

$$\mathrm{RO_2} + \mathrm{NO} \longrightarrow \mathrm{RO} + \mathrm{NO_2} \tag{1.7}$$

Alkoxy radicals (RO) formed in this reaction continue the cycle through further reactions.

$$\mathrm{RO} + \mathrm{O_2} \longrightarrow \mathrm{R'CHO} + \mathrm{HO_2} \tag{1.8}$$

$$\mathrm{HO_2} + \mathrm{NO} \longrightarrow \mathrm{OH} + \mathrm{NO_2} \tag{1.9}$$

Reformation of the hydroxyl radical (OH) in reaction (1.9) is important because OH is the initial oxidant that reacts with RH to create the RO_2.

$$\mathrm{OH} + \mathrm{RH} \longrightarrow \mathrm{R} \cdot + \mathrm{H_2O} \tag{1.10}$$

$$R\cdot + O_2 \xrightarrow{M} RO_2 \quad (1.11)$$

OH is initially formed in the troposphere by reaction of excited atomic oxygen O (^{1}D), from photolysis of O_3, with water vapor (H_2O).

$$O_3 \xrightarrow{hv < 300\,nm} O_2 + O(\,^1D) \quad (1.12)$$

$$O(\,^1D) + H_2O \longrightarrow 2OH \quad (1.13)$$

The flux of light reaching the troposphere at wavelengths less than 300 nm is small so the recycling of OH through the NO_x chemistry is critical to insuring that there are sufficient radicals to oxidize the RH emitted to the atmosphere.[13] In total, RH in the presence of NO_x and sunlight leads to the buildup of O_3 through the net reaction:[14,15]

$$RH + 4O_2 \longrightarrow H_2O + R'CHO + 2O_3 \quad (1.14)$$

The net scheme just described is one important end of many possible variants that have been systematically worked out through the complimentary efforts of all three branches of atmospheric chemistry. Much like the stratospheric work, but without the global treaty, this work collectively has led to government policy aimed at reducing pollution. Given the critical nature of RH for O_3 production initial pollution control efforts were directed at reducing RH emissions. However further work showed that an underestimation of the contribution of the biosphere to total RH had misled people into thinking that O_3 was limited by RH emissions. In fact when better measurements of the large biosphere contribution are used in the models it turns out that many areas of the country are limited by NO_x, despite the large concentrations emitted from automobiles, and stricter NO_x emission controls will be most effective in reducing O_3.[16-18]

These discoveries highlighted the need for better understanding of the RO_2 chemistry in the absence of NO_x; both in order to model the background troposphere where there is less anthropogenic influence, and also to understand the types and spatial extent of reactions that become important under NO_x-limited regimes.

1.2 Thesis work

The main focus of this work is laboratory studies of RO_2 reactions when no NO_x is present. Reaction with HO_2 (daytime mixing ratios of ~ 1–10 pptv)[19] is the dominant fate of RO_2 in the atmosphere at low NO_x.

$$\mathrm{RO_2 + HO_2 \longrightarrow ROOH + O_2} \tag{1.15}$$

The hydroperoxide products (ROOH) are reservoir species of reactive radicals. Removal of ROOH can occur by wet and dry deposition or participation in aerosol chemistry. Alternatively they can undergo photolysis or reaction with OH to recycle the radicals for further atmospheric reactions. Peroxy radical self reactions can also be important, especially the HO_2 self reaction forming another radical reservoir species.

$$\mathrm{HO_2 + HO_2 \xrightarrow{M} H_2O_2 + O_2} \tag{1.16}$$

$$\mathrm{RO_2 + RO_2 \longrightarrow products} \tag{1.17}$$

The RO_2 self reactions have much smaller rate coefficients so their individual reactions play less of a role in the atmosphere, but the sum total of all their reactions cannot be ignored. In laboratory experiments RO_2 self reactions are important to account for when studying the atmospherically important RO_2 + HO_2 reactions because of interfering secondary chemistry.

In Chapter 2 the HO_2 and $C_2H_5O_2$ system of reactions, (1.15) – (1.17), were investigated. Radical reactions are difficult to isolate leading to the almost inevitable difficulty of multiple reactions occurring at once. Self reactions of RO_2 further complicate matters by producing secondary HO_2 through one of their product channels. Time resolved spectroscopy specifically targeting each reactant was used to measure the rate coefficients for the self and cross reactions of HO_2 and $C_2H_5O_2$, as well as the product branching fraction of the $C_2H_5O_2$ self reaction responsible for the secondary HO_2. Chapter 3 looks further at self reactions of CH_3O_2, $C_2H_5O_2$, and $C_3H_7O_2$, but using a different experimental technique. Photoionization mass spectrometry was used to measure branching ratios for different product channels of these self reactions by monitoring all of the stable reactions products in time.

Nucleation observed in low temperature experiments on the HO_2 self reaction is the subject of Chapter 4. Radical chemistry is the main driver of gas phase atmospheric cycles, but is not currently thought to be at the center of new particle formation. Recently discovered radical-molecule complexes between HO_2 and a number of species, including methanol, water, and acetone, might be good candidates for particle seeds at low temperature due to the stability of their hydrogen bonds. Most of the nucleation work described is on the HO_2 – methanol complex, but all three were investigated. Lastly, Chapter 5 goes through the experimental calibrations and general procedures that went on throughout all this work.

1.3 Challenges ahead

While much is known about peroxy radical chemistry, some critical gaps in our knowledge remain. A recent field study in China was unable to model the observed distribution of HO_x between OH and HO_2, leading to the need for new laboratory experiments to shed light on reactions that could shift the predicted distribution.[20] Recent lab work has shown that other product channels of reaction (1.15), producing both OH and O_3, are important when the RO_2 contains a carbonyl functional group.[21,22] These reaction channels directly recycle the radicals without going through a reservoir species leading to a very different net reaction. Peroxy radical chemistry is also proving important in understanding secondary organic aerosol (SOA), a major influence on climate and health. Formation of SOA from isoprene, the largest non-methane hydrocarbon emitted to the atmosphere, is greater at low or no NO_x in laboratory experiments,[23] and epoxides formed in the OH oxidation of ROOH were determined to be the main source of the SOA growth.[24] The work showing this used detailed laboratory experiments to wrap up a mystery discovered by observational work done in areas with high isoprene emissions and unexplained HO_x chemistry. The growing importance of peroxy radical chemistry to SOA, the continued discovery of previously unknown gas phase reactions, and the discrepancies between models and observation show that there is still much to learn.

1.4 References

(1) Cavendish, H. *Philosophical Transactions of the Royal Society of London* **1784**, *74*, 119.

(2) Cornu, A. *Compt. Rend.* **1879**, *88*, 1101.

(3) Hartley, W. N. *Chemical News* **1880**, *42*, 268.

(4) Fabry, C.; Buisson, H. *Comptes Rendus Hebdomadaires Des Seances De L Academie Des Sciences* **1913**, *156*, 782.

(5) Chapman, S. *Quarterly Journal of the Royal Meteorological Society* **1932**, *58*, 11.

(6) Haagensmit, A. J. *Industrial and Engineering Chemistry* **1952**, *44*, 1342.

(7) Haagensmit, A. J.; Darley, E. F.; Zaitlin, M.; Hull, H.; Noble, W. *Plant Physiology* **1952**, *27*, 18.

(8) Pitts, J. N., Stephens, E.R. *Journal of the Air Pollution Control Association* **1978**, *28*, 516.

(9) The 1987 Montreal Protocol on Substances that Deplete the Ozone Layer; United Nations Environment Programme, O. S., Ed., 1987.

(10) Parson, E. *Protecting the ozone layer : science and strategy*; Oxford University Press: New York, 2003.

(11) Chameides, W. L.; Walker, J. C. G. *Journal of Geophysical Research* **1973**, *78*, 8751.

(12) Crutzen, P. *Pure and Applied Geophysics* **1973**, *106*, 1385.

(13) Jacob, D. J. *Introduction to Atmospheric Chemistry*; Princeton University Press: Princeton, 1999.

(14) Fishman, J.; Solomon, S.; Crutzen, P. J. *Tellus* **1979**, *31*, 432.

(15) Liu, S. C.; Trainer, M.; Fehsenfeld, F. C.; Parrish, D. D.; Williams, E. J.; Fahey, D. W.; Hubler, G.; Murphy, P. C. *Journal of Geophysical Research-Atmospheres* **1987**, *92*, 4191.

(16) Chameides, W. L.; Fehsenfeld, F.; Rodgers, M. O.; Cardelino, C.; Martinez, J.; Parrish, D.; Lonneman, W.; Lawson, D. R.; Rasmussen, R. A.; Zimmerman, P.; Greenberg, J.; Middleton, P.; Wang, T. *Journal of Geophysical Research-Atmospheres* **1992**, *97*, 6037.

(17) Sillman, S.; Logan, J. A.; Wofsy, S. C. *Journal of Geophysical Research-Atmospheres* **1990**, *95*, 1837.

(18) Trainer, M.; Williams, E. J.; Parrish, D. D.; Buhr, M. P.; Allwine, E. J.; Westberg, H. H.; Fehsenfeld, F. C.; Liu, S. C. *Nature* **1987**, *329*, 705.

(19) Seinfeld, J. H., Pandis, S.N. Atmospheric Chemistry and Physics; John Wiley and Sons: New York, 1998; pp 82.

(20) Hofzumahaus, A.; Rohrer, F.; Lu, K. D.; Bohn, B.; Brauers, T.; Chang, C. C.; Fuchs, H.; Holland, F.; Kita, K.; Kondo, Y.; Li, X.; Lou, S. R.; Shao, M.; Zeng, L. M.; Wahner, A.; Zhang, Y. H. *Science* **2009**, *324*, 1702.

(21) Dillon, T. J.; Crowley, J. N. *Atmospheric Chemistry and Physics* **2008**, *8,* 4877.

(22) Hasson, A. S.; Tyndall, G. S.; Orlando, J. J. *Journal of Physical Chemistry A* **2004**, *108*, 5979.

(23) Kroll, J. H.; Ng, N. L.; Murphy, S. M.; Flagan, R. C.; Seinfeld, J. H. *Environmental Science & Technology* **2006**, *40*, 1869.

(24) Paulot, F.; Crounse, J. D.; Kjaergaard, H. G.; Kurten, A.; St Clair, J. M.; Seinfeld, J. H.; Wennberg, P. O. *Science* **2009**, *325*, 730.

2 Near-IR kinetic spectroscopy (IR-KS) of the HO_2 and $C_2H_5O_2$ self and cross Reactions

2.1 Introduction

The chemistry of alkyl peroxy radicals (RO_2), introduced in Chapter 1, is central to the oxidation of volatile organic compounds (VOCs) in the atmosphere. In the troposphere RO_2 react primarily under two different regimes: high NO_x and low NO_x. Under the high NO_x conditions of urban air RO_2 chemistry contributes to regional air pollution problems by producing O_3. In the unpolluted troposphere (NO_x < ~20 pptv) the primary loss pathways for RO_2 radicals are self reaction and cross reaction with HO_2. These reactions lead to the production of organic hydroperoxides (ROOH), which are a temporary reservoir for HO_x. The net effect is to slow down or eliminate the production of O_3 from RO_2 chemistry.[1,2]

Ethane is one of the most abundant non methane hydrocarbons with a globally averaged annual concentration of ~ 1 ppb.[3] The ethyl peroxy radical ($C_2H_5O_2$) is formed in the atmosphere predominantly from the oxidation of ethane.

$$\mathrm{C_2H_6 + OH \xrightarrow{O_2} C_2H_5O_2} \tag{2.1}$$

In the remote troposphere the dominant loss process will be reaction with HO_2,

$$\mathrm{C_2H_5O_2 + HO_2 \longrightarrow C_2H_5OOH + O_2} \tag{2.2}$$

which leads to the formation of ethyl hydroperoxide (C_2H_5OOH). The concentrations of both $C_2H_5O_2$ and HO_2 also depend on their self reactions.

$$\mathrm{C_2H_5O_2 + C_2H_5O_2 \longrightarrow products} \tag{2.3}$$

$$\mathrm{\longrightarrow C_2H_5O + C_2H_5O + O_2} \tag{2.3a}$$

$$\longrightarrow C_2H_5OH + CH_3CHO + O_2 \qquad (2.3b)$$

$$\longrightarrow C_2H_5OOC_2H_5 + O_2 \qquad (2.3c)$$

$$C_2H_5O + O_2 \longrightarrow HO_2 + CH_3CHO \qquad (2.4)$$

$$HO_2 + HO_2 \xrightarrow{M} HOOH + O_2 \qquad (2.5)$$

Reaction (2.4) is a critical link because it leads to the generation of secondary HO_2. This recycles radicals in the atmosphere, and complicates laboratory kinetics experiments. The competition between the self, (2.3) and (2.5), and cross (2.2) reactions means that a pseudo-first-order kinetics experiment is not possible when trying to measure the rate coefficient for reaction (2.2), k_2, and that no analytic solution to the kinetics equations for the reaction exist.

There have been a number of studies of the kinetics[4-9] and products[9-12] of reaction (2.2). All of the kinetics studies with the exception of Cattell et al.[5] and Raventos-Duran et al.[9] used UV absorption alone to monitor peroxy radicals. One problem with UV absorption is that all RO_2 radicals have overlapping broad absorption features arising from a $\pi \rightarrow \pi^*$ transition on the terminal oxygen atom. This overlap of the $C_2H_5O_2$ and HO_2 absorption bands increases the uncertainty of the derived rate coefficient(s). A second problem with UV absorption is that it is not a particularly sensitive method unless long path lengths are used (several meters). This limits the range of initial reaction ratios, $[HO_2]_0$ / $[C_2H_5O_2]_0$, that can be used to check for consistency in the kinetics model. A different complication that affected several of the previous temperature-dependent measurements is the use of CH_3OH as a precursor for HO_2.[6,7] It has been demonstrated in this lab and others that CH_3OH acts as a chaperone, leading to larger apparent HO_2 self reaction rate constants at low temperature.[12,13] The large variation in the reported range of $\frac{E_A}{R}$ (650-1250 K^{-1}), is evidence of the difficulties encountered by previous temperature-dependent studies. The product studies on reaction (2.2) were done with FTIR and chemical ionization mass spectrometry (CIMS), and they showed that C_2H_5OOH is the major product.

The self reaction kinetics of $C_2H_5O_2$ were also measured by a number of groups,[5,7,10,11,14-19] and separate product studies were completed to determine the branching ratios of the different channels.[11,14,20-22] The difficulty with studying reaction (2.3) is that the alkoxy products in (2.3a) can go on to produce secondary HO_2 by reaction (2.4). This secondary HO_2 will enhance the apparent rate of reaction (2.3). It is possible to determine the actual rate constant for reaction (2.3) from the observed if the branching fraction to the alkoxy channel α is known.[23]

$$k_3 = \frac{k_{3obs}}{1+\alpha} \tag{i}$$

$$\alpha = \frac{k_{3a}}{k_3} \tag{ii}$$

All of the previous kinetics experiments used UV absorption to measure k_{3obs} and used α from end product studies to determine k_3. The end product studies on reaction (2.3) are in fair agreement, but there has been no measurement of α below room temperature. There also has been no measurement of α by a direct observation of the nascent products.

This study aimed to overcome some of the difficulties in previous work by using two probes in different wavelength regions to characterize the above reactions. A near-infrared (NIR) probe measured HO_2 and an ultraviolet (UV) probe measured $C_2H_5O_2$. Experiments were done either focusing on (2.2) or (2.3). The rate coefficient k_2 was measured during experiments on (2.2). In the experiments focusing on reaction (2.3) UV detection of $C_2H_5O_2$ allowed for the determination of k_{3obs} similar to previous studies. In addition, the NIR measured the time profile of secondary HO_2 from reactions (2.3) and (2.4), allowing for real time determination of α and k_3 for the first time. The measurements made of each reaction were then used together to develop a self consistent description of the self and cross reactions of $C_2H_5O_2$ and HO_2.

2.2 Experimental

2.2.1 Summary

The experimental apparatus is discussed in Chapter 5, and has been given in full detail previously.[24] Briefly, the IRKS apparatus consisted of a flash photolysis flow cell coupled with two optical probes for time-resolved HO_2 and $C_2H_5O_2$ detection. An excimer laser created a column of radicals down the length of the ~ 2 m flow cell. $C_2H_5O_2$ was detected by UV absorption spectroscopy. The UV light from a deuterium lamp was coupled into the cell along the same path as the excimer but in a counter-propagating direction. A monochromator was used to select the desired wavelength from the light exiting the cell. HO_2 was detected at the overtone of its OH stretching vibration using NIR wavelength modulation (WM) spectroscopy. The NIR light was also coupled lengthwise but was slightly off axis compared to the excimer and deuterium lamp. The NIR beam begins above and ends below the deuterium and excimer beams, but makes 30 passes crossing through the photolysis region in a Herriott cell setup. Data acquisition was gated to the firing of the excimer, and data for both optical probes were recorded simultaneously. The data from both probes were then fit simultaneously to determine the desired kinetics parameters.

2.2.2 Apparatus and Detection Probes

The radical chemistry took place in a 175 cm long, 5 cm diameter reaction cell. The intersection of the reactant gases with the excimer laser defined the photolysis volume, 2 cm x 1 cm x 138 (159) cm. The gas flows were adjusted so that the residence time in the flow cell (typically 10–15 s) matched the interval between photolysis laser pulses. Photolysis of Cl_2 by a XeCl excimer laser (308 nm, 110 ± 15 mJ/pulse) led to the formation of HO_2 and $C_2H_5O_2$ by the reaction sequence,

$$\mathrm{Cl_2} + h\nu(308\ \mathrm{nm}) \longrightarrow 2\mathrm{Cl} \tag{2.6}$$

$$\mathrm{Cl} + \mathrm{CH_3OH} \longrightarrow \mathrm{CH_2OH} + \mathrm{HCl} \tag{2.7}$$

$$\mathrm{Cl} + \mathrm{C_2H_6} \longrightarrow \mathrm{C_2H_5} + \mathrm{HCl} \tag{2.8}$$

$$\mathrm{CH_2OH} + \mathrm{O_2} \longrightarrow \mathrm{HO_2} + \mathrm{HCHO} \tag{2.9}$$

$$\mathrm{C_2H_5} + \mathrm{O_2} \xrightarrow{\mathrm{M}} \mathrm{C_2H_5O_2} \tag{2.10}$$

For the experiments on the $C_2H_5O_2$ self reaction no CH_3OH was used, but there is a small source of HO_2 from the reaction that forms $C_2H_5O_2$.

$$\mathrm{C_2H_5} + \mathrm{O_2} \longrightarrow \mathrm{HO_2} + \mathrm{C_2H_4} \tag{2.11}$$

The HO_2 concentration resulting from reaction (2.11) is about 1% of the initial $C_2H_5O_2$. This value is in good agreement with previous work by Kaiser et al., but is slightly higher than new measurements by Clifford et al.[25-27]

The temperature in the cell was held to within ± 1 K of the stated temperatures. Methanol cooled by liquid nitrogen circulated through a jacket around the cell to obtain temperatures below 298 K. Calibrated flows of reagent gases were cooled and mixed in a 1 m long tube before flowing into the middle of the reaction cell. The temperature inside the cell was measured with a type T thermocouple (Omega). A purge flow was used to protect the NIR Herriott mirrors from corrosion and contain the main flow to the temperature-controlled region. The mixing of the purge flow and reactant gases occurred throughout 10 cm on either side of the cell leading to a path length of 148 ± 10 cm. A complete discussion of the purge and reactant gas mixing is given in Chapter 5.

Typical reagent gas concentrations were, in units of molecules cm^{-3}: Cl_2 = (0.3-1.5) × 10^{16}, He = (3-15) × 10^{16}, CH_3OH = (0–2.5) × 10^{15}, C_2H_6 = (0.5–30) × 10^{15}, O_2 = (5-20) × 10^{17}, N_2 = (0-1) × 10^{18}. The CH_3OH was carried into the cell by N_2 after it passed through the liquid CH_3OH (J.T. Baker, PHOTOREX® Reagent) in a bubbler held at 273 K. The experiments on the cross reaction (2.2) were performed in O_2. The $C_2H_5O_2$ self reaction (2.3) measurements were primarily in O_2 as well, but used N_2 as a buffer when investigating the effect of varying O_2 concentrations on α. All gas flows were monitored with mass flow meters (Hastings HFM-200 series) and controlled with needle valves. Sufficient concentrations of C_2H_6 and/or CH_3OH were always used to insure stochiometric conversion of Cl to $C_2H_5O_2$, HO_2 or both. In the experiments on (2.2) flows were adjusted to investigate the kinetics over a wide range of initial radical concentrations, i.e., different values of the initial radical ratio: $[HO_2]_0 / [C_2H_5O_2]_0$. This ratio typically ranged from 0.1–4 while the total concentration of radicals remained constant at ~ 1 x 10^{14} molecules cm^{-3}. For experiments on (2.3) the total radical concentration was varied, typically from 3.0 x 10^{13}– 1.5 x 10^{14} molecules cm^{-3}. At least six measurements were made spaced throughout the range of the initial radical ratio, or total radical concentration, at every temperature and pressure for (2.2) and (2.3), respectively. The pressures in the cell and the CH_3OH bubbler were monitored by capacitance manometers (MKS-220CA 1000 Torr), and were constant within ± 2 Torr of the stated pressures. Flow meters were calibrated by measuring the time required to flow through a calibrated volume over a range of flows suitable to each meter. The capacitance manometers were calibrated in reference to other factory calibrated capacitance manometers.

Two optical probes were used to monitor the radical chemistry. The UV light source was a 150 W deuterium lamp (Hamammatsu L1314). The beam made a single pass through the cell counter-propagating with the excimer photolysis beam. Baffles on either end of the reaction cell ensured that only light that had sampled the photolysis region entered the monochromator slit. The monochromator was set to 250.0 nm for detection of $C_2H_5O_2$. The minimum detectable absorbance for $C_2H_5O_2$ was ~ 2×10^{-5} $Hz^{-1/2}$ (~ 6×10^{12} molecules cm^{-3}). The monochromator was calibrated by looking at the atomic emission lines from a Hg pen lamp. The NIR probe source was a 3 mW distributed-feedback (DFB) continuous-wave tunable diode laser manufactured in the JPL Microdevices Laboratory. The laser was tuned for HO_2 at the $^{q}Q_2$ band head (6638.2 cm^{-1}) of the first overtone of the OH stretch.[28] The NIR beam made 30 passes through the reaction cell using a Herriott cell setup with an estimated effective path length of 2700 cm. The laser was frequency modulated at 6.8 MHz by varying the drive current with an external RF generator. The signal from the InGaAs photodiode detector (New Focus 1811) was demodulated at 13.6 MHz (2f detection) and subsequently amplified by a factor of 100. The minimum detectable absorbance for HO_2 was ~ 2×10^{-7} $Hz^{-1/2}$ (~ 1×10^{11} molecules cm^{-3}).

The detector signals for both optical probes were recorded simultaneously. The data acquisition was controlled by a Visual BASIC program. For reaction (2.2) the decay measurements typically began 1 ms before the excimer fired to establish a baseline for the signal, and continued for 20 ms at a sampling rate of 200 kS/s. For reaction (2.3) the baseline was recorded for 10 ms before the excimer pulse and continued for 200 ms at a sampling rate of 20 kS/s to capture the slower decay. Both signals were low pass filtered at 100 kHz and 10 kHz, respectively (SRS-SR560). The data was digitized using a two channel 16 bit per channel A/D card with a maximum sampling rate of 2.5 MS/s (Gage-CompuScope 1602). Decay traces for the UV and the IR probes were obtained by averaging the signals over 50 excimer shots.

2.2.3 Calibration of the NIR Probe

The NIR probe was calibrated daily to measure HO_2 because WM spectroscopy measures relative not absolute changes in concentration. The NIR probe was calibrated with the UV absorption probe by measuring the kinetics of the HO_2 self-reaction (2.5). The two probe beams measure the same physical processes, albeit with different geometrical overlap, but should yield the same bimolecular kinetics at short time scales (~ 20 ms). At the beginning of each day data for reaction (2.5) were taken while only HO_2 radicals were present. The UV monochromator was set to 220.0 nm to monitor HO_2 at the same as it was monitored by the NIR. The time decays of both probes were fit simultaneously with the kinetics modeling program FACSIMILE.[29] The fits checked for consistency between the probes, and determined that day's calibration factor for the NIR. The rate coefficient of the HO_2 self reaction k_5 used in the kinetic modeling of (2.2) and (2.3) was taken from these daily measurements as it was determined along with the value of the calibration factor for the NIR. This calibration factor was very sensitive to optical alignment, but in general was consistent from day to day within ± 15%. The UV detection wavelength was then optimized for $C_2H_5O_2$ detection to allow for the simultaneous independent detection of both radicals.

2.2.4 Diffusion

Diffusion was taken into account when modeling the data and comparing the two probes. For reactions that were complete in < 20 ms diffusion had a minimal effect, but all data was treated the same way. Different volumes of the reaction cell were sampled by the UV and NIR probes, and this led to different observed behavior from diffusion. UV modeling included an explicit loss term, but The NIR had offsetting effects that were not factored into the kinetics model. The UV was co-aligned with the excimer laser down the middle of the flow cell. The radicals created down the middle of the cell diffused radially out of the UV beam given sufficient time. This type of diffusion was approximated as a unimolecular loss term in the kinetic fits. By varying the initial concentration of total radicals and determining the observed bimolecular rate constant, the contribution of diffusion to the observed rate constant was determined in the manner of Thiebaud et al.[30] The NIR was complicated by the geometry of the Herriott cell. The NIR beam passed in and out of the photolysis region because of its off axis alignment with respect to the radicals. Diffusion allowed parts of the beam originally outside the photolysis region to interact with radicals and extend the path length. However the concentration profile along that path length was not uniform. The different concentrations underwent reaction at different rates. At longer times, as more and more of the beam passed through smaller concentrations of the radical, the bimolecular reaction rate appeared to have slowed down. This led to a small systematic residual in the IR signal. This effect on the overall error analysis will be discussed in the results and analysis section.

2.3 Results and analysis

2.3.1 Overview

Reactions (2.2) and (2.3) were the primary focus of this work. In order to achieve the greatest sensitivity to k_2 and k_3 one type of experiment was performed in which both HO_2 and $C_2H_5O_2$ were created deliberately, and another type where only $C_2H_5O_2$ was created deliberately. Both types of experiment were done using simultaneous NIR and UV probes of HO_2 and $C_2H_5O_2$, respectively. Perfect isolation of each reaction is not possible because they are connected by secondary chemistry, but one reaction or the other became the focus with the different experimental conditions. The rate coefficients k_2 and k_3 and the branching fraction α were measured in a self consistent manner. Correlation among the parameters was explored and accounted for throughout the data analysis.

2.3.2 Methods and Error Analysis

All three of the major kinetics parameters determined in this study – k_2, k_3, and α – could not be well determined at the same time. Unphysical values for the parameters were returned when all three were varied at once. Therefore it was necessary to follow an iterative procedure for fitting the data. First the NIR was calibrated with data from (2.5) as described in the experimental section on NIR calibration. Data for (2.2) with $[HO_2]_0 / [C_2H_5O_2]_0 > 1$ (typically 3 different conditions) were then fit in order to approximate k_2. Secondary chemistry from (2.3) does not interfere when HO_2 is in excess because k_2 is ~50 times larger than k_3, and almost all $C_2H_5O_2$ will react with HO_2. The estimate for k_2 was then used in fits of the (2.3) data to give values for k_3 and the branching fraction α.

The values for k_3 and α were then used to fit the rest of the (2.2) data where $[HO_2]_0$ / $[C_2H_5O_2]_0 < 1$. Under these conditions the secondary chemistry of (2.3) has an effect on the values obtained for k_2. A new value of k_2 was obtained by averaging the values from all of the fits of (2.2) data. This value of k_2 was then used in subsequent fits of data on reaction (2.3), and all of the values were refined iteratively. In practice two iterations were sufficient to achieve convergence. **Table 2-1** presents the full chemical model used while fitting the reactions and what parameters were fit. All fits were performed using the program FACSIMILE.[29]

Data fitting started at 200 μs after the photolysis laser pulse for both reactions. The (2.2) data were typically fit to 5–10 ms. The data for the slower (2.3) were fit out to two half lives (50–200 ms) in order to account for the varying values of $[C_2H_5O_2]_0$. In all fits the radical source chemistry was neglected and the initial radical concentrations $[HO_2]_0$ and $[C_2H_5O_2]_0$, were fit as well. The initial radical concentrations from the fits were consistent with the ratios of $[CH_3OH]$ and $[C_2H_6]$, the precursors of HO_2 and $C_2H_5O_2$, respectively.

Table 2-1. The chemical model used for fitting HO_2 and $C_2H_5O_2$ system of reactions

Reaction	k_{298}[a]	
$HO_2 + C_2H_5O_2 \longrightarrow C_2H_5OOH + O_2$	5.5×10^{-12}	k_2^{*}
$C_2H_5O_2 + C_2H_5O_2 \longrightarrow 2C_2H_5O_2 + O_2$	3.2×10^{-14}	k_{3a}^{*}
$\longrightarrow C_2H_5OH + CH_3CHO$	7.8×10^{-14}	k_{3b}^{*}
$C_2H_5O_2 + O_2 \longrightarrow HO_2 + CH_3CHO$	1.0×10^{-14}	$k_4^{\dagger}$
$HO_2 + HO_2 \xrightarrow{M} H_2O_2 + O_2$	1.7×10^{-12}	k_5^{*}
$C_2H_5O_2 + C_2H_5O \longrightarrow C_2H_5OOH + CH_3CHO$	1.5×10^{-11}	k_{12}^{*}
$C_2H_5O_2 \xrightarrow{\text{diffusion, UV}}$	$5\ s^{-1}$	k_D^{*}
$HO_2 \xrightarrow{\text{diffusion, UV}}$	$5\ s^{-1}$	$k_D^{\ddagger}$

[a] units of cm^3 $molecules^{-1}$ s^{-1} except where explicitly written, * determined during this study, † ref [31], ‡ used $C_2H_5O_2$ value

Sample fits with residuals for both (2.2) and (2.3) are shown in **Figure 2-1 A–D**. In **A** and **B** are the data and fits for (2.2) at 273 K, 50 Torr, and $[HO_2]_0 / [C_2H_5O_2]_0 = 1.13$ in the NIR and UV, respectively. The high signal-to-noise ratio for the HO_2 NIR signal reveals the subtle systematic residual attributed to diffusion and described in the calibration of the NIR probe portion of the experimental section. Panels **C** and **D** show the NIR and UV traces for reaction (2.3) taken at 273 K, 50 Torr, and 8.8×10^{13} molecules cm^{-3} total radicals. At the HO_2 concentrations in **C** (~100 times lower than **A**) the diffusion effect is masked by the signal noise. For both (2.2) and (2.3) the fits agree well with the UV and NIR signals.

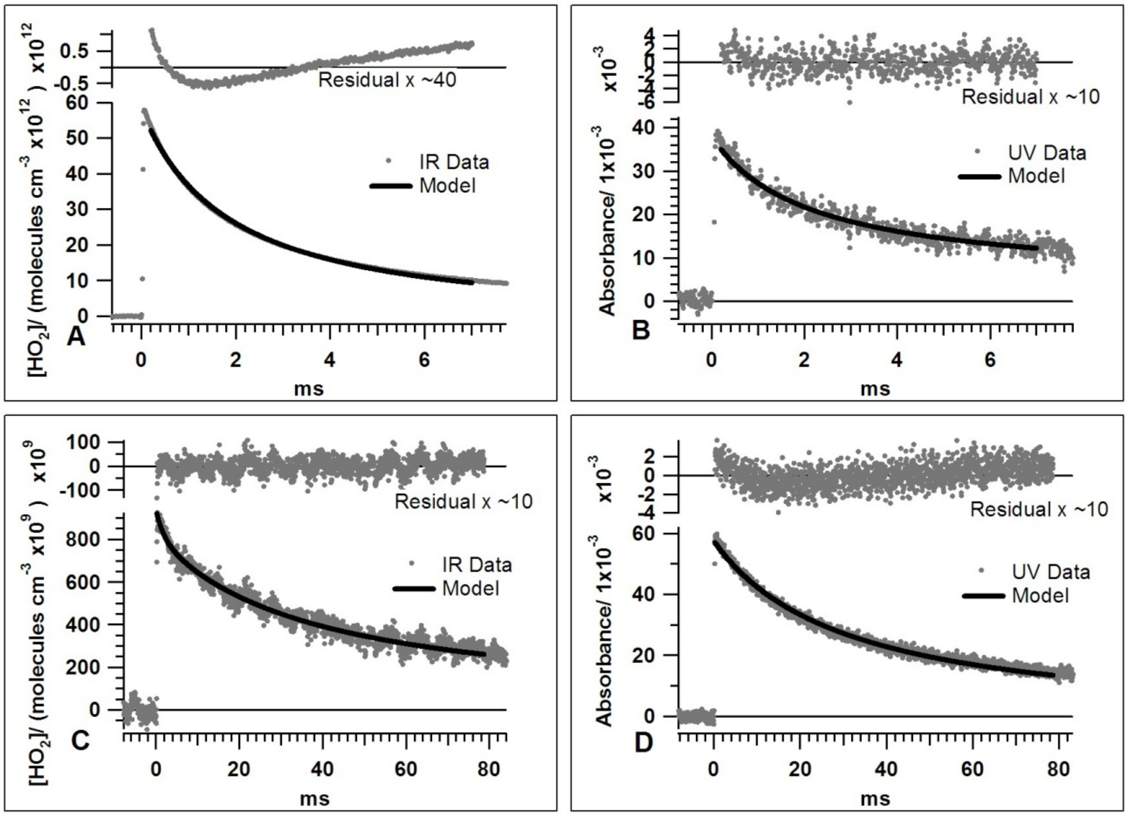

Figure 2-1. (A) Example fit of IR data for reaction (2.2). (B) Example fit of UV data for reaction (2.2). The data were taken at 273 K, 50 Torr, [CH_3OH] = 4 × 10^{15} molecules cm^{-3} and [$C_2H_5O_2$]$_0$ / [HO_2]$_0$ = 1.13. (C) Example fit of IR data for reaction (2.3). (D) Example fit of UV data for reaction (2.3). The data were taken at 273 K, 50 Torr, and [$C_2H_5O_2$]$_0$ = 8.8 x 10^{13} molecules cm^{-3}.

By setting the monochromator to 250.0 nm, the ratio of $C_2H_5O_2$ and HO_2 cross sections was maximized at ~ 10:1 ($C_2H_5O_2$: $\sigma = 4.1 \times 10^{-18}$ cm^2; HO_2: $\sigma = 0.48 \times 10^{-18}$ cm^2)[31] within the operating range of the lamp. The peroxide products of (2.2) and (2.5), C_2H_5OOH and HOOH, respectively, also absorb at 250 nm. The absorption cross section for C_2H_5OOH has not been measured, but was assumed to be the same as that for CH_3OOH. We make this assumption because the hydroperoxides all share a broad dissociative transition in the UV (210–365 nm) due to the breaking of the O-O bond.[32] While σ_{250} for HOOH and CH_3OOH vary by a factor of 2, the values for CH_3OOH and $HOCH_2OOH$ are virtually identical, suggesting that differences past the alpha atom will not have a large influence on σ. The values used for HOOH and C_2H_5OOH at 250 nm are $\sigma = 8.3 \times 10^{-20}$ and $\sigma = 3.98 \times 10^{-20}$ cm^2, respectively.[31]

The uncertainties stated in the following sections come from random error and systematic error. The random errors are accounted for in a straightforward way by determining the standard deviation from the mean. The mean was determined by averaging values of k_2, k_3, and α from runs at the same temperature and pressure but with different initial radical ratios or total radical concentrations, respectively. One potential source of systematic error was the uncertainty from the fitting procedure just described. In the initial fits to the data for (2.2) where $[HO_2]_0/[C_2H_5O_2]_0$ was high, the low signal-to-noise ratio in the UV detection of $C_2H_5O_2$ and the small systematic residual in the NIR detection of HO_2, led to a range of acceptable fits and a range in the value for k_2. The quality of the fits was determined by the overall residual sum of squares as well as by visual evidence of non-random residuals. The high and low values for k_2 were then propagated through the fitting routine in order to determine the effect of this uncertainty on the values of k_3 and α. The values of k_3 and α returned, but not the overall quality of the fits, relied on the value of k_2 used to fit them. This meant a wide range of k_2 values led to similarly high quality fits to the data from (2.3), but returned a proportionally wide variety in values for k_3 and α. The uncertainty in the k_2 fits and the correlating uncertainties in k_3 and α were smaller than the random uncertainties but not negligible. Both sources of error were combined in quadrature. An example of these 1 σ error bars at two temperatures for k_2 are shown in **Figure 2-2**, and show how the overall uncertainties get larger at $[HO_2]_0/[C_2H_5O_2]_0 > 1$ due to increased uncertainty in the fits.

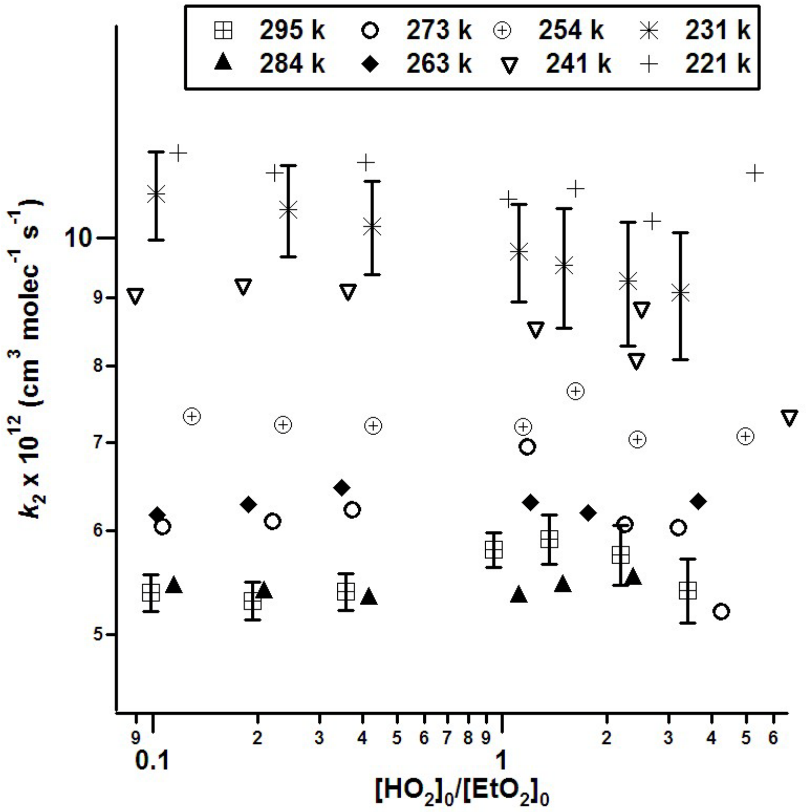

Figure 2-2. Plot of k_2 vs. $[C_2H_5O_2]_0$: $[HO_2]$ for T 221-296 K. Error bars are examples of data precision.

The major source of systematic error was the uncertainty in the path length due to the mixing of the purge and reactant gas flows. The data was analyzed at the maximum and minimum lengths, i.e., 138 and 159 cm, to determine the error associated with this uncertainty. Upper and lower error bounds were determined by applying the random and fitting uncertainties just discussed to the analysis done at the long and short path length. The total error determined in this way was considered a 2σ error bar. The final errors are reported as half this at their 1σ limits. These are the error bars displayed with data presented in **Figure 2-4**, **2-5**, and **2-6**, and in **Table 2-3** and **2-4**. The uncertainties do not take into account the error associated with σ for HO_2 and $C_2H_5O_2$ in the UV.

Another potential contributor to the error from reaction (2.3) is the correlation between parameters k_3 and α. Unlike the correlation between k_2, k_3, and α just described, k_3 and α are impossible to determine independently in this experiment. Fortunately the quality of the fit to the data degrades rapidly if k_3 or α is fixed away from their simultaneously fit values. This meant that the contribution to the overall error was much smaller than the random error and was not included. **Figure 2-3 A–B** compares fits that use the JPL-06 ($\alpha = 0.6$), the data fit ($\alpha = 0.28$), and an arbitrary lower value ($\alpha = 0.10$) for α, and provides an example of how fits to the data do not capture the behavior observed when k_3 and α are not fit simultaneously. The NIR HO_2 data in **A** shows clearly that the JPL-06 value for α predicts larger concentrations of HO_2 than are observed, and that the lower value predicts much lower concentrations. In **B** the fit to the UV data that largely determines k_3 shows a much slower rate constant for the JPL-06 and a faster one for the lower α value. **Figure 2-3** demonstrates that although k_3 and α are correlated, pulling one away from its best fit value also pulls the other away from its best fit.

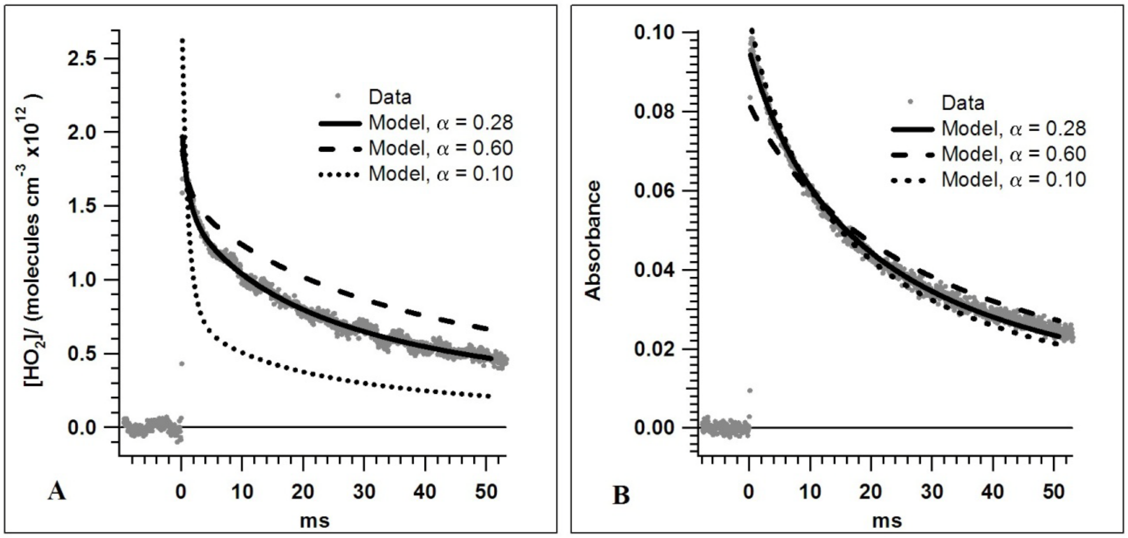

Figure 2-3. (A) Example of NIR data for reaction (2.3) while holding α at three different values, and the effect it produces on the fit. (B) The corresponding UV data.

2.3.3 $HO_2 + C_2H_5O_2$ rate constant

Measurements of the rate coefficient k_2 were performed over the temperature range 221–296 K and the pressure range 50–200 Torr. For each combination of temperature and pressure, the initial radical ratio ($[HO_2]_0 / [C_2H_5O_2]_0$) was varied over the range 0.1–3. The range of initial radical concentrations were as follows, in units of molecules cm^{-3}: $[HO_2]_0 = (0.1\text{-}1) \times 10^{14}$ and $[C_2H_5O_2]_0 = (0.3\text{-}1) \times 10^{14}$. **Figure 2-2** shows the values obtained for k_2 vs. $[HO_2]_0 / [C_2H_5O_2]_0$ at each temperature at a pressure of 50 Torr. For clarity error bars have only been included for 295 K and 231 K. **Figure 2-4** shows a comparison of the current work to previous studies at temperatures < 298 K.

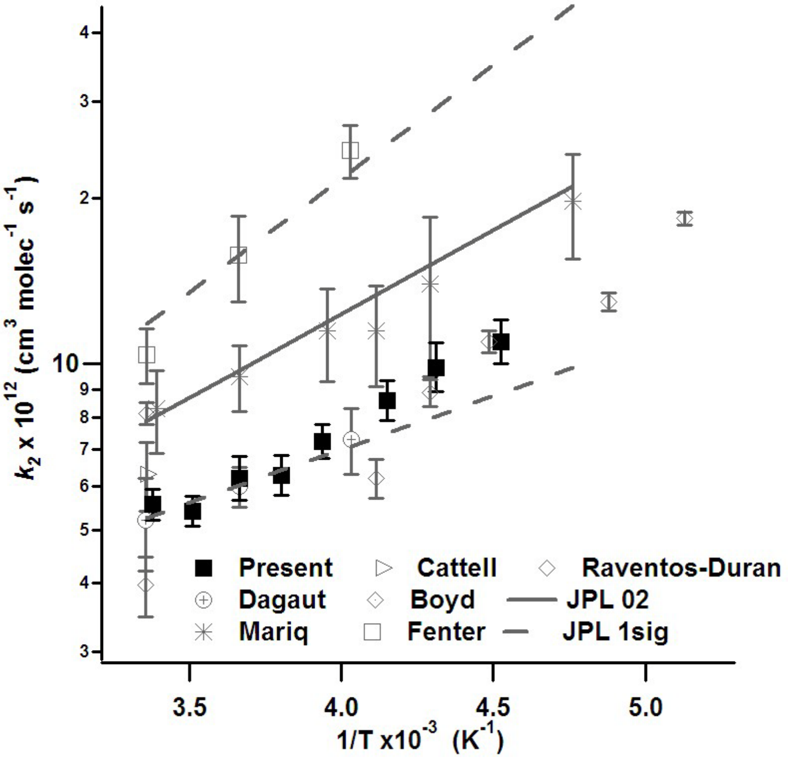

Figure 2-4. Comparison of k_2 with previous work. Error bars are 1σ.

Table 2-2 lists the values of k_2 measured in this study. The values of $k_2(298K)$ and the Arrhenius parameters for all of the studies are given in **Table 2-3**.

Table 2-2. Measured rate constant values for HO2 + $C_2H_5O_2$

T (K)	k_2 / $10^{-12\ (a)}$
295	5.57 ± 0.36
284	5.41 ± 0.36
273	6.20 ± 0.59
263	6.29 ± 0.54
254	7.25 ± 0.52
241	8.59 ± 0.74
231	9.87 ± 1.06
221	11.0 ± 1.08

(a) Units cm^3 $molecules^{-1}$ s^{-1}

Table 2-3. Summary of results for the HO_2 + $C_2H_5O_2$ reaction rate constant

Ref.	A/ $10^{-13\ (a)}$	E_a/R (K^{-1})	k_2(298K)/$10^{-12\ (a)}$
[5]	NA	NA	6.3
[6]	5.6 ± 2.4	650 ± 125	5.2
[7]	1.6 ± 0.4	1260 ± 130	10.4
[8]	6.9 (+2.1, -1.6)	702 ± 69	8.3
[4]	NA	NA	8.14
[9]	2.08 (+0.87, -0.62)	864 ± 79	3.97
(b)	**6.01 (+1.95, -1.47)**	**638 ± 73**	**5.6**

(a) Units $molecules^{-1}$ cm^3 (b) Current study

An Arrhenius fit to our data gives, $k_2(T)=\left(6.01\,^{+1.95}_{-1.47}\right)\text{x}10^{-13}\exp\left(\frac{638 \pm 73}{T}\right)$. The pressure dependence of k_2 was studied over the range 50–200 Torr of N_2 at 296 K and 231 K. No dependence on pressure was observed at either of these temperatures in agreement with previous measurements.[5,6,8,9]

2.3.4 $C_2H_5O_2 + C_2H_5O_2$ kinetics and branching fraction

Three kinetics parameters were determined from the studies of (2.3): k_{3obs}, k_3, and α. Reaction (2.3) was investigated over the same temperature range as (2.2), 221–296 K. The total initial radical concentration was varied over the range 3.0 x 10^{13}–1.5 x 10^{14} molecules cm^{-3}. At the largest total radical concentrations O_2 was varied to check for secondary chemistry other than the production of HO_2. Using the UV data alone it is possible to determine k_{3obs} which is related to k_3 by equation (i). The value of k_{3obs} measures the total loss of $C_2H_5O_2$. It incorporates loss from both the self reaction and from reaction with secondary HO_2. Combining the UV and NIR data allows for determination of k_3 and α. Values for k_{3obs} were measured over the pressure range 50–200 Torr. Values for k_3 and α could only be measured at 50 Torr because of decreased sensitivity due to pressure broadening in the WM detection of HO_2.

It is difficult to directly compare the different values of k_{3obs} from different studies because the value actually measured, k_{3obs}/σ_λ is dependent on the wavelength used to make the determination and the spectrometer instrument lineshape function. In the present study to determine k_{3obs}, $\lambda = 250$ nm was used and σ_{250} was taken from the JPL-06 recommendation.[31] In order to compare with the present work, previous data sets were normalized to the value of σ recommended in the JPL-06 evaluation for the λ used in that experiment. **Figure 2-5** compares the previous and present work on k_{3obs}.

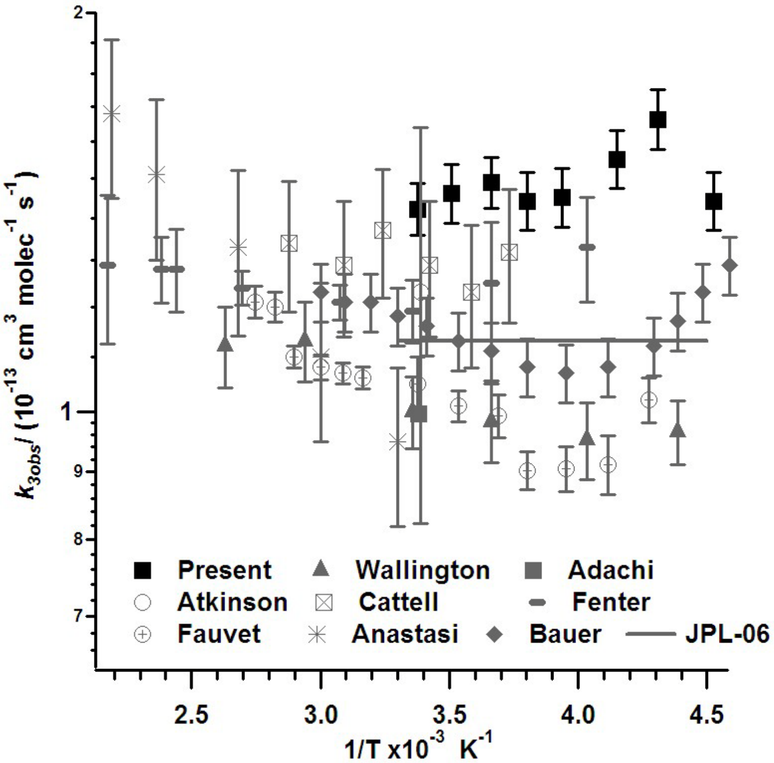

Figure 2-5. Comparison of k_{3obs} with previous work. Error bars are 1 σ.

An Arrhenius fit to our data leads to the expression

$k_{3obs}(T) = \left(1.18\ ^{+0.23}_{-0.19}\right) \text{x}10^{-13} \exp(\frac{58 \pm 45}{T})$. **Table 2-4** presents our data for k_{3obs} at all temperatures and pressures . We do not see a pressure dependence for k_{3obs} in agreement with previous results, however there is a slightly anomalous decrease in k_{3obs} at 200 Torr. Values for k_d, the rate constant for the unimolecular disappearance due to diffusion were determined along with the values for k_{3obs}. For $C_2H_5O_2$, $k_d = 5 \pm 1$ s^{-1} and was invariant over the pressure range 50–200 Torr. Diffusion constants should be inversely proportional to pressure, so if rather than using the measured value we assume a linear dependence on pressure (i.e., if $k_d = 5$ s^{-1} at 50 Torr then at 200 Torr $k_d = 1.25$ s^{-1}) and use that to fit the 200 Torr data we get values for k_{3obs} that agree much better. These values are shown in parenthesis for the 200 Torr data in **Table 2-4**. While it can not be ruled out that the lower pressure data are under-representing the diffusion effect, this seems unlikely because the fits to the 200 Torr data improve based on total residual sum of squares when using the lower k_d values. Trying the opposite route, increasing k_d for the 50 Torr data linearly (i.e., 50 Torr k_d = 20 s^{-1}) from the fitted 200 Torr values, leads to unacceptable fits.

Table 2-4. Results of $C_2H_5O_2$ self reaction at all temperatures and pressures

T (K)	P (Torr)	k_{3obs} / 10^{-13} (a)	k_3 / 10^{-13} (a)	α
295	50	1.42 ± 0.07	1.10 ± 0.09	0.32 ± 0.05
284	50	1.46 ± 0.08	1.17 ± 0.07	0.27 ± 0.03
273	50	1.49 ± 0.07	1.22 ± 0.05	0.23 ± 0.03
263	50	1.44 ± 0.07	1.18 ± 0.06	0.23 ± 0.03
254	50	1.45 ± 0.08	1.13 ± 0.06	0.30 ± 0.03
241	50	1.55 ± 0.08	1.24 ± 0.07	0.28 ± 0.03
231	50	1.66 ± 0.09	1.36 ± 0.11	0.25 ± 0.05
221	50	1.44 ± 0.07	1.02 ± 0.07	0.43 ± 0.05
295	200	1.20 ± 0.09 (1.55)		
231	200	1.23 ± 0.09 (1.62)		
298(b)	all P	1.1	6.8	0.6

(a) Units cm^3 $molecule^{-1}$ s^{-1}. (b) Values from [1]

The values for α are shown in **Figure 2-6** along with the previous results from the end product studies. To our knowledge this is the first published investigation of the temperature dependence of α below room temperature. A weighted average of the measurements leads to the expression α = 0.28 ± 0.06. The larger error bars and scatter of the measured value reflect the sensitivity of α to correlation with the other parameters, but were not interpreted as any temperature dependence.

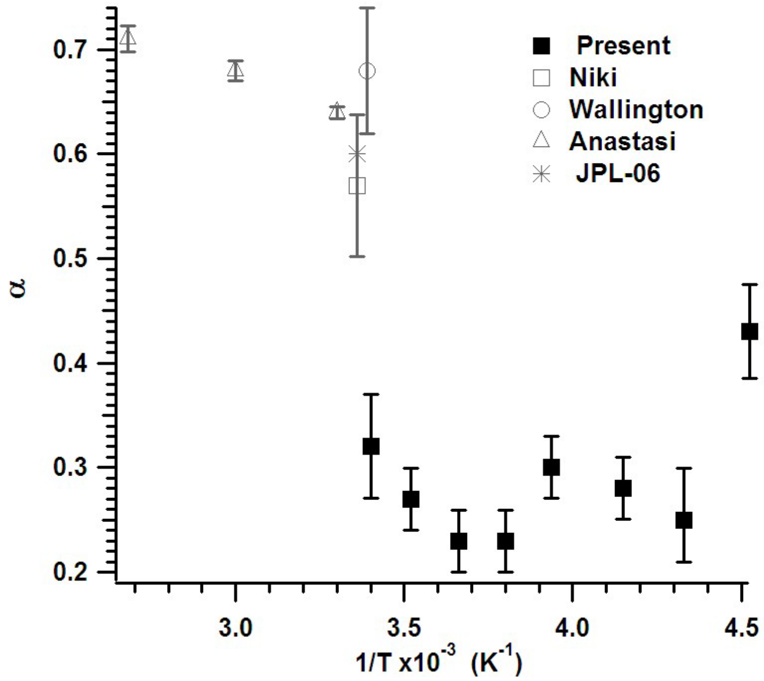

Figure 2-6. Comparison of α with previous work. Error bars are 1σ.

For reaction (2.3) varying the [O_2] provided a check on whether (2.4) was the only subsequent reaction of C_2H_5O. In our experiments where [O_2] was varied no difference in k_{3obs} was measured similar to the experiments of Cattell et al.[5] However values for α did not remain consistent as [O_2] varied, and the temporal profile of HO_2 from the IR data could not be fit as accurately. Inclusion of the chemistry suggested by Cattell et al.,

$$C_2H_5O + C_2H_5O_2 \longrightarrow C_2H_5OOH + CH_3CHO'' \tag{2.12}$$

allowed for agreement across all [O_2] values. Values for k_{12} were generally determined at the lowest [O_2] values where (2.4) would be slowed. The rate coefficient k_{12} = (1.54 ± 0.7) x 10^{-11} cm^3 molecules^{-1} s^{-1} independent of temperature.

Lastly it was possible to measure k_3 directly. The Arrhenius expression derived from the data is, $k_3(T) = \left(1.29\, ^{+0.34}_{-0.27}\right) \mathrm{x} 10^{-13} \exp\left(\frac{-23 \pm 61}{T}\right)$. **Table 2-4** shows the values measured for k_{3obs}, k_3, and α along with current recommendations for them.

2.3.5 CH$_3$OH Chaperone effect

The methanol chaperone effect on (2.5) has previously been investigated in this laboratory and others.[12,13] This effect enhances the observed rate of reaction at low temperatures through the following mechanism.

$$\mathrm{HO_2 + CH_3OH \rightleftharpoons HO_2{\bullet}CH_3OH} \quad (2.13)$$

$$\mathrm{HO_2 + HO_2{\bullet}CH_3OH \longrightarrow H_2O_2 + CH_3OH + O_2} \quad (2.14)$$

$$\text{Net:}\ \mathrm{HO_2 + HO_2 \xrightarrow{CH_3OH} H_2O_2 + O_2} \quad (2.15)$$

Under the conditions of low [CH$_3$OH] used in this experiment, the dependence of k_{5obs} on [CH$_3$OH] is that derived in the Christensen et al. paper,[33]

$$k_{5obs} = k_5 + \left(k_{14} - 2k_5\right) K_{13}\left[\mathrm{CH_3OH}\right] \quad \text{(iii)}$$

In this experiment it was investigated whether the HO$_2$•CH$_3$OH complex might change the observed kinetics of (2.2). At 241 K, a set of experiments at [CH$_3$OH] of 1×10^{15}, 2.5×10^{15} and 5×10^{15} molecules cm^{-3} were performed. No evidence for a methanol chaperone effect was observed on (2.2) at the conditions studied. We were unable to investigate this effect further at lower temperatures and/or higher [CH$_3$OH] due to the large amount of complex that is formed under those conditions. When > ~10% of the HO$_2$ exists in a complexed state the UV and NIR spectroscopy in this experiment are no longer observing the same simple bimolecular reaction. This makes it difficult to accurately calibrate the NIR probe signal. A comprehensive study including other temperatures below 298 K as well as looking at the effect of H_2O would be valuable, but was outside the scope of the present work.

2.4 Discussion

The major strength of this experiment was the ability to monitor HO_2 and $C_2H_5O_2$ using simultaneous but distinct optical probes in the NIR and UV, respectively. A self consistent method was used for measuring the interrelated parameters k_2, k_3, and α. For the first time α was determined by measurement of the nascent radical product on the time scale of the reaction.

There are a number of experimental concerns that need to be addressed when looking at the self and cross reactions of HO_2 and $C_2H_5O_2$, or any RO_2 for that matter. In the cross reaction (2.2) it is important to investigate a wide range of initial radical ratios ($[HO_2]_0/[C_2H_5O_2]_0$) to test for consistency in the results. The simplest conditions to investigate (2.2) are where (2.3) is suppressed, i.e., at $[HO_2]_0/[C_2H_5O_2]_0 > 1$. This prevents interference due to secondary production of HO_2 from (2.4), and leaves (2.5) as the only competing pathway to (2.2). Experiments done under the conditions of the more complicated case where $[HO_2]_0/[C_2H_5O_2]_0 < 1$, must carefully consider the secondary chemistry of (2.3) and (2.4). Under these conditions measurements of k_2 also implicitly check the parameters used for (2.3) due to their influence on the observed rate coefficient. **Figure 2-2** shows the wide range of initial radical ratios examined in the current study of (2.2), and the good agreement across these conditions. The initial radical ratio varied from ~ 0.1–4 at all temperatures. This range is considerably wider than employed in previous studies. As initial conditions shift to more $C_2H_5O_2$ and the secondary chemistry plays a larger role, the value of α used influences what value of k_2 is determined by the model.

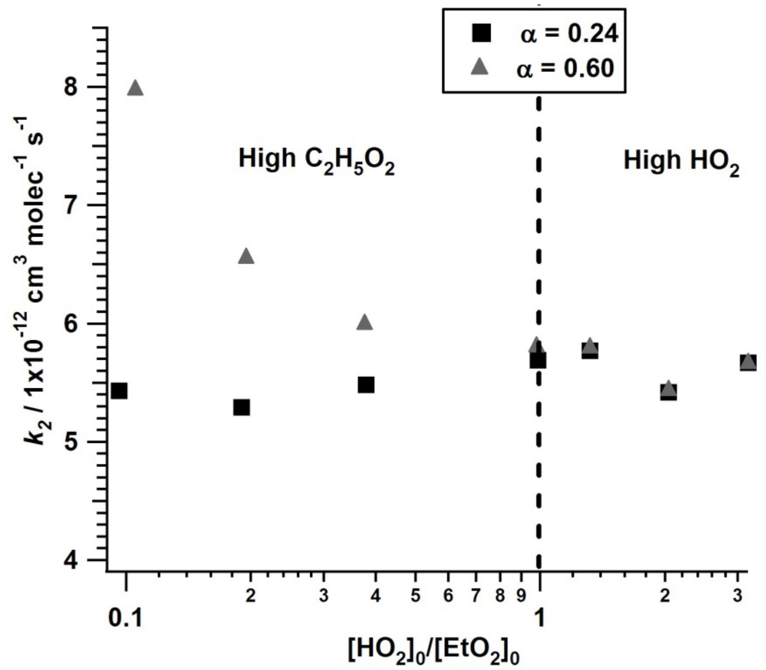

Figure 2-7. Comparison of the fitted values for k_2 using either the previous recommendation for α or the value measured in this study

Figure 2-7 shows the dependence of k_2 on $[HO_2]_0/[C_2H_5O_2]_0$ and α. The data shown are the same except that the value for α used in the model fits was fixed at either the literature value of 0.60, or the value measured by this experiment of 0.24. Prior to performing the current measurement of α we could not explain the trend observed of increasing k_2 with decreasing $[HO_2]_0/[C_2H_5O_2]_0$. Our lower values for α led to a consistent value for k_2. This made it clear that previously the model was trying to compensate for too much secondary HO_2 by increasing the rate of loss of HO_2 by (2.2). **Table 2-5** (given at the end of the chapter) lists the initial radical ratios explored by the previous temperature-dependent studies of (2.2). **Figure 2-7** shows that examining a wide range of initial radical ratios provided a useful check on the consistency of the results.

Another issue that is important to look at is the use of CH_3OH as a precursor for HO_2 in (2.2). CH_3OH is a common precursor for HO_2, but, as discussed in the results and analysis section, it is now known that CH_3OH and HO_2 form a hydrogen bonded complex at low temperatures that enhances the observed rate of the HO_2 self reaction (2.5). Previous studies that used CH_3OH as a precursor may have underestimated k_5 because the chaperone effect was not accounted for. This may have led to an overestimate of k_2 in order to fit the observed time decay of the HO_2 signal, thus attributing the increased decay to reaction with $C_2H_5O_2$ instead of the effect of $CH_3OH{\bullet}HO_2$ on (2.5). In the section on comparison with previous work it will be noted when this could be a contributing factor. This experiment does not see a direct enhancement in the observed rate coefficient k_2 due to the $CH_3OH{\bullet}HO_2$ complex reacting with $C_2H_5O_2$. Therefore it is only the chaperone effect on k_5 that could cause problems.

The last experimental issue pertains to the measurement of α. This experiment is able to make the first direct measurement on the time scale of the reaction. The other studies have all relied on ratios of stable end products minutes after the reaction, which are susceptible to unknown production mechanisms.

2.4.1 Previous work: $HO_2 + C_2H_5O_2$

Figure 2-4 displays the all of the previous work on reaction (2.2) at temperatures < 298 K. The present work is in closest agreement with Dagaut et al.[6] As with all of the UV absorption studies, Dagaut et al. was not able to independently monitor both radicals, but had to rely on spectral deconvolution. The study also only looked at two temperautures below 298 K. Three other factors that may influence the agreement between the studies are: the initial radical ratio range explored, the use of CH_3OH as an

HO_2 precursor, and the UV cross section used. Dagaut et al. did explore a wide range of initial radical ratios, but they were using the larger value for α recommended by the end product studies. This may have biased their results to larger values although they did not report any discrepancy in k_2 when changing initial radical ratio. They also used large values of CH_3OH (1.1–5.5 x 10^{16} molecules/cm^3) as an HO_2 precursor without accounting for the CH_3OH chaperone effect, leading to a potential overestimate of k_2 at lower temperatures. Lastly, the UV cross sections used by Dagaut et al. were lower than those currently recommended and it is estimated that using the current recommendation would add ~20–30% to the values reported.[2,8] It is possible that the competing errors may somewhat offset each other, leading to the agreement seen.

Maricq et al.[8] is another UV absorption study in reasonable agreement with our work. The study used fluorine chemistry as a precursor for its radicals so no correction for CH_3OH is needed. There is good agreement for the value of $\frac{E_A}{R}$ across Dagaut et al., Maricq et al., and the current work. Some of the difference between the actual values in Maricq et al. and the present work can probably be attributed to larger k_2 from larger α values used because the bulk of their experiment were carried out at $[HO_2]_0/[C_2H_5O_2]_0$ = 0.67. However, the small excess of $C_2H_5O_2$ under their conditions would account for at most 5–10% of the ~50% discrepancy. There are no other obvious reasons for the discrepancy between the experiments, but especially at low temperatures the agreement becomes better as the data sets agree within the stated uncertainties.

Fenter et al.[7] is the temperature dependent study that deviates from the rest. It was a UV absorption study similar to the Maricq et al. and Dagaut et al. work. The low temperature data were limited to two points below 298 K, and the study also used large CH_3OH concentrations (1.5–6 x 10^{16} molecules/cm^3) without knowing about the chaperone effect. This effect would not be large enough to account for the discrepancy seen here. As has been stated previously, there is no clear reason for the discrepancy between the Fenter et al. results and the rest.[8] The Arrhenius parameters and k_2(298K) of Fenter et al. stand out in **Table 2-3.** The results from the present study and Raventos-Duran et al. suggest that there may have been systematic errors in the low temperature data of Fenter et al.

The most recent investigation is the Raventos-Duran et al.[9] work, which used the CIMS technique. This experiment was the only one not using UV absorption for radical detection, and was the first temperature-dependent study to independently monitor the HO_2 and $C_2H_5O_2$ concentrations. The agreement between the Raventos-Duran et al. work and the current study appears acceptable especially at low temperatures. Their $\frac{E_A}{R}$ value of 864 K^{-1} is slightly larger than the currently recommended value of 700 K^{-1}.

There have also been two room temperature studies by Cattell et al. and Boyd et al.[4,5] The Cattell et al. study was the first to use diode laser IR spectroscopy to independently monitor HO_2. They could not simultaneously measure HO_2 and $C_2H_5O_2$, as in the current study, but there is good agreement between our values. The Boyd et al. study used only UV absorption and is in better agreement with the Maricq et al. value at 298K.

Overall the present work is part of a convergence in the measurements of k_2. The largest uncertainties remain in its 298 K value, but there is agreement in its temperature dependence and overlap among lower temperature data points within their uncertainties.

2.4.2 Previous work: $C_2H_5O_2$ + $C_2H_5O_2$: k_{3obs}

All previous investigations of reaction (2.3) have either studied the kinetics or the branching fraction of the reaction, but unlike this experiment, never both simultaneously. Previous kinetics measurements obtained values for k_{3obs} and then determined k_3 using α determined from end product studies and the relationship in equation (i). **Figure 2-5** is a comparison of results for k_{3obs}. The results from this study are the largest reported values and are ~25% larger than the JPL-06 recommended value at 298 K. We report an $\frac{E_A}{R}$ = -58 K by fitting an Arrhenius expression to the data. Of the previous studies, The Fenter et al.[7] work ($\frac{E_A}{R}$ = -60 K) and the Cattell et al.[5] data ($\frac{E_A}{R}$ ~ 0) are in the closest agreement with the present study. The Fauvet et al.[17] ($\frac{E_A}{R}$ = 128 K) and Wallington et al.[19] ($\frac{E_A}{R}$ = 110 K) agree very well with each other and both observe the opposite trend of a steady decrease in rate constant with temperature. Anastasi et al.[11] also observed a decreasing rate constant but with a much steeper decline than was observed in any other study. None of the other previous studies went quite as low in temperature as Bauer et al. so it is possible that they would not have observed the change in temperature dependence observed by Bauer et al., and there is some evidence for the beginning of a change at the lowest temperature of Wallington et al. and Fauvet et al. There are no clear experimental reasons for the discrepancies between the different studies. All the studies were done using UV absorption, and the data have been normalized as best possible for differences in σ as discussed in the results section. **Table 2-6** (given at the end of the chapter) summarizes the experimental conditions of each study and the measured $\frac{E_A}{R}$. Agreement between studies is not split down obvious lines of different experimental techniques, source chemistry, or pressure range. None of the previous studies saw any effect due to pressure. The overall spread in the data from the different studies would ideally be less, but is not unreasonable. However the temperature dependence of the reaction is still very uncertain and more work to determine it is needed.

2.4.3 Previous work: $C_2H_5O_2$ + $C_2H_5O_2$: k_3 and α

This experiment is the first to measure k_3 directly, and not rely on equation (i) in order to calculate it. **Table 2-4** lists the values measured and compares then with the current recommendation.[31] The measured values are nearly twice the currently recommended value. This increase is predominantly due to the difference in α as the relationship in equation (i) is a valid approximation for most conditions. The rest of the discrepancy is explained by the slightly larger values of k_{3obs} discussed above. The current recommendation lists (2.3) as having no T dependence which is in agreement with the value from this work, $\frac{E_A}{R}$ = 23 ± 61.

The current study is also the first “direct” study of α. Monitoring the HO_2 from reaction (2.4) is not technically a direct measurement as it is one step removed from the actual $C_2H_5O_2$ self reaction. However under most experimental conditions sufficient O_2 insured essentially complete conversion by reaction (2.4) and the possibility of (2.12) was accounted for. Every previous measurement of α was a continuous photolysis end product study which made measurements of the stable products on a timescale of minutes. Of the five previous studies on α we will focus on three.[11,21,22] The other works by Kaiser et al.[20] and Anastasi et al.[14] were superseded by a new study from the same group and never published in the peer reviewed literature, respectively, and so will not be mentioned further here. **Figure 2-6** shows the wide gap between the current and previous measurements, this discrepancy is discussed below.

The study by Anastasi et al.[11] was a continuous photolysis experiment using azoethane ($(C_2H_5)_2N_2/O_2$) initiation chemistry and irradiation by UV lamps. They used GC/MS detection of the products over the course of minutes and explored temperatures in the range 303–372 K. Total pressure was varied, but typically was ~500 Torr. Product ratios were related to the reaction rates by the expressions:[21]

$$\left[\mathrm{C_2H_5OH}\right]/\left[\mathrm{CH_3CHO}\right]=k_{3b}/\left(2k_{3a}+k_{3b}\right) \qquad \text{(iv)}$$

$$\left[\mathrm{C_2H_5OOH}\right]/\left[\mathrm{C_2H_5OH}\right]=2k_{3a}/k_{3b} \qquad \text{(v)}$$

They also explored the effect different O_2 concentrations had on the product ratios, and noticed an increase in C_2H_5OOH yield and decrease in C_2H_5OH yield as O_2 is raised. This indicates that the products in reaction (2.12) may not only be the stable ones suggested, but instead may also have a channel producing C_2H_5OH and a diradical (e.g., CH_3CHOO). Overall they did not observe steady product ratios over time and tried to rely on the initial rates of formation at high O_2 to determine α. In the modeling of their data they also used quite different values for key rate coefficients which could have influenced their determination of the initial rates. The combination of these effects makes it difficult to compare their results to the current study, but does suggest that it's possible that the different timescales of the end product study and the current study could display very different results.

The first measurement of α was made by Niki et al.[21] using a continuous photolysis FTIR experiment at room temperature and 700 Torr. Data were typically recorded after 5,10, or 20 min periods of irradiation by UV lamps. Both azoethane and chlorine ($Cl_2/C_2H_6/O_2$) chemistries were used to generate the radicals. Similar product ratios for $[C_2H_5OH]/[CH_3CHO]$ were found for both chemistries and there was no change over time. A different ratio than those previously mentioned, the ratio of $[C_2H_5OOH]/[CH_3CHO]$ did appear to decrease with time, and this decrease was more evident when using the azoethane chemistry that required longer irradiation times. They interpreted the changing ratio as a heterogeneous loss of C_2H_5OOH. One possibility of chemistry that was overlooked in this study is the reaction of Cl with C_2H_5OH.[34]

$$\mathrm{Cl} + \mathrm{C_2H_5OH} \longrightarrow \text{products} \tag{2.16}$$

$$\longrightarrow \mathrm{CH_3CHOH} + \mathrm{HCl}\ (90\%) \tag{2.16a}$$

$$\longrightarrow \mathrm{CH_2CH_2OH} + \mathrm{HCl}\ (10\%) \tag{2.16b}$$

$$\mathrm{CH_3CHOH} + \mathrm{O_2} \longrightarrow \mathrm{HO_2} + \mathrm{CH_3CHO} \tag{2.17}$$

If this chemistry were occurring in the chlorine system then it could provide an explanation for how, over time, the yield of C_2H_5OH could be artificially reduced and that of CH_3CHO increased to yield an apparently higher branching fraction in k_{3a}. Simultaneous Cl reaction with CH_3CHO at comparable rates as (2.16) would keep the ratio in equation (iv) stable,[35,36] as observed in their data. However this chemistry would not explain the agreement seen between the two different initiation chemistries because this chemistry would not occur in azoethane mixture where no Cl is present.

The last study by Wallington et al.[22] is very similar to the Niki et al. study, and is also a continuous photolysis FTIR study. It was a room temperature study at 700 Torr total pressure. Chlorine initiation chemistry was used and no change in the product ratios with time was observed. They note that they had the smallest surface/volume ratio of any of the previous experiments, minimizing the effect of any surface reactions. The reactions of Cl with the products C_2H_5OH, CH_3CHO, and C_2H_5OOH were modeled and corrections were made to the observed product ratios, but it does not appear that the full sequence of reactions (2.16) – (2.17) are included, allowing another route of production for CH_3CHO. For both the Niki et al. and Wallington et al. studies there are no clear reasons for the discrepancy between the current results and theirs.

One hypothesis for the discrepancy between the end product studies and the current one is the pathway (2.3c) and then photolysis of the diethylperoxide $C_2H_5O_2C_2H_5$.

$$\mathrm{C_2H_5OOC_2H_5} \xrightarrow{hv} \mathrm{2C_2H_5O} \tag{2.18}$$

Of the three studies only Niki et al. saw any evidence for its formation. If the diethylperoxide formed and photolyzed on the timescale of seconds it would generate ethoxy radicals. The ethoxy radicals would not be distinguishable from the fraction of the reaction that proceeded through pathway (2.3a) and would be lumped together during the end product studies.

The lower value of α measured in this study is closer in value to α for the CH_3O_2 self reaction, which ranges from 0.28–0.43.[2] Agreement would not necessarily be expected because k_{3obs} for CH_3O_2 is 3–4 times larger than for $C_2H_5O_2$ indicating that different pathways may be preferred in each case.[2] It is also interesting that a temperature dependence is not observed for α in this study. An experiment by Horie et al.[37] on CH_3O_2 suggest that there is a steep decrease in the k_{3a}/k_{3b} branching ratio with temperature down to 223 K. The overall temperature dependence of (2.3) is fairly flat in the studied temperature range, unlike the behavior seen in the CH_3O_2 self reaction rate coefficients, which may explain some of the observed difference between the two systems. Still α

could easily have a temperature dependence due to the different barriers for different product channels, while the overall rate coefficient temperature dependence would only be determined by the initial intermediate formation. Given the large deviation between α measured with our experiment and the value from the end product studies in the literature, validation of these results will be necessary.

2.4.4 Mechanism

The complete picture of reaction (2.2) has been developed by work done on both the mechanism and products of the reaction. A number of product studies using FTIR have determined that the product channel shown for reaction (2.2) is the only one available at room temperature.[38-40] The Raventos-Duran et al.[9] temperature-dependent CIMS study confirmed that C_2H_5OOH is the major product channel all the way down to 195 K.[9] Work by Elrod et al. on $CH_3O_2 + HO_2$[41] detected a minor channel leading to the products $HCHO + H_2O + O_2$ that grew larger at lower temperature. The Raventos-Duran et al. work could not check for the analogous minor channel leading to $CH_3CHO + H_2O + O_2$, and so this would be worth investigating. Recent theoretical works agree with the product studies about the dominant product channel,[9,42,43] and are coming to a consensus on the likely mechanism for $RO_2 + HO_2$ reactions in general. The general mechanism involves the formation of both a hydrogen bonded intermediate on the triplet surface and a tetroxide intermediate on the singlet surface. Barriers to the transition state are too high on the singlet surface (when R is a straight chain alkyl group) despite the more stable nature of the tetroxide. The bulk of the reaction then proceeds through the hydrogen bonded structure on the triplet surface. The intermediate formation is indicative of the negative activation energy observed in the reaction's Arrhenius dependence. The lack of an observed pressured dependence on the reaction indicates that the intermediate formation is the rate limiting step and that it proceeds to products prior to a collision. The fact that collisional stabilization is not needed prior to reaction may explain the lack of an observed enhancement in the rate of reaction (2.2) in the presence of the HO_2•CH_3OH complex, as there is no benefit to having the CH_3OH as a collision partner.

Other HO_2 hydrogen bonded complexes have shown a similar lack of rate enhancement when reacting with RO_2. The HO_2•H_2O complex has been observed and its effect of increasing the observed rate of reaction (2.5) is well known.[44-47] The large amounts of H_2O vapor in the atmosphere make the reactions of HO_2•H_2O potentially very important. Recent work from English et al. showed that H_2O did not enhance the observed rate of reaction between CH_3O_2 + HO_2.[48] This work, along with the current study provides further confirmation of the likely mechanism for the RO_2 + HO_2 reactions.

The mechanism of reaction (2.3) and the self reaction of RO_2 in general needs more work. A recent paper by Dibble et al. nicely summarizes the current theory and its problems.[49] The Russell mechanism for the production of the stable products through a cyclic tetroxide intermediate has been the accepted mechanism for all simple RO_2 self reactions.[50] However, the most rigorous theoretical study on the smallest system, the CH_3O_2 self reaction, did not find a transition state resembling the Russell mechanism pathway.[51] This raises serious questions that need to be resolved given the long standing acceptance of the Russell mechanism. For reaction (2.3) specifically there has been only one computational attempt to determine the reaction pathway.[52] This study shows a transition state below the energy of the reactants for all three reaction paths (R3a–c), but in light of the analysis in the Dibble paper may need a higher level of theory to capture the behavior observed in experiments. Furthermore, given the uncertainty now in the measured value of α, understanding the actual reaction path to the various product channels will allow a prediction of α to compare with the experiments. Lastly, from the variation in rate constants between the CH_3O_2 and $C_2H_5O_2$ self reactions (~4.5 x 10^{-13} and ~1.5 x 10^{-13}), it is clear that work on different examples of RO_2 are needed to understand the mechanism of the self reaction and shed light on the variety of kinetics measured.

2.5 Conclusion

The kinetics of the $C_2H_5O_2$ reaction system, including k_2, k_{3obs}, k_3, and α, were measured using simultaneous independent detection of the $C_2H_5O_2$ and HO_2 radicals. WM NIR spectroscopy allowed for sensitive and specific detection of HO_2 while UV absorption was used to predominantly monitor $C_2H_5O_2$. The first direct measurements of k_3 and α were made and their sensitivity to k_2 was established. Self consistency established between all the measured parameters provided confidence in the measurements and helped determine the overall uncertainty in each. The experiments on the atmospherically important k_2 added to the growing consensus on the mechanism and overall rate constant for this reaction with an Arrhenius expression $k_2(T)=\left(6.01\,^{+1.95}_{-1.47}\right)\mathrm{x}10^{-13}\exp\left(\frac{638 \pm 73}{T}\right)$. Meanwhile the measurements of k_3 and α provided strikingly different results than those obtained previously, $k_3(T)=\left(1.29\,^{+0.34}_{-0.27}\right)\mathrm{x}10^{-13}\exp\left(\frac{-23 \pm 61}{T}\right)$ and $\alpha = 0.28 \pm 0.06$ independent of temperature. The difference in α is especially glaring given that its literature value is frequently used as the branching fraction value for all RO_2 self reactions with $R \neq CH_3$. It was also the first low temperature study of α. Both experimental and theoretical verification of k_3 and α are needed in order to better understand the self reactions of $C_2H_5O_2$ and the self reactions of RO_2 in general.

Table 2-5. Summary of experimental conditions for the determination of the HO_2 + $C_2H_5O_2$ reaction rate constant

Ref	Method$^{(a)}$	Source Gases	$[CH_3OH]^{(b)}$	Bath	$T^{(c)}$	$P^{(e)}$	$[EtO_2]_0:[HO_2]_0$	$\lambda_{UV}^{(f)}$
[6]	FP/UV	$Cl_2/O_2/C_2H_6/CH_3OH$	1.1–5.5	N_2	248–380 298	100 25–400	0.22–6	250
[7]	FP/UV	$Cl_2/O_2/C_2H_6/CH_3OH$	1.5–6	N_2	248–460	760	0.5–2.0	220 260
[8]	LFP/UV	$F_2/O_2/C_2H_6/H_2$	--	N_2	210–363	200	1.3 (0.6–2 at 243 and 338 K)	
[5]	FP/UV/IR	$Cl_2/O_2/C_2H_6/CH_3OH$	0.06	N_2	295	2.4	2	210 260
[4]	LFP/UV	H_2O_2/C_2H_6	--	air	298	760	0.1–0.25	210 270
[9]	CIMS	$F_2/O_2/C_2H_6/H_2/He^{(i)}$	--	N_2	195–298	75–200	<1	
(h)	LFP/UV/IR	$Cl_2/O_2/C_2H_6/CH_3OH$	0.001–0.1	O_2	221–296	100	0.3–10	250

(a) FP: Flash photolysis, LFP: Laser flash photolysis, CIMS: Chemical ionization mass spectrometry, UV: UV absorption spectroscopy, IR: near-IR diode laser spectroscopy. (b) Units: $\times 10^{16}$ molecules cm^{-3}. (c) Units: K. (e) Units: Torr. (f) Units: nm (h) Current study (i) microwave discharge creates radicals.

Table 2-6. Summary of previous experiments on $C_2H_5O_2$ + $C_2H_5O_2$

ref	technique	source gas	T (K)	P (Torr)	λ(nm)	$\sigma^a/10^{-18}$ used^b/rec^c	E_a/R (K)
[10]	FP/UV	(CH3CH2)2N2/O2	298	625	230–250 (236)	3.9/4.4	-
[11]	MM/UV	(CH3CH2)2N2/O2	303–457	495	240	6.23/4.52	?
[18]	PR/UV	H2/C2H4/O2	298	760	240	5.19/4.52	-
[5]	MM/UV	(CH3CH2)2N2/O2	266–347.5	27–760	260	3.4/3.24	0
[19]	FP/UV	Cl2/C2H6/O2	228–380	25–400	250	3.89/4.12	110±40
[16]	MM/UV	Cl2/C2H6/O2	218–333	760	250	4/4.12	147±30[e]
[7]	FP/UV	Cl2/C2H6/O2	248–260	760	220–260 (240)	4.89/4.52	-60±40
[17]	MM/UV	Cl2/C2H6/O2	253–363	200	240–250 (250)	4.04/4.12	128
[15]	LFP/CRDS	Cl2/C2H6/O2	295	5.5	270	2.14/2.14	-
(d)	LFP/UV	Cl2/C2H6/O2	221–295	50–200	250	4.12/4.12	-58±45

FP: Flash photolysis, MM: Molecular modulation, PR: Pulse Radiolysis, LFP: Laser flash photolysis, UV: UV absorption, CRDS: Cavity ringdown spectroscopy, (a) units of cm^{-2}, (b) value of σ used in the ref. to determine k_{3obs}, (c) value of σ from JPL-06[31] that was used to normalize k_{3obs}, (d) Current study, (e) Over the T range 250–330, below 250 curvature is observed.

2.6 References

(1) Jacob, D. J. *Introduction to Atmospheric Chemistry*; Princeton University Press: Princeton, NJ, 1999.

(2) Tyndall, G. S.; Cox, R. A.; Granier, C.; Lesclaux, R.; Moortgat, G. K.; Pilling, M. J.; Ravishankara, A. R.; Wallington, T. J. *Journal of Geophysical Research-Atmospheres* **2001**, *106*, 12157.

(3) Rudolph, J. *Journal of Geophysical Research-Atmospheres* **1995**, *100*, 11369.

(4) Boyd, A. A.; Flaud, P. M.; Daugey, N.; Lesclaux, R. *Journal of Physical Chemistry A* **2003**, *107*, 818.

(5) Cattell, F. C.; Cavanagh, J.; Cox, R. A.; Jenkin, M. E. *Journal of the Chemical Society-Faraday Transactions Ii* **1986**, *82*, 1999.

(6) Dagaut, P.; Wallington, T. J.; Kurylo, M. J. *Journal of Physical Chemistry* **1988**, *92*, 3836.

(7) Fenter, F. F.; Catoire, V.; Lesclaux, R.; Lightfoot, P. D. *Journal of Physical Chemistry* **1993**, *97*, 3530.

(8) Maricq, M. M.; Szente, J. J. *Journal of Physical Chemistry* **1994**, *98*, 2078.

(9) Raventos-Duran, M. T.; Percival, C. J.; McGillen, M. R.; Hamer, P. D.; Shallcross, D. E. *Physical Chemistry Chemical Physics* **2007**, *9*, 4338.

(10) Adachi, H.; Basco, N. *Chemical Physics Letters* **1979**, *64*, 431.

(11) Anastasi, C.; Waddington, D. J.; Woolley, A. *Journal of the Chemical Society-Faraday Transactions I* **1983**, *79*, 505.

(12) Andersson, B. Y.; Cox, R. A.; Jenkin, M. E. *International Journal of Chemical Kinetics* **1988**, *20*, 283.

(13) Christensen, L. E.; Okumura, M.; Sander, S. P.; Salawitch, R. J.; Toon, G. C.; Sen, B.; Blavier, J. F.; Jucks, K. W. *Geophysical Research Letters* **2002**, *29*.

(14) Anastasi, C. B., M.J.; Smith, D.B.; and Waddington, D.J. Joint Meeting of the French and Italian Sections of the Combustion Institute, June 1987, Amalfi.

(15) Atkinson, D. B.; Hudgens, J. W. *Journal of Physical Chemistry A* **1997**, *101*, 3901.

(16) Bauer, D.; Crowley, J. N.; Moortgat, G. K. *Journal of Photochemistry and Photobiology a-Chemistry* **1992**, *65*, 329.

(17) Fauvet, S.; Ganne, J. P.; Brion, J.; Daumont, D.; Malicet, J.; Chakir, A. *Journal De Chimie Physique Et De Physico-Chimie Biologique* **1997**, *94*, 484.

(18) Munk, J.; Pagsberg, P.; Ratajczak, E.; Sillesen, A. *Journal of Physical Chemistry* **1986**, *90*, 2752.

(19) Wallington, T. J.; Dagaut, P.; Kurylo, M. J. *Journal of Photochemistry and Photobiology a-Chemistry* **1988**, *42*, 173.

(20) Kaiser, E. W.; Rimai, L.; Wallington, T. J. *Journal of Physical Chemistry* **1989**, *93*, 4094.

(21) Niki, H.; Maker, P. D.; Savage, C. M.; Breitenbach, L. P. *Journal of Physical Chemistry* **1982**, *86*, 3825.

(22) Wallington, T. J.; Gierczak, C. A.; Ball, J. C.; Japar, S. M. *International Journal of Chemical Kinetics* **1989**, *21*, 1077.

(23) Lightfoot, P. D.; Cox, R. A.; Crowley, J. N.; Destriau, M.; Hayman, G. D.; Jenkin, M. E.; Moortgat, G. K.; Zabel, F. *Atmospheric Environment Part a-General Topics* **1992**, *26*, 1805.

(24) Christensen, L. E.; Okumura, M.; Sander, S. P.; Friedl, R. R.; Miller, C. E.; Sloan, J. J. *Journal of Physical Chemistry A* **2004**, *108*, 80.

(25) Kaiser, E. W. *Journal of Physical Chemistry* **1995**, *99*, 707.

(26) Clifford, E. P.; Farrell, J. T.; DeSain, J. D.; Taatjes, C. A. *Journal of Physical Chemistry A* **2000**, *104*, 11549.

(27) Kaiser, E. W.; Lorkovic, I. M.; Wallington, T. J. *Journal of Physical Chemistry* **1990**, *94*, 3352.

(28) DeSain, J. D.; Ho, A. D.; Taatjes, C. A. *Journal of Molecular Spectroscopy* **2003**, *219*, 163.

(29) Li, Y. M.; Sun, Q.; Li, H. Y.; Ge, M. F.; Wang, D. X. *Chinese Journal of Chemistry* **2005**, *23*, 993.

(30) Thiebaud, J.; Crunaire, S.; Fittschen, C. *Journal of Physical Chemistry A* **2007**, *111*, 6959.

(31) Sander, S. P.; Finlayson-Pitts, B. J.; Friedl, R. R.; Golden, D. M.; Huie, R. E.; Kolb, C. E.; Kurylo, M. J.; Molina, M. J.; Moortgat, G. K.; Orkin, V. L.; Ravishankara, A. R. "JPL 2006: Chemical Kinetics and Photochemical Data for Use in Atmospheric Studies, Evaluation No. 15, JPL Publication 06-2, Jet Propulsion Lab," 2006.

(32) Vaghjiani, G. L.; Ravishankara, A. R. *Journal of Chemical Physics* **1990**, *92*, 996.

(33) Christensen, L. E.; Okumura, M.; Hansen, J. C.; Sander, S. P.; Francisco, J. S. *Journal of Physical Chemistry A* **2006**, *110*, 6948.

(34) Taatjes, C. A.; Christensen, L. K.; Hurley, M. D.; Wallington, T. J. *Journal of Physical Chemistry A* **1999**, *103*, 9805.

(35) Wallington, T. J.; Skewes, L. M.; Siegl, W. O.; Wu, C. H.; Japar, S. M. *International Journal of Chemical Kinetics* **1988**, *20*, 867.

(36) Seakins, P. W.; Orlando, J. J.; Tyndall, G. S. *Physical Chemistry Chemical Physics* **2004**, *6*, 2224.

(37) Horie, O.; Crowley, J. N.; Moortgat, G. K. *Journal of Physical Chemistry* **1990**, *94*, 8198.

(38) Hasson, A. S.; Tyndall, G. S.; Orlando, J. J. *Journal of Physical Chemistry A* **2004**, *108*, 5979.

(39) Spittler, M.; Barnes, I.; Becker, K. H.; Wallington, T. J. *Chemical Physics Letters* **2000**, *321*, 57.

(40) Wallington, T. J.; Japar, S. M. *Chemical Physics Letters* **1990**, *166*, 495.

(41) Elrod, M. J.; Ranschaert, D. L.; Schneider, N. J. *International Journal of Chemical Kinetics* **2001**, *33*, 363.

(42) Hasson, A. S.; Kuwata, K. T.; Arroyo, M. C.; Petersen, E. B. *Journal of Photochemistry and Photobiology a-Chemistry* **2005**, *176*, 218.

(43) Hou, H.; Li, J.; Song, X. L.; Wang, B. S. *Journal of Physical Chemistry A* **2005**, *109*, 11206.

(44) Aloisio, S.; Francisco, J. S.; Friedl, R. R. *Journal of Physical Chemistry A* **2000**, *104*, 6597.

(45) Kanno, N.; Tonokura, K.; Tezaki, A.; Koshi, M. *Journal of Physical Chemistry A* **2005**, *109*, 3153.

(46) Kircher, C. C.; Sander, S. P. *Journal of Physical Chemistry* **1984**, *88*, 2082.

(47) Suma, K.; Sumiyoshi, Y.; Endo, Y. *Science* **2006**, *311*, 1278.

(48) English, A. M.; Hansen, J. C.; Szente, J. J.; Maricq, A. M. *Journal of Physical Chemistry A* **2008**, *112*, 9220.

(49) Dibble, T. S. *Atmospheric Environment Part a-General Topics* **2008**, *42*, 5837.

(50) Russell, G. A. *Journal of the American Chemical Society* **1957**, *79*, 3871.

(51) Ghigo, G.; Maranzana, A.; Tonachini, G. *Journal of Chemical Physics* **2003**, *118*, 10575.

(52) Feria, L.; Gonzalez, C.; Castro, M. *International Journal of Quantum Chemistry* **2004**, *96*, 380.

3 Peroxy radical self reactions studied by photoionization mass spectrometry

3.1 Introduction

The work in Chapter 2 was one of the first studies to look at the products from a peroxy radical (RO_2) self reaction on the time scale of the reaction. The downside of that work was that it was only able to follow one product channel. The work described here set out to better characterize the products by monitoring all of the stable product channels on the timescale of the reaction.

The specifics of the $C_2H_5O_2$ chemistry introduced in Chapter 2 can be generalized to a wide range of RO_2 whose atmospheric importance was discussed in Chapter 1. The RO_2 self reaction chemistry generally follows the scheme below.

$$\mathrm{RO_2} + \mathrm{RO_2} \longrightarrow \mathrm{ROH} + \mathrm{R'CHO} + \mathrm{O_2} \qquad (3.1)$$

$$\longrightarrow \mathrm{RO} + \mathrm{RO} + \mathrm{O_2} \qquad (3.2)$$

$$\longrightarrow \mathrm{ROOR} + \mathrm{O_2} \qquad (3.3)$$

$$\mathrm{RO} + \mathrm{O_2} \longrightarrow \mathrm{HO_2} + \mathrm{R'CHO} \qquad (3.4)$$

$$\mathrm{RO_2} + \mathrm{HO_2} \longrightarrow \mathrm{ROOH} + \mathrm{O_2} \qquad (3.5)$$

In most cases the RO_2 of interest is generated in the laboratory by reaction of the appropriate alkyl radical (R) with oxygen so the following formation reactions are also important.

$$\mathrm{R} + \mathrm{O_2} \xrightarrow{\mathrm{M}} \mathrm{RO_2} \qquad (3.6)$$

$$\mathrm{R} + \mathrm{O_2} \longrightarrow \mathrm{R''CH{=}CH_2} + \mathrm{HO_2} \qquad (3.7)$$

There are also competing reactions which need to be accounted for, and they make up part of the general scheme.

$$\mathrm{RO_2} + \mathrm{RO} \longrightarrow \mathrm{Products} \qquad (3.8)$$

$$\mathrm{HO_2} + \mathrm{HO_2} \longrightarrow \mathrm{H_2O_2} + \mathrm{O_2} \qquad (3.9)$$

The key physical parameter of interest for this work was the radical channel branching fraction of the RO_2 self reaction (reaction (3.2)) defined as,

$$\alpha = \frac{k_{1.2}}{k_{1.1} + k_{1.2} + k_{1.3}} \qquad \mathrm{i}$$

During this work methyl (CH_3), ethyl (C_2H_5), and propyl (C_3H_7) R groups were investigated. Previous work on the CH_3O_2 self reaction was reviewed by Tyndall et al.[1], work on the $C_2H_5O_2$ self reaction was discussed in Chapter 2, and there have been only two product studies on the i-$C_3H_7O_2$ self reaction.[2,3] Of this previous work only the experiments described in Chapter 2 and high temperature (T > 373 K) work by Lightfoot et al.[4] monitored the nascent products on the timescale of the reaction. All of the other studies analyzed the stable end products by FTIR, GC, and GC/MS seconds to minutes after the reaction. The work in Chapter 2 measured a value for α a factor of two lower than the end product studies found for the $C_2H_5O_2$ self reaction by measuring the secondary HO_2 formed from reactions (3.2) and (3.7) using near-infrared kinetics spectroscopy. This work set out to determine whether detection of all the stable products on the time scale of the reaction using a photoionization mass spectrometer technique could determine the cause of the discrepancy between previous end product studies and the work in Chapter 2.

3.2 Experimental

A flash photolysis flow cell coupled to a photoionization mass spectrometer was used to study the product branching ratio of reactions (3.1) – (3.3). The RO_2 chemistry was initiated by laser photolysis and then reacted throughout the laminar flow cell. As the plug flow moved down the flow cell it was sampled from a pinhole at the midpoint of the cell. The sampled gas expanded into the ionization region where it was ionized by the synchrotron radiation. Ion optics then focused a beam into the mass spectrometer where a sector magnet separated the masses for simultaneous detection with a micro-channel plate detector. The product masses were identified by their time traces as well as characteristic ionization energies. The branching fraction was determined by measuring the ratio of the product masses as well as by conversion to absolute concentrations combined with kinetics modeling.

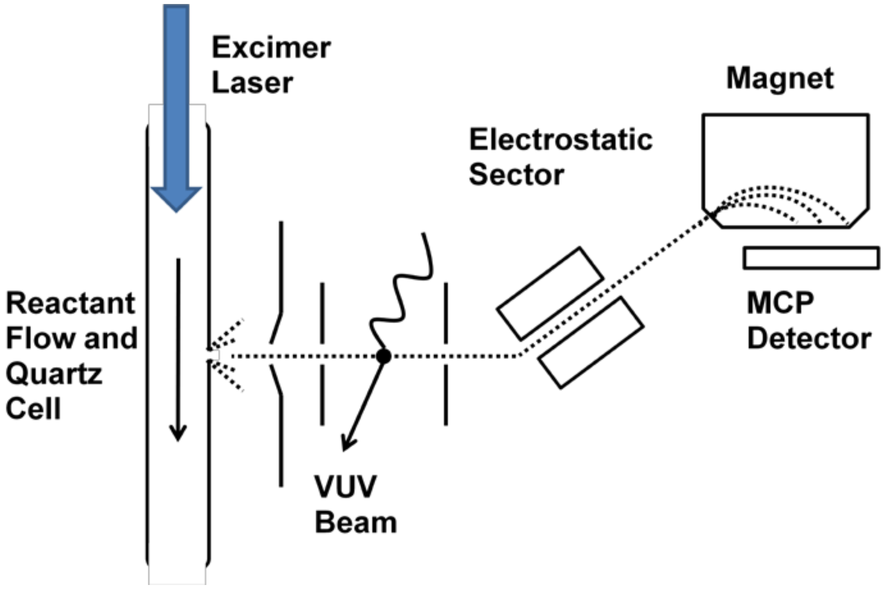

Figure 3-1. Schematic of experimental system

A schematic of the experiment is shown in **Figure 3-1**, and the full apparatus has been described previously.[5] The flow tube was 60 cm long with a 600 μm pinhole 35 cm from the entrance. Mass flow controllers delivered the precursor gases to the cell where the total pressure was controlled by an automated feedback throttle valve leading to a vacuum pump. Typical flow velocities were ~400 cm s^{-1} allowing for a fresh fill of precursor gas for every photolysis pulse.

Ionizing synchrotron undulator radiation came from the Advanced Light Source (ALS) at Lawrence Berkeley National Lab, and was dispersed using a 3 m monochromator on the Chemical Dynamics Beamline. A 30 Torr Ar gas filter suppressed higher undulator harmonics. The radiation energy could be scanned during a data set with energy resolution of 40 – 80 meV corresponding to a monochromator slit width of 0.6 – 1 mm. Energy calibration was done using Ar absorbance using the Ar gas filter as an absorption cell, O_2 autionization resonances, and Xe atomic resonances.

The quasi-continuous synchrotron light passed through the ionization region of a miniature double-focusing magnetic-sector mass spectrometer of the Mattauch-Herzog geometry. Ions were dispersed according to the square root of their mass in a 0.94 T magnetic field. A time and position sensitive multi-channel plate detector with a delay line anode recorded the position and time relative to the photolysis pulse for each ion. The time resolution of the detector and electronics was ~ 20 ns and the overall time resolution of the experiment including sampling from the pinhole was ~ 50 μs. The mass resolution varied, but for the usable data in Runs 1 and 2 it was 0.70 amu FWHM.

The $C_2H_5O_2$ system was investigated during three separate runs, and the CH_3O_2 and $C_3H_7O_2$ systems were each tried for one run. The precursor chemistry, photolysis laser, and number of averages for each data set are described for each of the RO_2 below. All measurements were performed at room temperature. Each data set also had a signal calibration run where a mixture of known concentrations of ethene, propene, and cis-2-

butene was flown through the cell so that a calibration factor relating counts to concentration could be determined.

3.2.1 $C_2H_5O_2$ system

3.2.1.1 Run 1 (02/27/08–02/28/08)

During Run 1 two types of precursor chemistry were used; Oxalyl chloride (OxCl)/ethane/oxygen mixtures, and diethyl ketone (DEK)/oxygen mixtures. Ethyl radicals were either generated by reaction of Cl, from photolysis of OxCl,with ethane,[6]

$$(\mathrm{ClCO})_2 \xrightarrow{h\nu\ (248)} \mathrm{Cl} + \mathrm{CO} + \mathrm{ClCO}^* \tag{3.10}$$

$$\mathrm{ClCO}^* \longrightarrow \mathrm{Cl} + \mathrm{CO} \tag{3.11}$$

$$\mathrm{Cl} + \mathrm{C_2H_6} \longrightarrow \mathrm{HCl} + \mathrm{C_2H_5} \tag{3.12}$$

or by photolysis of DEK.[7-9]

$$(\mathrm{C_2H_5})_2\mathrm{CO} \xrightarrow{h\nu\ (248\ \mathrm{nm})} \mathrm{C_2H_5} + \mathrm{C_2H_5CO}^* \longrightarrow 2\mathrm{C_2H_5} + \mathrm{CO} \tag{3.13}$$

In both generation methods the ethyl radicals went on to react with oxygen to form $C_2H_5O_2$ by reaction (3.6).

The concentrations for the OxCl chemistry in molecules cm^{-3} were, $O_2 = 1.3 \times 10^{16}$, OxCl = 5.0×10^{14} (vapor pressure of 30 Torr at 2 °C), and $C_2H_6 = 1.3 \times 10^{15}$. The helium (He) bath gas was varied to reach total pressures over the range 1 – 6 Torr. Four data sets were taken for the branching ratio measurements with the synchrotron energy set to 10.7 eV. The flash photolysis was done using a KrF excimer laser at 248 nm. 7500 photolysis pulses were averaged at a repetition rate of 4 Hz. One photoionization efficiency (PIE) scan was also performed over the synchrotron energy range 8.6 – 10.7

eV with a 0.025 eV step size and 250 photolysis pulses per step. It was performed at a total pressure of 4 Torr with the same concentrations as the single energy runs.

The DEK chemistry used the same O_2 and He bath concentrations as well as 1.6 x 10^{13} DEK (vapor pressure of 10 Torr at 17.2 °C).[10] Pressure was varied over the range 1 – 6 Torr, and the synchrotron radiation and flash photolysis laser were set to 10.7 eV and 248 nm respectively. Three data sets were taken, and 5000 – 7000 photolysis pulses were averaged for each data set. No PIE scan was done with the DEK chemistry.

3.2.1.2 Run 2 (03/08/08)

Only OxCl chemistry was used for the four branching ratio data sets in this run. Data was taken at total pressures of 4 and 6 Torr. OxCl concentrations were one order of magnitude lower than Run 1, i.e., 5.0 x 10^{13} molecules cm^{-3}. O_2 was the same except for one run at 6 Torr where O_2 was increased to 4.9 x 10^{16} to look for any competition between reactions (3.4) and (3.8). The synchrotron radiation was set at 10.7 eV and three out of four runs were done with flash photolysis at 248 nm. One data set was also done at 193 nm to ensure that there were no complications from reaction of $ClCO^*$ in the 248 nm photolysis. At 193 nm there is no evidence for a stable intermediate, and the net yield of 2Cl + 2CO is reached immediately.[11] The two 6 Torr data sets averaged 3750 photolysis pulses, the 4 Torr/248 nm data set averaged 7500 photolysis pulses, and the 4 Torr/193nm data set averaged 2000 photolysis pulses. An additional data set was taken at a synchrotron radiation of 11.1 eV and 193 nm photolysis where it was possible to observe the photoionization of OxCl. The depletion of the OxCl signal after photolysis was observed to check the alignment of the excimer laser, and insure the expected absorption occurred.

3.2.1.3 Run 3 (12/04/08–12/07/08, poor mass resolution)

During this run the effect of total radical concentration and O_2 were explored. High and low concentrations of each were explored at total pressures of both 4 and 6 Torr. Data on 12/04 was mistakenly taken at one order of magnitude lower O_2 concentration than expected due to the incorrect assignment of mass flow controller in the data acquisition program. The data at 6 Torr of total pressure were taken again at the correct O_2 concentrations. Further experimental problems during this run led to inadequate mass resolution for the products of interest, making reliable branching ratio measurements difficult.

3.2.2 CH_3O_2 system

Acetone/O_2 precursory chemistry was used for the generation of CH_3O_2 radicals. The much slower reaction of chlorine radicals with methane prevents the use of OxCl/CH_4/O_2 precursor chemistry for this system. Similar to the DEK chemistry photolysis of acetone is the radical source. At 193 nm the photodissociation is almost exclusively through one product channel.[12]

$$\mathrm{CH_3COCH_3} \xrightarrow{hv,193\ nm} \mathrm{2CH_3} + \mathrm{CO} \quad (>95\%) \tag{3.14}$$

Single photoionization energy data sets using 10.9 eV light were taken at 1 and 4 Torr total pressure. Acetone and O_2 were fixed at 3.8 x 10^{13} and 5 x 10^{16} molecules cm^{-3}, respectively. Acetone was brought into the cell by flowing He through a bubbler filled with acetone held at -31 °C and total pressure 750 Torr. 6000 shots were averaged for each data set. One PIE data set was also taken at 4 Torr total pressure over the range 10 – 11.5 eV. 400 shots per step were taken at a step size of 25 meV. An ArF excimer laser was the source of the 193 nm photolysis pulse, and operated at 4 Hz.

3.2.3 $C_3H_7O_2$ system

For studying the propyl peroxy self reaction both OxCl/C_3H_8/O_2 and Dipropyl ketone (DPK)/O_2 precursor chemistries were used. The OxCl chemistry was not as straightforward in this case because two different H abstraction pathways were in competition leading to two different propyl peroxy radicals. There was a 50/50 split between the primary and secondary propyl radical production,[13] and this led to a variety of products in the self and cross reactions of these two peroxy radicals.

$$\mathrm{Cl + C_3H_8 \longrightarrow CH_2CH_2CH_3 + HCl\ (\sim 50\%)} \tag{3.15}$$

$$\mathrm{\longrightarrow CH_3CHCH_3 + HCl\ (\sim 50\%)} \tag{3.16}$$

Photolysis of DPK also produced propyl radicals but the yield of reaction (3.17) was not known and other product channels existed.[14]

$$\mathrm{C_3H_7COC_3H_7} \xrightarrow{hv, 193\ nm} \mathrm{2C_3H_7 + CO} \tag{3.17}$$

The concentrations for the OxCl chemistry in molecules cm^{-3} were, O_2 = 1.3 x 10^{16}, OxCl = 5.0 x 10^{14}, and C_3H_8 = 1.3 x 10^{15}. A He bath gas brought the total pressure to 1, 4, and 6 Torr. The three single photoionization energy data sets were done at 10.6 eV. The photolysis laser was a KrF excimer at 248 nm operating at 4 Hz, and 2000 – 2500 shots were averaged for each data set. A PIE scan over the range 8.6 – 10.3 eV was also performed at 4 Torr total pressure. The energy resolution was 25 meV and 200 shots were taken at each step.

The DPK chemistry used precursor concentrations of DPK = 1.25 x 10^{13} (V.P. 0.7 Torr at 19 °C)[10] and O_2 = 2.6 x 10^{16} molecules cm^{-3}. A He bath brought the total pressure to 1 or 4 Torr. The three single photoionization data sets were done at 10.6 eV. The photolysis laser was the ArF excimer at 193 nm and 4 Hz repetition. 5000 shots were averaged for each single energy data set. A PIE scan was done over the range 9.2 – 10.65 eV at a total pressure of 4 Torr. 400 shots per step at a step size of 25 meV were taken for the PIE.

3.3 Results and analysis

This work attempted to measure α for three RO_2 self reactions. A successful measurement was made for $C_2H_5O_2$, and preliminary work was completed for CH_3O_2 and $C_3H_7O_2$. The α value was determined by photoionization mass spectrometry of the time resolved stable end products of the reaction, e.g., acetaldehyde (CH_3CHO), ethanol (C_2H_5OH), and ethyl hydroperoxide (C_2H_5OOH) for the case of the $C_2H_5O_2$ self reaction. Ratios of these products provided a measure of α, as did kinetics fitting to the absolute concentration time profiles. PIE curves were used to help identify products. In addition the first PIE curves of the three ROOH were also measured.

Using equations (ii) and (iii) it was possible to determine α from the ratio of R'CHO and ROH. This relied on assuming the steady state approximation for the concentration of RO in the RO_2 self reaction scheme (3.1) – (3.8), and neglecting reaction (3.3). The observations of ROOR appeared to be from secondary sources in this data so neglecting (3.3) was justified.

$$\alpha = \frac{R-1}{R+1} \qquad \text{ii}$$

$$R = \frac{[\mathrm{R'CHO}]}{[\mathrm{ROH}]} \qquad \text{iii}$$

It was also necessary to know the photoionization cross section of each species to convert the raw value of *R* from the ratio of counts to the ratio of concentrations. The cross sections used were: HCHO = 6.78 Mb and CH_3OH = 1.85 Mb at 10.9 eV,[15,16] CH_3CHO = 7.97 and C_2H_5OH = 3.90 Mb at 10.7 eV,[15,17] C_2H_5CHO = 9.93 Mb and 1-C_3H_7OH = 4.80 Mb at 10.6 eV,[15,18] and CH_3COCH_3 = 11.10 Mb and 2-C_3H_7OH = 0.63 Mb at 10.6 eV.[15] A correction for detection efficiency based on the square root of the mass was also applied when species with large mass differences were compared.[19]

The kinetics fitting method to determine α requires converting counts to the absolute concentrations in order to fit the kinetics of the observed time traces. Calibration data sets for each run were used to determine a calibration factor that converted counts to concentration with the following equation,

$$[\text{Concentration}] = \frac{S}{\sigma * n_{ph} * \Delta t_{bin} * C * \sqrt{m_i}}$$

where *S* is the signal in counts $amu^{0.5}$ $timebin^{-1}$ $experiment^{-1}$ cm^{-1}, σ is the photoionization cross section in MegaBarns (cm^2 $molecules^{-1}$), n_{ph} is the number of photons in photons s^{-1}, Δt_{bin} is the width of an acquisition time bin in s, *C* is the number of coadded shots, and m_i is the mass in amu of the species. This factor was then scaled for each data set and each species being detected using the appropriate cross section.

Other product ratios were also of interest.

$$R_{A/EH} = \frac{[\text{R'CHO}]}{[\text{ROOH}]}$$

$$R_{E/EH} = \frac{[\text{ROH}]}{[\text{ROOH}]}$$

Without having an independent source for the cross sections of the ROOH it was not possible to make quantitative measurements with these ratios, but they provided insight into the overall reaction mechanism and any deviations from expected behavior.

Single ionization energy runs provided 3D data blocks with the number of counts recorded against axes m/z and time. The data were then examined in a variety of ways. One way was to integrate counts over one m/z unit to look at the time profile of a single mass as is shown in **Figure 3-2**. In each panel one mass has been isolated. A background signal was recorded prior to the self reaction chemistry that was initiated by the excimer laser at 20 ms. The reaction proceeds for ~ 80 ms until the pump out of the reaction flow cell starts to influence the concentration profiles at ~ 100 ms. The remaining trace from 100 – 150 ms follows the pump out of the flow cell. An alternative view of this data, shown in **Figure 3-4**, involved integrating the counts over the time period of the reaction (20 – 100 ms) to look at the full mass spectrum. Both of these views combined with looking at 3D plots allowed careful examination of the data.

PIE data was collected as a 4D data block with the additional axis of photon energy. Three different 3D blocks could be extracted from this data for analysis similar to what was just described for the 3D block at a single photoionization energy. The most common extraction was a 3D block with axes of photon energy and m/z, where the counts have already been integrated along the time axis throughout the 20–100 ms reaction period. This data was then further reduced to look at the mass spectrum or the PIE curve of single masses as shown in **Figure 3-3**.

3.3.1 $C_2H_5O_2$ self reaction

Three different runs were performed on the $C_2H_5O_2$ self reaction. A successful measurement of α was made based off of the results from Runs 1A and 2.

3.3.1.1 Run 1A (OxCl chemistry)

The large number of shots averaged and large radical concentrations led to good signal-to-noise for the OxCl chemistry. No pressure dependence was observed from 1 – 6 Torr in the reaction products. Some higher molecular weight and unknown masses were observed in addition to the expected products. The value for α was successfully determined by both kinetics fitting and *R*.

3.3.1.1.a Observed Products

Figure 3-2 shows the time traces of four stable products from the $C_2H_5O_2$ chemistry including simultaneous kinetic fits using the FACSIMILE program.[20] The products CH_3CHO, C_2H_5OH, and C_2H_5OOH were all observed as expected, and all displayed similar time dependences. Ethene (C_2H_4) from reaction (3.7) was also observed. Its time dependence resembled a step function as it was not produced or consumed after its initial production. Not shown in the figure, C_2H_5 was identified as coming from dissociative ionization of $C_2H_5O_2$ because of its reactant time profile. One feature to note is that the pump out of the flow cell was incomplete for both C_2H_5OH and C_2H_5OOH over the same time scale that it completed for the other two products. The data shown is from the 6 Torr total pressure run, but similar results were observed at 1, 2.5, and 4 Torr as well.

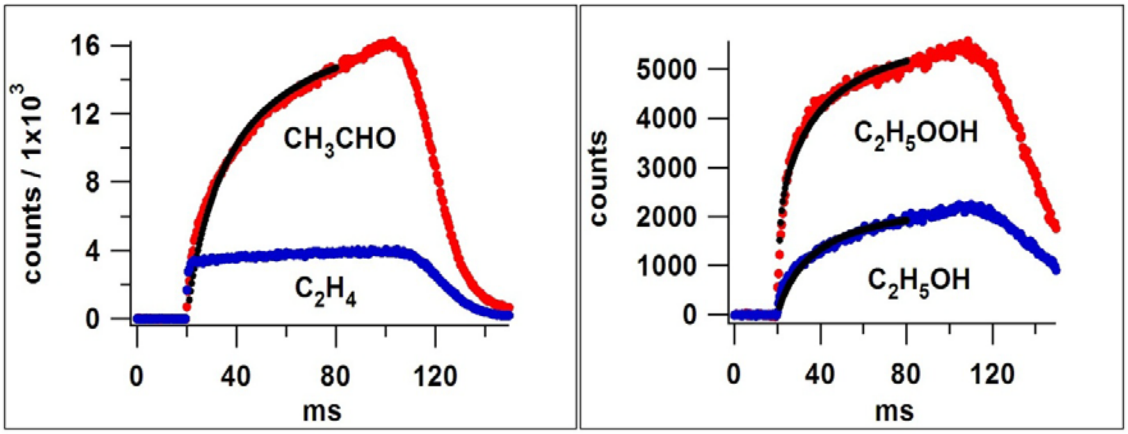

Figure 3-2. Four stable products of the $C_2H_5O_2$ self reaction from OxCl initiation chemistry. The excimer fired at 20 ms and pump out starts ~ 100 ms. The pump out of the ethanol and ethyl hydroperoxide products does not complete on the same time scale as the other two products.

Species assignments were confirmed by looking at the PIE curves and comparing them with the literature. Panel B in **Figure 3-3** shows the comparison between this work and papers by Cool et al. for CH_3CHO and C_2H_4.[15,17] This work did not measure an absolute cross section, but was scaled to the cross sections given in the Cool et al. paper at 10.7 eV for comparison purposes. Good agreements between the curves allowed for definitive identifications. In panel C the agreement between the C_2H_5OH traces was not as good. The qualitative shapes were similar, but the appearance energies were different. The mass resolution in this region was not as good for the PIE data set as shown in Panel A around m/z 46 (C_2H_5OH). It was clear that other masses were likely present as contaminants, but the single energy data sets used for the kinetics analysis, shown in **Figure 3-4**, had much better mass resolution so the qualitative agreement for the ethanol PIE was considered sufficient for identification. No previous PIE for C_2H_5OOH was found in the literature, but the data shown in Panel D had an appearance energy of ~ 9.6 eV in agreement with a first ionization energy of 9.65 eV determined by Li et al. with photoelectron spectroscopy.[21] The cross section values for C_2H_5OOH were determined by scaling to a value measured at 10.7 eV during Run 2, and will be discussed later during the results from Run 2.

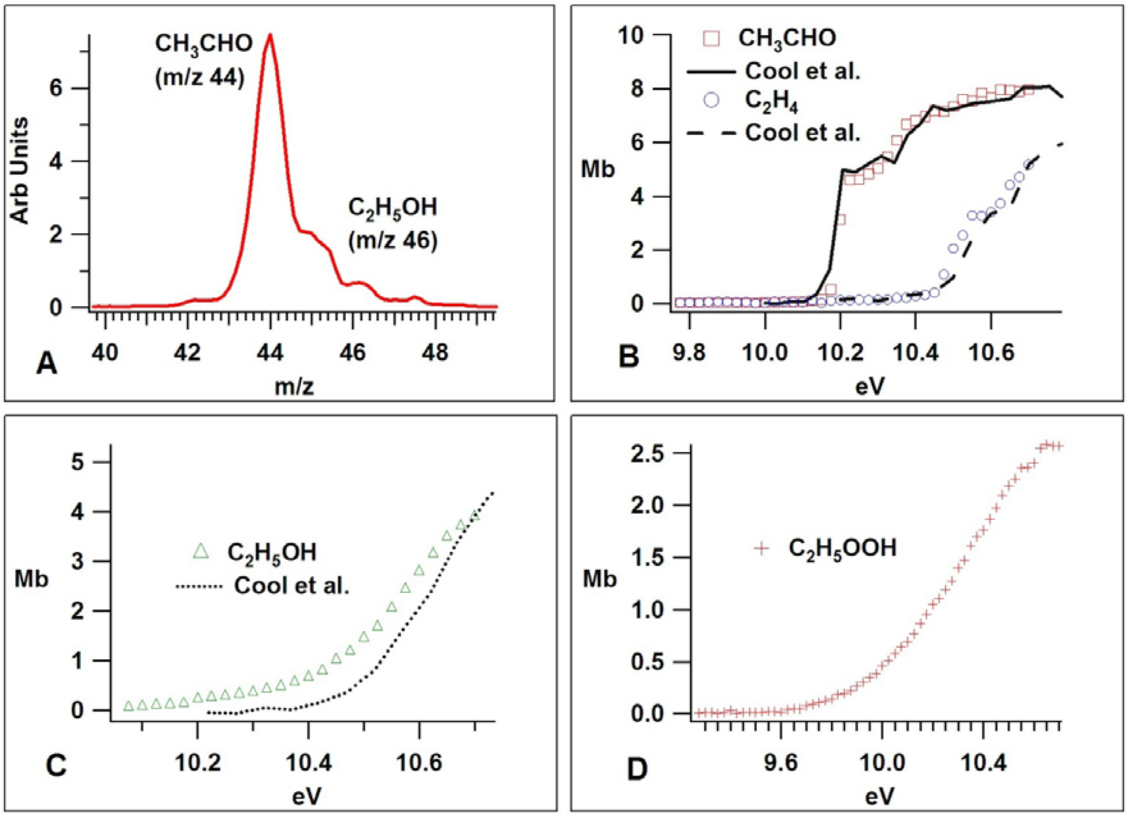

Figure 3-3. (A) 1-D mass spectrum from the PIE data set; the mass resolution was not good in the 4X region. (B) PIE of acetaldehyde and ethene both agreed well with literature. (C) Mass contamination appears to have caused a discrepancy in the ethanol PIE. (D) PIE of ethyl hydroperoxide; the cross section was determined by normalization to the cross section determined using Run 2 data at 10.7 eV.

The mass spectra from the four different pressure data sets provided further information about the product distribution and are shown in **Figure 3-4**. The mass resolution in this data was much improved over the PIE data, but there was a slight shift in the mass calibration so the peaks are ~0.5 amu above their actual masses. The peaks in the figure are all analogous to the ones labeled in the 1 Torr panel. In every case there was a significant peak at m/z 45 when the two dominant peaks were expected to be CH_3CHO and C_2H_5OH. While a ^{13}C and ^{2}H isotope peak of CH_3CHO existed it would have been a much smaller fraction (~ 2.8%) based on natural abundances. One other feature in **Figure 3-4** is the large m/z 43 peak in the 6 Torr data. It only appeared in this one data set, but it was a signal not a background interference. Other data sets also had one or two unique masses, but only the masses common to every data set have been fully investigated.

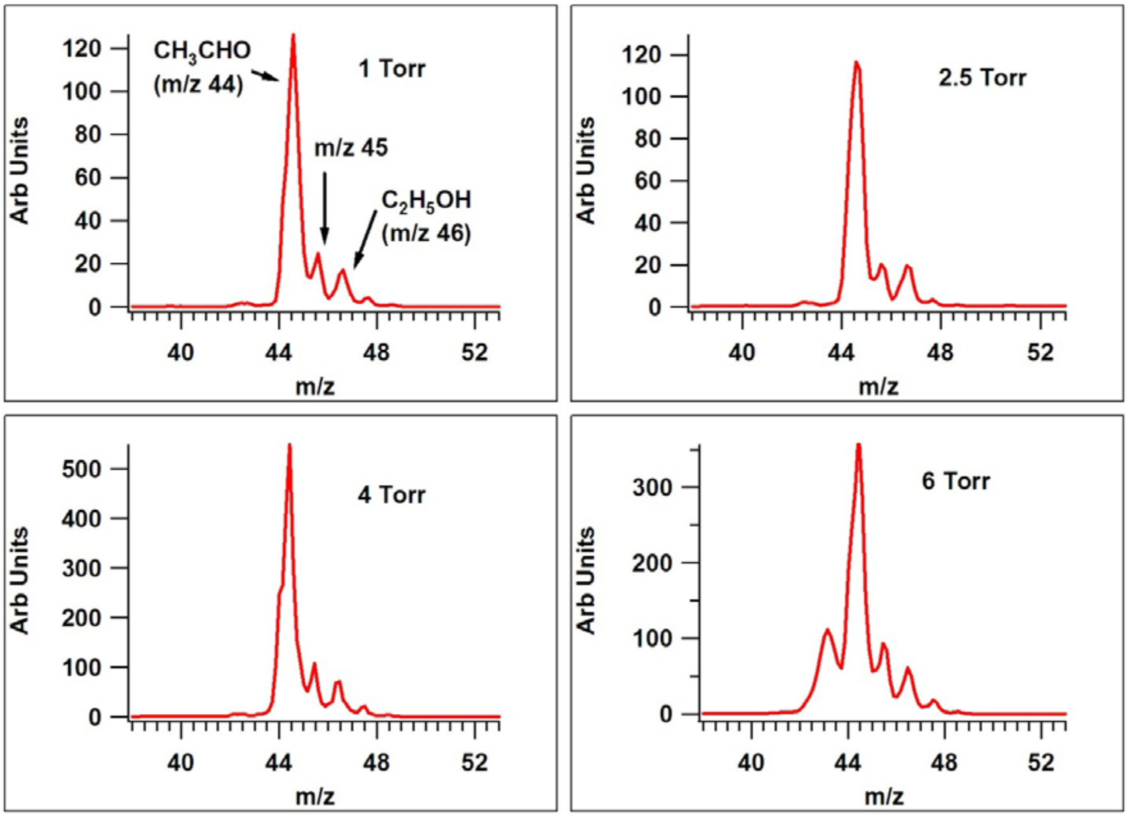

Figure 3-4. 1-D mass spectra of four different pressures; similar peaks are labeled as shown in the 1 Torr panel. m/z 45 peak was much larger than expected based on isotopic abundances. m/z 43 in the 6 Torr panel is also unknown.

The time trace of m/z 45, shown in **Figure 3-5**, looked like a stable product similar to CH_3CHO and C_2H_5OH ruling out a significant radical contribution to the peak. The product at m/z 45 was not the only unexplained product mass. The time traces of some other unexplained masses m/z 105, 89, 60, and 59 are also shown in **Figure 3-5**, and they had clear product time traces as well. Observation of m/z 89 initially suggested that reaction (3.3) forming diethyl peroxide (m/z 90) may not be negligible. However the m/z 89 product was slower to form than the others indicating that it might have been formed by secondary chemistry and not directly through channel (3.3). In fact there are other isomers at m/z 90 that could explain the observed products including the hemiacetal product in reaction (3.18).

$$\mathrm{CH_3CHO + C_2H_5OH \xrightarrow{surface} CH_3CH(OH)OC_2H_5} \qquad (3.18)$$

There was further evidence for this type of chemistry due to a product peak at m/z 105 which may have been the peroxy-hemiacetal (m/z 106) formed from reaction (3.19).

$$\mathrm{CH_3CHO + C_2H_5OOH \xrightarrow{surface} CH_3CH(OH)OOC_2H_5} \qquad (3.19)$$

Peroxy-hemiacetal formation is a well known acid and base catalyzed process in organic chemistry. Work from Tobias et al. has seen evidence of this chemistry happening on the surface of aerosols making it possible that the walls of this experiment could provide the surface necessary to catalyze these reactions.[22]

In each case above the predicted masses, 90 and 106, were actually detected at one mass unit lower, i.e., 89 and 105, respectively. This was most likely due to a small mass calibration error at high mass, but another possibility is that both lost H atoms during the ionization. For simplicity they will be referred to as m/z 90 and 106 from here on except in figures where they will be labeled both ways.

The time traces shown in **Figure 3-5** provide clues as to what products might have been linked through dissociative ionization pathways. The initial growth in the time trace of m/z 45 agreed well with the trace at m/z 106 suggesting that the peroxy hemiacetal might split at the O-O bond after ionization leading to a $C_2H_5O^+$ ion by reaction (3.20).

$$\mathrm{CH_3CH(OH)OOC_2H_5} \xrightarrow{hv\ 10.7\ eV} \mathrm{CH_3CH(OH)O} + \mathrm{C_2H_5O^+} + e^- \qquad (3.20)$$

A companion mass at m/z 60 had a similar time trace indicating that ionized acetic acid and ethanol might also form through reaction (3.21).

$$\mathrm{CH_3CH(OH)OOC_2H_5} \xrightarrow{hv\ 10.7\ eV} \mathrm{CH_3COOH^+} + \mathrm{C_2H_5OH} + e^- \qquad (3.21)$$

The slower appearance of the time trace at m/z 90 did not match well with the time traces of any of the unidentified lower mass products, preventing any clear link from being made. The time trace of m/z 106 and m/z 59 were nearly identical, suggesting that 59 came from 106. The assignment of m/z 59 was not obvious, but might also be linked to the products in reaction (3.21).

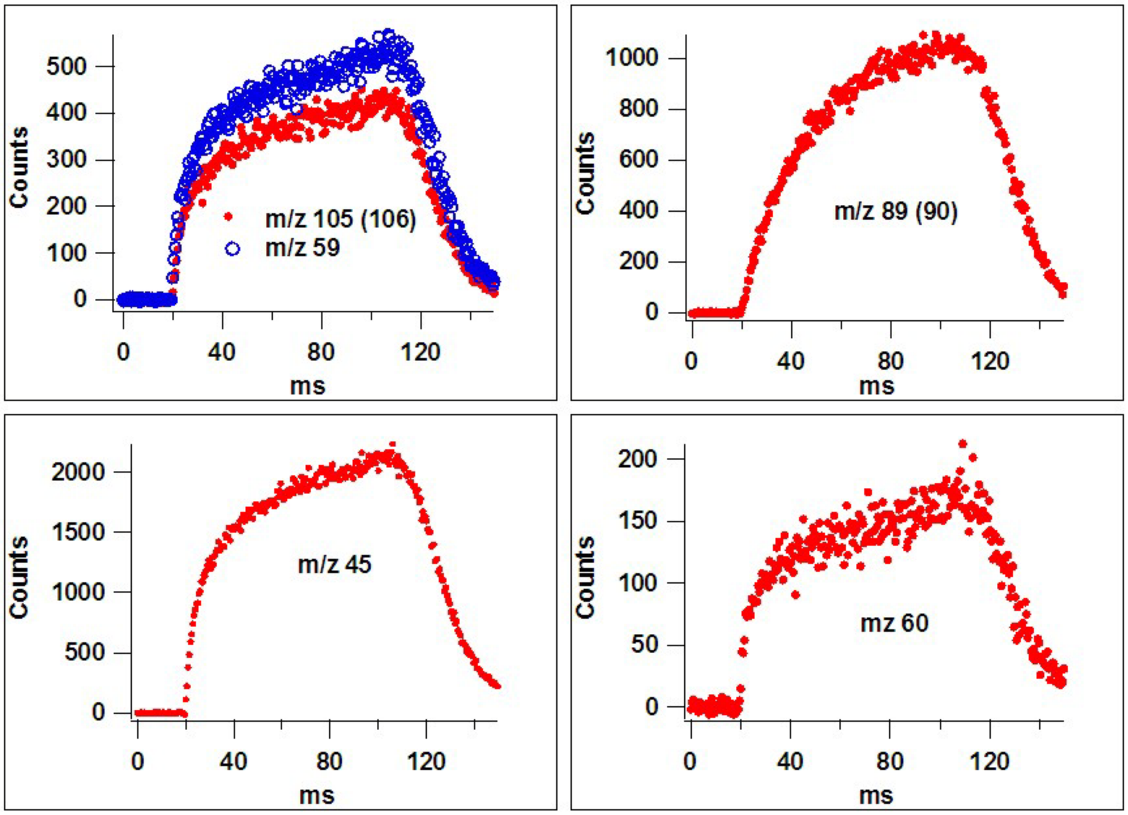

Figure 3-5. Some of the unidentified products and their likely parents at m/z 106 and 90

The PIE curves of these masses also provided information about how they were connected, but it was limited because of the mass contamination already indentified for C_2H_5OH in panel A of **Figure 3-3**. A unique mass must have been present in the PIE of m/z 45 because it appeared well before both acetaldehyde and ethanol as shown in panel A of **Figure 3-6**. Acetaldehyde contamination was subtracted out of the PIE due to its clear interference at around 10.2 eV where it characteristically jumps up. There may have also been ethanol contamination but no subtraction was made. The general curve of the remaining PIE at m/z 45 does not mirror the ethanol PIE, shown in **Figure 3-6** for comparison, and there is no characteristic shape for ethanol that would signal its presence. The best guess PIE for m/z 45 is shown next to the PIE curves from m/z 106, 90, 60, and 59 in panel B. Both m/z 90 and 106 appeared at lower energy than m/z 45, 59, and 60 indicating that they were possible parents. In the inset of panel B it is shown that m/z 45 and m/z 60 have very similar appearance energies. This is in agreement with the time traces that suggested dissociation channels (3.20) and (3.21) were complimentary. In addition m/z 60 appeared well before the known appearance energy of acetic acid at 10.6 eV, so m/z 60 could not be attributed to acetic acid formed through other chemistry.[23] The appearance of m/z 59 did not happen until higher energy indicating a different pathway was needed for its formation.

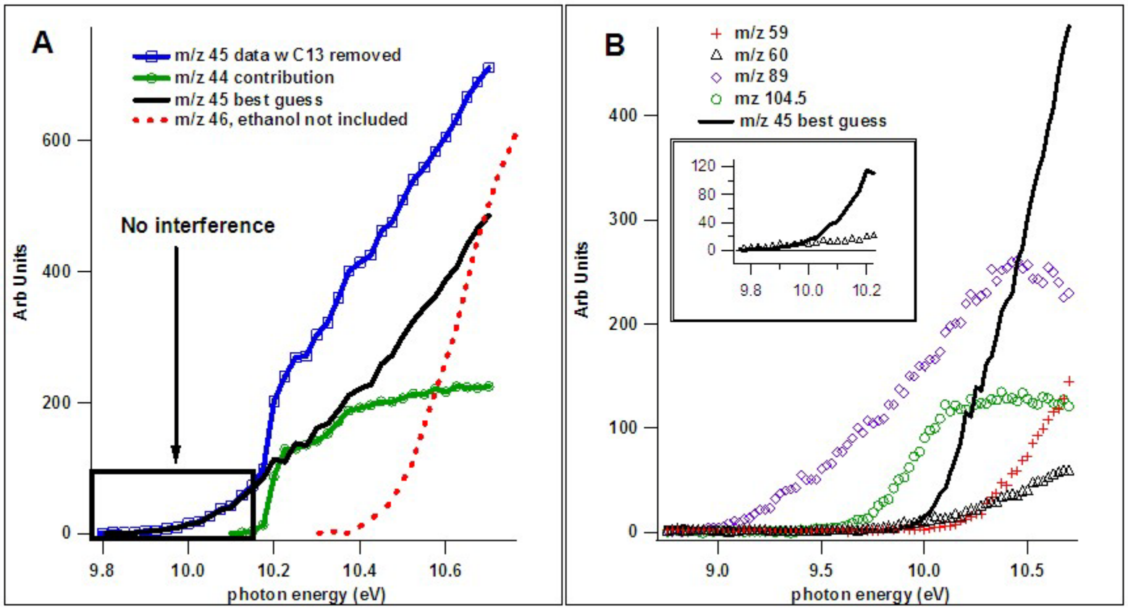

Figure 3-6. (A) Removing acetaldehyde mass contamination from m/z 45 PIE. Ethanol was not removed, but is shown for comparison. (B) A comparison of the PIE curves for the larger masses and some of their possible dissociation products.

Table 3-1 lists all of the reproducible masses observed and their species assignments where possible. Description explains whether the species time trace looked like a reactant, product, or a step function (e.g., a product that comes up almost instantly at the firing of the excimer due to its formation from the initiation chemistry, but is neither created nor destroyed in the subsequent reactions). Two species which have not already been mentioned are butene (C_4H_8) and butane (C_4H_{10}). Both had time traces indicating initial formation at the firing of the excimer, but then no further reaction. Recombination of C_2H_5 radicals may have been the source of one or both species. The butene PIE was not in exact agreement with the PIEs in the literature so some doubt in this assignment remains.[18,24] An excited $(CO)_2^+$ from OxCl photolysis might also appear at this mass. Butane did not appear in the PIE data set because of insufficient signal-to-noise, but it has an appearance energy of 10.53 eV and so would have been observed during the kinetics data sets at 10.7 eV where much more averaging was done.[18]

Table 3-1. All the reproducible masses identified in Runs 1A and 2 as well as their species assignment and a description of how their time trace appeared.

Run 1A (m/z)	Run 2 (m/z)	Species	Description
28	28	$C_2H_4^+$	Step function
29	29	$C_2H_5^+$ (from $C_2H_5O_2^+$)	Reactant
44	44	CH_3CHO^+	Product
45	45	$C_2H_5O^+$ (From dissoc) And $^{13}C/^2H$	Product
46	46	$C_2H_5OH^+$	Product
47	47	? And $^{13}C/^2H$	Step function, small product
56		$C_4H_8^+$	Step function
58		$C_4H_{10}^+$	Step function
59		? (From dissoc)	Product
60		CH_3COOH^+ (From dissoc)	Product
62	62	$C_2H_5OOH^+$	Product
89 (90)	89 (90) sometimes	$C_2H_5OOC_2H_5$ or $CH_3CH(OH)OC_2H_5$	Product
105 (106)		$CH_3CH(OH)OOC_2H_5$	Product

3.3.1.1.b Measurement of α

Using the assigned product masses the simplest way to measure α was to use equations (ii) and (iii); determining *R* from the ratio of the CH_3CHO and C_2H_5OH time profiles. **Figure 3-7** shows a plot of the time trace of *R*. In each case a stable ratio was reached after ~ 20 ms validating the steady state approach used. The results spanned the range $\alpha = 0.52 – 0.58$.

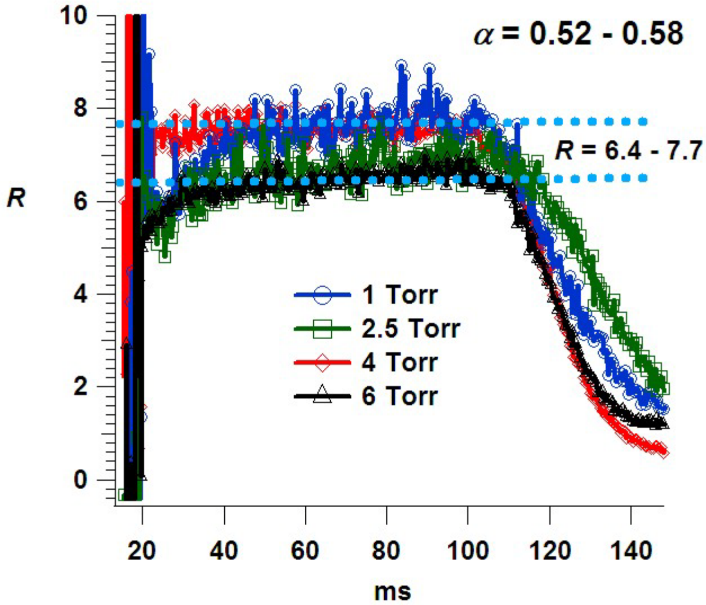

Figure 3-7. Ratio of CH_3CHO counts to C_2H_5OH counts and value for α that was determined from the ratios at the four pressures 1, 2.5, 4, and 6 Torr.

As shown in **Figure 3-2**, α was also measured by performing kinetics fits to the time traces using the calibration factor to determine absolute concentrations. This method agreed well with the *R* method. The calibration factor was not well known (the slits on the micrometer were changed during the calibration run leading to an unknown amount of photons) so the absolute kinetics were uncertain, but the relative nature of α meant that the fitted parameter was robust no matter what calibration factor was used to translate counts into concentration. (e.g., The total self reaction rate constant for one data set varied over the range $9.65 \times 10^{-14} – 3.07 \times 10^{-13}$ cm^3 molecules^{-1} s^{-1}, using a calibration factor that also varied by a factor of three, but α only varied over the range 0.532 – 0.579)

3.3.1.1.c Other product ratios: $R_{A/EH}$ and $R_{E/EH}$

The other ratios $R_{A/EH}$ and $R_{E/EH}$ provided more information about the progress of the reaction. **Figure 3-8** shows both ratios, neither was constant in time and both increased prior to the pump out that started at ~ 100 ms. From the ratios it was especially clear that the products were not pumping out at the same rate. $R_{A/EH}$ got much smaller throughout the pump out showing that CH_3CHO was being removed the fastest, and $R_{E/EH}$ got much larger showing that C_2H_5OH was removed the slowest. There were also changes in the ratios with pressure, but this was expected. The branching fraction between reaction (3.6) and reaction (3.7) is pressure dependent, so the initial amount of C_2H_5OOH will also be pressure dependent. Without knowing the photoionization cross section a value for α can not be independently determined from this data.

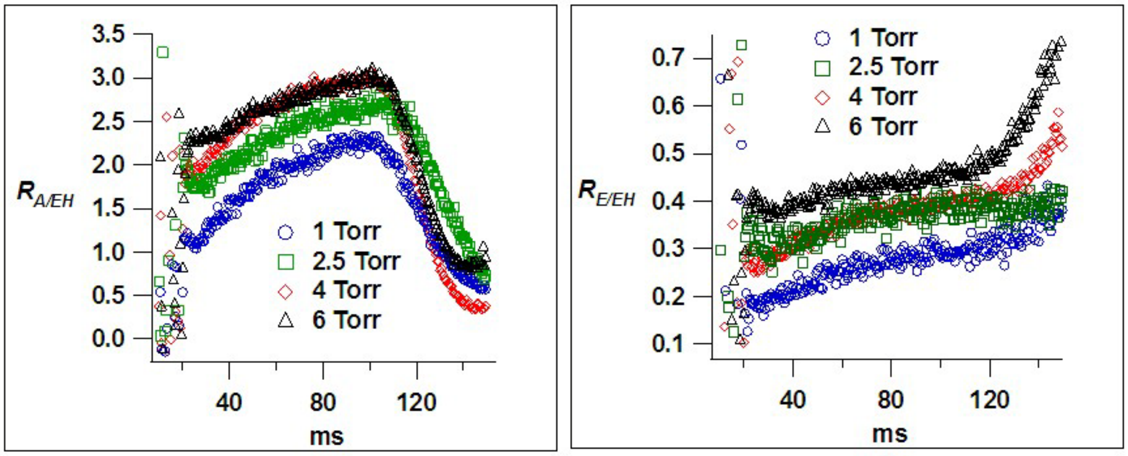

Figure 3-8. Ratios of [CH_3CHO] / [C_2H_5OOH] and [C_2H_5OH] / [C_2H_5OOH] in the left and right panels respectively. Behavior during the pump out shows that the products had different retention in the flow cell.

3.3.1.2 Run 1B (DEK chemistry)

The DEK precursor chemistry was also tried during Run 1. The total radical concentration was ~ 1 order of magnitude lower than the OxCl chemistry in Run 1A, largely due to the smaller photolysis cross section of DEK. The DEK chemistry was an interesting comparison because Cl was not needed due to the direct production of ethyl radicals from photolysis. A strange distribution of products meant that a measurement of α was not reliable.

3.3.1.2.a Observed Products

The reactants and products, C_2H_5, CH_3CHO, C_2H_5OH, and C_2H_5OOH shown in **Figure 3-9**, were observed during the DEK data sets. The time traces did not all have the same shape. The C_2H_5 had a sharp initial drop followed by a slower reaction that looked like the $C_2H_5O_2$ self reaction. C_2H_5OH counts jumped up very quickly and then only increased marginally for the rest of the reaction time. The C_2H_5OOH appeared to form a little bit more slowly than everything else. Only the CH_3CHO has the characteristic time trace expected. In addition the amount of C_2H_5OOH was also quite large, nearly equaling the CH_3CHO trace, but during the OxCl chemistry in Run 1A CH_3CHO was ~ 3 times greater than the C_2H_5OOH. The data shown here are for the 6 Torr data but similar results were obtained for the 4 and 1 Torr data sets, albeit with lower signal-to-noise ratios.

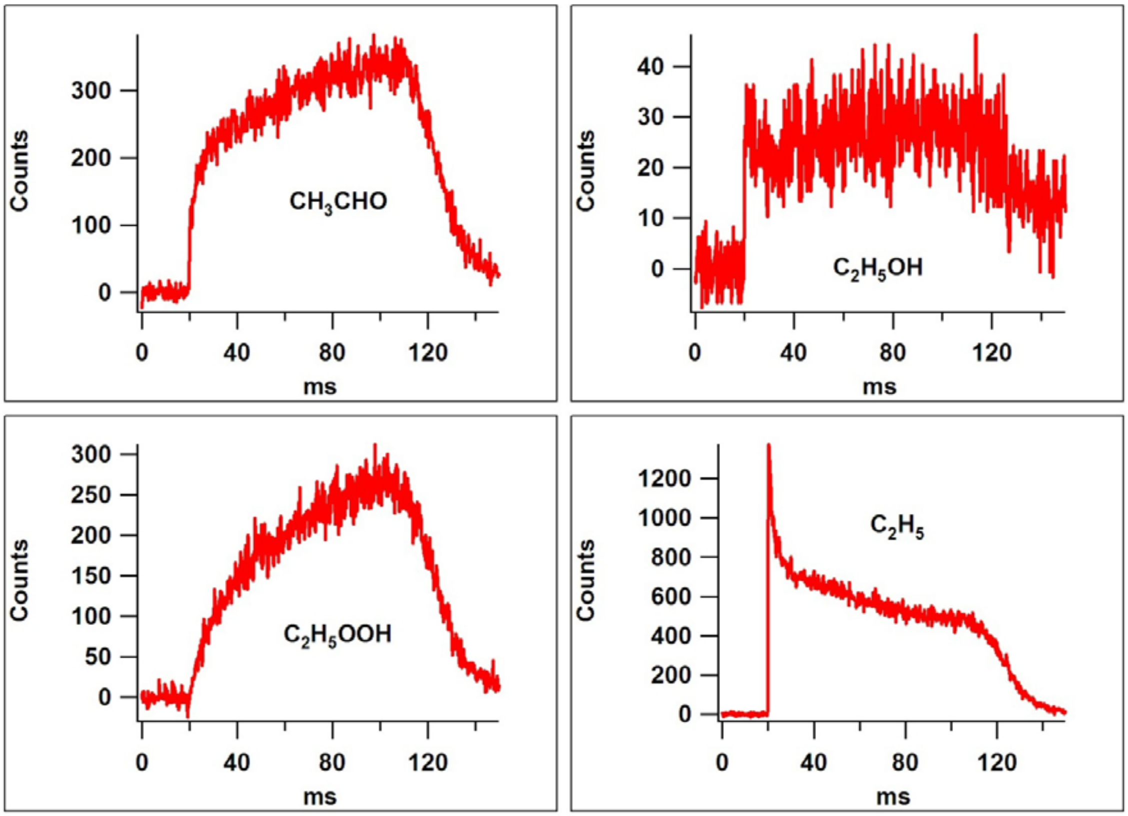

Figure 3-9. Expected products and reactants of $C_2H_5O_2$ self reaction using the DEK precursor chemistry. Time traces do not all appear the same, and are different from the behavior they showed in the OxCl chemistry.

The results from the DEK chemistry also had unexplained mass peaks. **Figure 3-10** shows the mass spectrum from the 6 Torr data set. The peaks at m/z 45 and 47 were as large or larger than the C_2H_5OH peak at m/z 46. Their time traces are shown in the next panel where m/z 47 appeared as a step function, and m/z 45 grows in as a product after an early transient peak. Both of these peaks well exceed what would be expected from natural isotopic abundances. There was also a new prominent peak at m/z 42 which reacted away with time. It was not possible to look for the larger mass products (m/z 90 and 106) because the ion optics were tuned so that anything larger than DEK (m/z 86) would not hit the detector to avoid saturation from the DEK signal. This made it hard to determine whether the unexpected mass peaks came from a larger parent. No PIE data was taken with this chemistry so it was not possible to identify the products that way either. A data set was taken that verified photodepletion of the DEK signal before it was tuned off the detector, and indicated there was a good photolysis laser alignment.

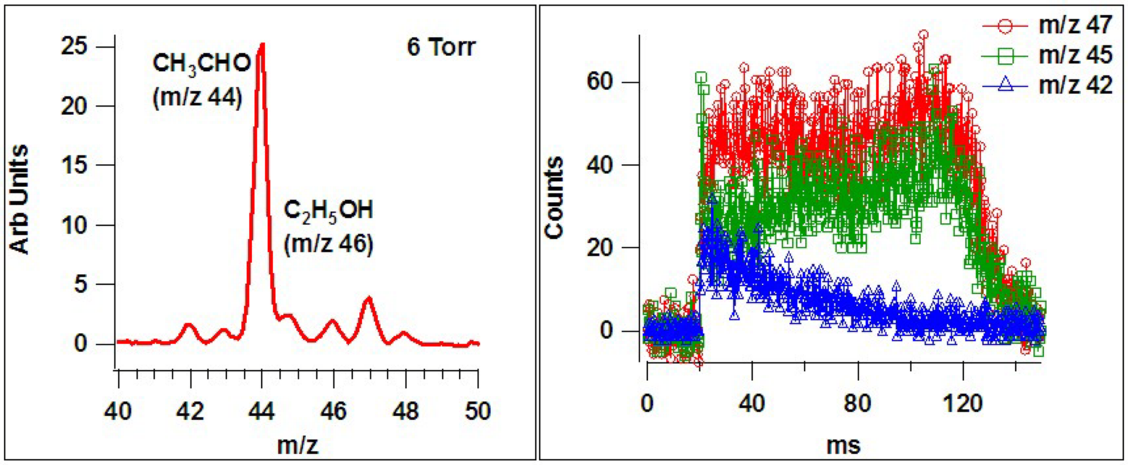

Figure 3-10. 1-D mass spectrum from DEK chemistry, and time traces of selected masses

3.3.1.2.b Measurement of α

The strange mass distribution around the critical product masses combined with low signal-to-noise from the lower radical concentration meant that α from this data was not reliable. This data was not considered for the overall measurement of α for the $C_2H_5O_2$ self reaction.

3.3.1.3 Run 2

In Run 2 the OxCl chemistry at ~ 1 order of magnitude lower radical concentrations (~ 1 x 10^{13} molecules cm^{-3}) was explored. One data set was also taken to determine if changing the O_2 concentration would have an effect. Good measurements of α were made with few unknown product masses observed.

3.3.1.3.a Observed Products

The product masses CH_3CHO, C_2H_5OH, C_2H_5OOH, and C_2H_4 were all observed and are shown in **Figure 3-11**. The C_2H_5 reactant trace also was observed as expected. In this OxCl run the product masses all pumped out at the same time unlike during Run 1A. The product time traces have similar qualitative shapes except for the CH_3CHO which appeared to jump up earlier. No PIE was taken during this run so the species assignments from Run 1A were used.

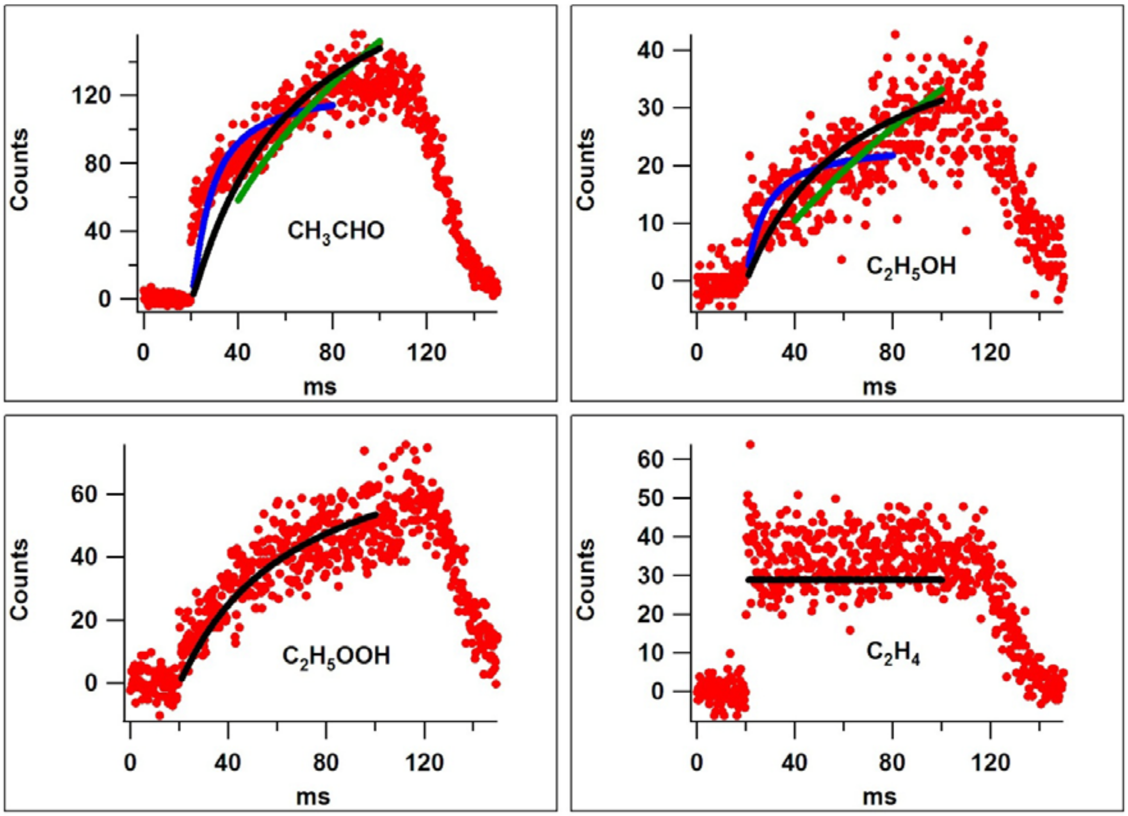

Figure 3-11. Stable products from the 6 Torr, 248 nm, high O_2 data set in Run 2. Different time scale fits are shown, as well as when the fit to ethyl hydroperoxide is included along with an initial HO_2 constraint from the ethene.

In **Figure 3-12** the mass spectrum of each data set around m/z 40 is shown. Clear resolution of the individual peaks was seen. The peaks at m/z 45 and 47 were much smaller than the expected product peaks at m/z 44 and 46. They were still not quite as small as would be expected from isotopic abundances, but with careful removal of the tails of the neighboring peaks they are only slightly larger. The time trace of m/z 45 is not shown but still resembled a stable product. Comparing the top two panels shows no observable difference between flash photolysis at 193 nm and 248 nm. There was also no qualitative difference from the addition of extra O_2 as can be seen by comparing the bottom two 6 Torr panels. The quantitative differences will be discussed shortly.

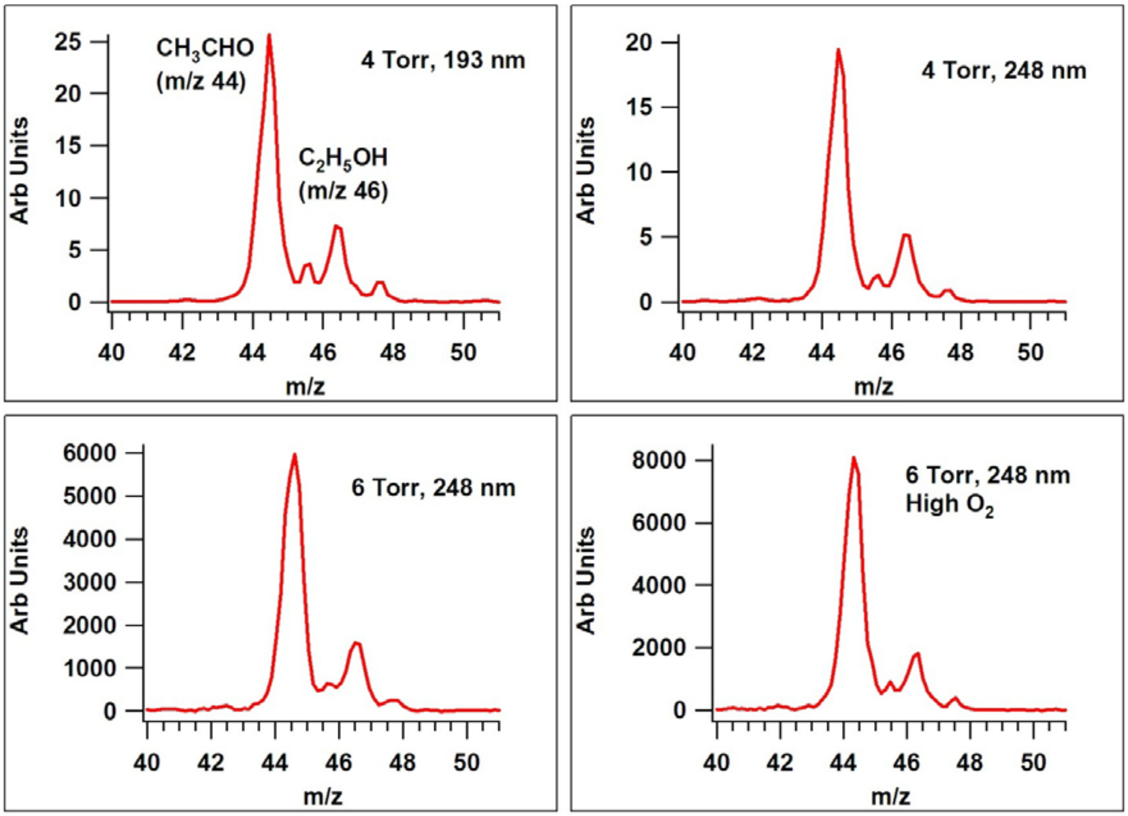

Figure 3-12. 1-D mass spectra in the m/z 4X range from the four data sets taken during Run 2. All the peaks are labeled analogously to the first panel. m/z 45 and 47 are much smaller than m/z 44 and 46, as expected.

There were not as many additional masses observed during Run 2. The product at m/z 90 was not conclusively observed in every run. **Figure 3-13** shows the observed time traces for m/z 90 for the four different data sets. The 6 Torr data in the bottom two panels was taken last and no m/z 90 was observed. The variable nature of the detection makes it likely that it resulted from a secondary process. There was also no detection of m/z 106 in any of the data sets from Run 2. **Table 3-1** lists all of the observed masses during Run 2 in comparison with all of the observed masses from Run 1A.

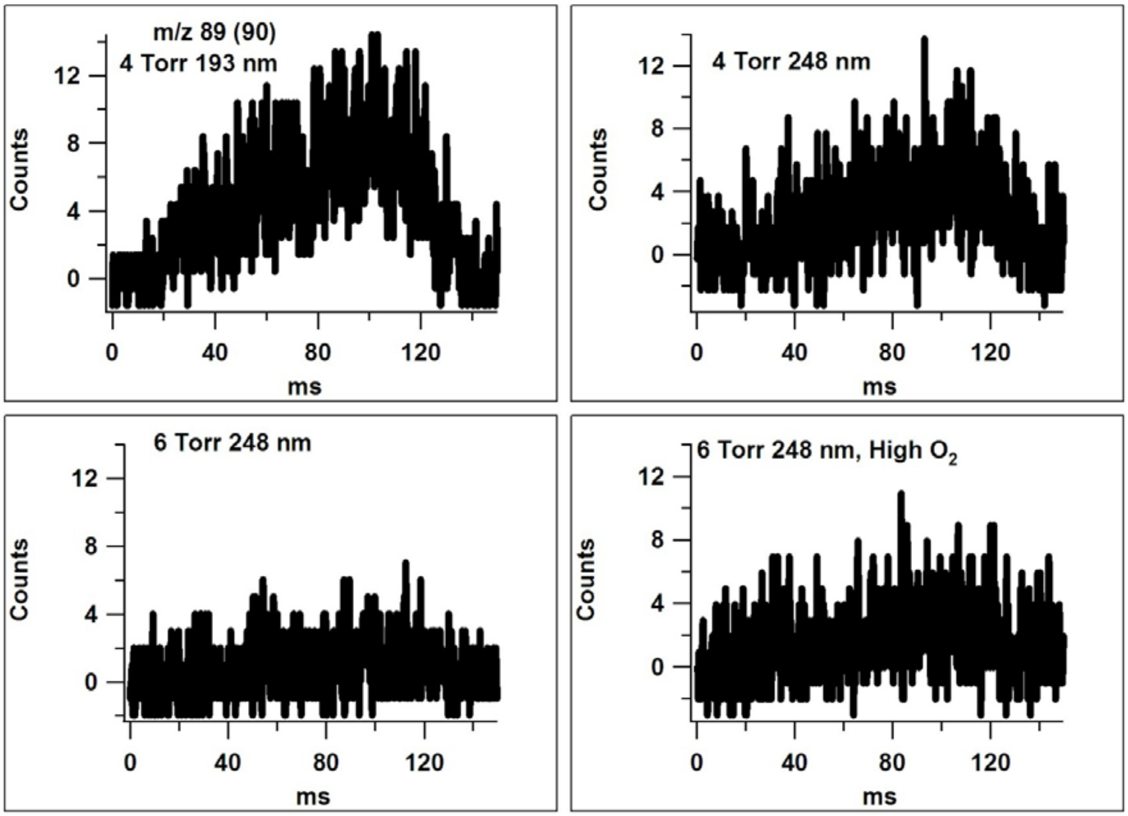

Figure 3-13. m/z 90 was not observed in every data set. The sporadic detection indicated that it was likely a secondary product, not one produced in the $C_2H_5O_2$ self reaction.

3.3.1.3.b Measurement of α and O_2 dependence

Similar to Run 1A, α was determined by both kinetic fitting and looking at *R*. The kinetic fits are plotted with the time traces in **Figure 3-11**. In all the kinetics fits shown the value for α did not change substantially despite the clear differences in the fits. The blue and green fits were done over different time ranges, and the black fits included the C_2H_5OOH and C_2H_4 data as well. As in Run 1A the rate constant values were too large, ~ 3 x 10^{-13} cm^3 $molecules^{-1}$ s^{-1}, to be considered realistic using the concentration factors derived from the calibration gas data set. The relative nature of α meant that it did not depend on these concentration factors as previously discussed for Run 1A. The value for

α from the kinetics fits is 0.34 ± 0.06. The value was determined as an average of all four data sets and the quoted errors are the standard deviation of those measurements.

The signal-to-noise for these data was lower than in Run 1A (predominantly due to the lower radical concentration), and was especially evident when looking at *R* as shown in **Figure 3-14**. It was less clear cut what should be taken as the value for *R*, so a linear fit was performed over the time range 60 – 100 ms, (the area inside the pink box) and the average value of the linear fit was taken for *R*. The average of the four data sets leads to α = 0.33 ± 0.08, where the quoted errors are the standard deviation of the four measurements. The values for α obtained from the kinetics fits and *R* for each individual data set are shown in **Table 3-2**. The individual errors for α from *R* were determined by taking the high and low *R* value determined from the linear fit just described, and the error from the kinetics fitting was determined by the range of α determined in the different types of fits.

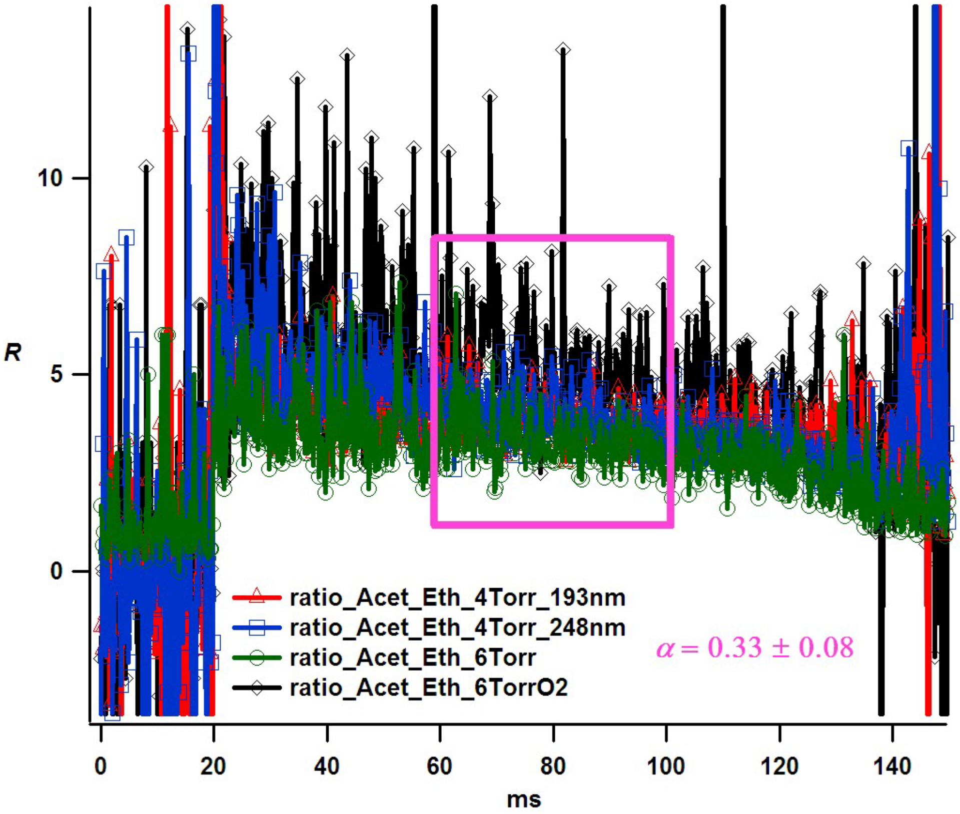

Figure 3-14. *R* plotted for the four data sets of Run 2. The area within the pink box (60–100 ms) is the region used for determining the *R* and the corresponding α for each data set. The average value for α determined is also stated in pink.

The O_2 dependence of this reaction was also investigated with the two data sets at 6 Torr. Competition from reaction (3.8) might have interfered with the end product analysis at low O_2 concentrations so a higher O_2 concentration was also tried at 6 Torr. The value for α does change with the addition of extra O_2 as can be seen in **Table 3-2**. The additional O_2 in the carrier gas led to lower signal-to-noise making it difficult to determine how robust this effect was with only the one data set including the variation. This signal-to-noise effect was evident in the initial radical determined in **Table 3-2** for the high O_2 run. Nothing except the O_2 concentration was changed from the previous run but using a similar calibration factor returned an initial radical concentration a factor of two lower. In reality (and in parenthesis for Img_020) the radical concentration would have been approximately the same as the previous run, but the extra O_2 led to less of the sample from the pinhole making it into the ionization region of the instrument.

Table 3-2. Conditions and α values measured for each of the data sets in Run 2

Run	P (Torr)	Laser (nm)	# of Shots	$[C_2H_5]$ / 10^{13}	$[O_2]$ / 10^{16}	α from *R*	α from kinetics
Img_014	4	193	2000	2.8	1.3	0.31 ± 0.03	0.28 ± 0.02
Img_018	4	248	7500	1.1	1.3	0.32 ± 0.03	0.32 ± 0.02
Img_019	6	248	3750	1.0	1.3	0.24 ± 0.06	0.31 ± 0.02
Img_020	6	248	3750	0.45 *(1.0)*	4.9	0.43 ± 0.06	0.42 ± 0.02

3.3.1.3.c C$_2$H$_5$OOH photoionization cross section

The kinetics fits in black in **Figure 3-11** that included the C_2H_5OOH and C_2H_4 data were also used to determine the photoionization cross section of C_2H_5OOH relative to the other products. The C_2H_4 data constrained the initial amount of C_2H_5 radicals and the initial amount of HO_2 through the known branching ratio between reaction (3.6) and (3.7). The α value measured from CH_3CHO and C_2H_5OH determined the additional amount of secondary HO_2. Assuming that C_2H_5OOH only forms through reaction (3.5) a determination of the C_2H_5OOH cross section for the data was then possible because the absolute concentrations of all the sources of C_2H_5OOH were known. The photoionization cross section at 10.7 eV was determined to be 2.57 Mb. This measurement was then used to scale the PIE curve taken in Run 1A to provide cross sections for the range 8.6 – 10.7 eV. The error on this measurement will be discussed further in the discussion section.

3.3.1.3.d Other product ratios: $R_{A/EH}$ and $R_{E/EH}$

The other ratios, $R_{A/EH}$ and $R_{E/EH}$, were also looked at for Run 2, and are shown in **Figure 3-15**. The ratios showed the same overall shape starting out larger before settling at a plateau. While both CH_3CHO and C_2H_5OH pumped out more quickly than C_2H_5OOH the change was not as dramatic as in Run 1. It was possible to check for self consistency in the data by using the photoionization cross section derived from this data to determine α from these ratios. This was complicated by the fact that a large amount of the C_2H_5OOH in this data comes from the initial HO_2 formed in reaction (3.7). After a best guess subtraction of the initial C_2H_5OOH the data was used to determine α, and consistency within the results was observed.

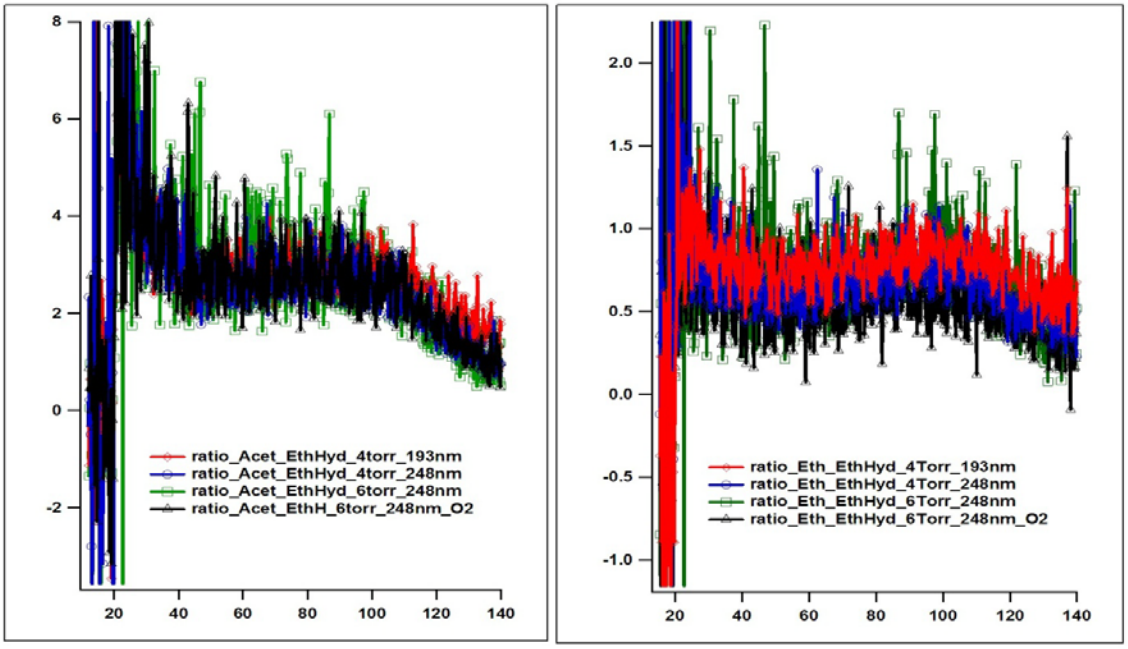

Figure 3-15. The ratio of CH_3CHO/C_2H_5OOH and C_2H_5OH/C_2H_5OOH for the four data sets in Run 2

3.3.1.3.e Differences in radical concentration

The absolute concentrations have been checked by comparing the OxCl depletion at 11.1 eV and determining a total Cl concentration of 3.3×10^{12} molecules cm^{-3} for the 193 nm photolysis runs. This was almost an order of magnitude lower than the value of

2.8×10^{13} estimated from the concentration of C_2H_4 observed and assuming a branching fraction of 0.13 for reaction (3.7).[25,26] The reason for this discrepancy was unknown, but the observed rate of reaction was consistent with the higher concentrations determined from the calibration factor, suggesting that more OxCl may have been present than expected.

3.3.1.4 Run 3

The main goal of this run was to further investigate the role that O_2 and total radical concentrations have on the measured value of α. It was discovered too late that problems with the experimental apparatus had led to unusable data sets. **Figure 3-16** shows the mass resolustion from around the main product peak m/z 44 and 46 for four data sets during Run 3. It was not possible to make a clear distinction of each mass so it was not possible to determine the appropriate ratio. Individual shift corrections (the alignment of counts from alike masses that appear curved in the raw data) were done for each data set, but this did not improve the data significantly. For now this data has not been used.

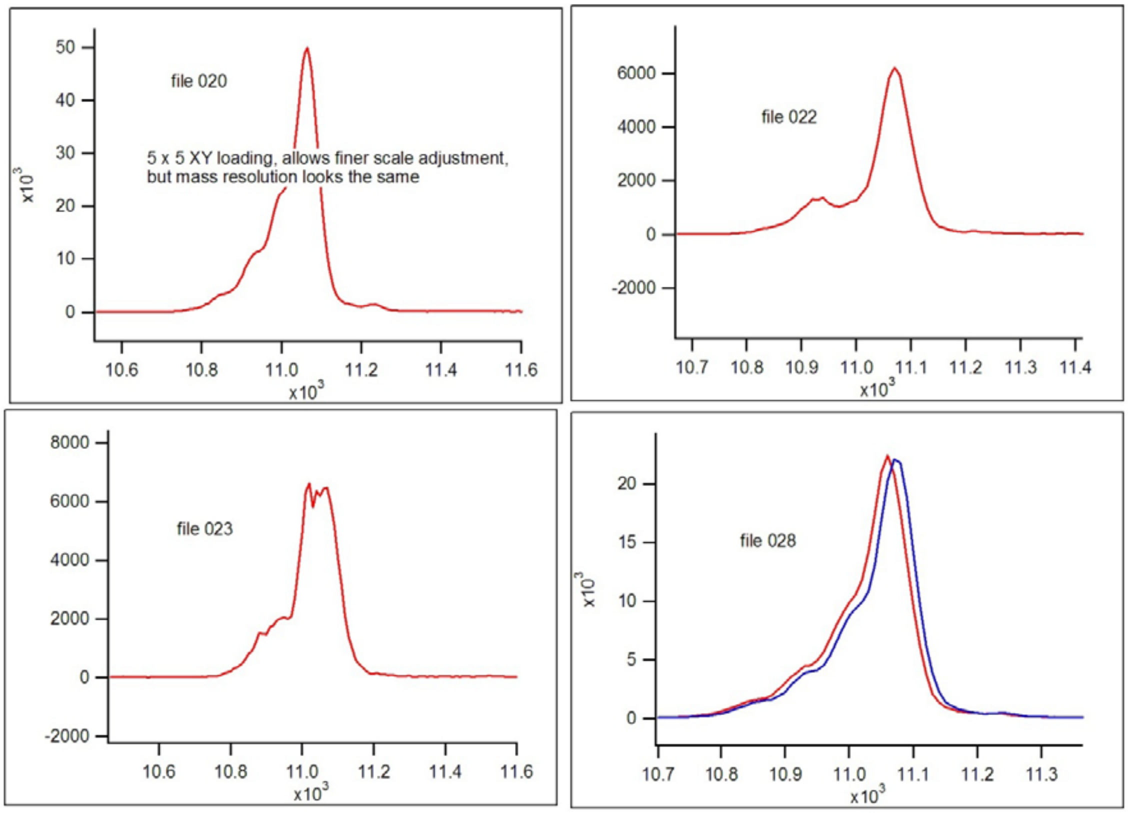

Figure 3-16. The mass resolution in the 4X range for Run 3 is very poor, as shown in four different data sets.

3.3.2 CH_3O_2 self reaction

Acetone photolysis was used as the precursor chemistry for the CH_3O_2 self reaction. The expected products were identified, and a preliminary measurement of α was made using one 4 Torr data set with sufficient signal to noise. More data is needed to confirm the value.

3.3.2.1 Observed Products

The major products formaldehyde (HCHO), methanol (CH_3OH), and methyl hydroperoxide (CH_3OOH) were all observed and are shown in **Figure 3-17**. In addition the reactant methyl peroxy (CH_3O_2) itself was observed, unlike in the case of ethyl or propyl, because it has a stable cation at m/z 47 and does not dissociatively ionize until higher energies.[27] There was an interference at m/z 32 which was visible in the CH_3OH signal as a transient species very early in the time trace. A small sulfur contamination from the previous run may have been responsible. The pump out portion of all the time traces looked similar as well. The 1 Torr data set is not shown, but looked qualitatively the same although it had much poorer signal-to-noise.

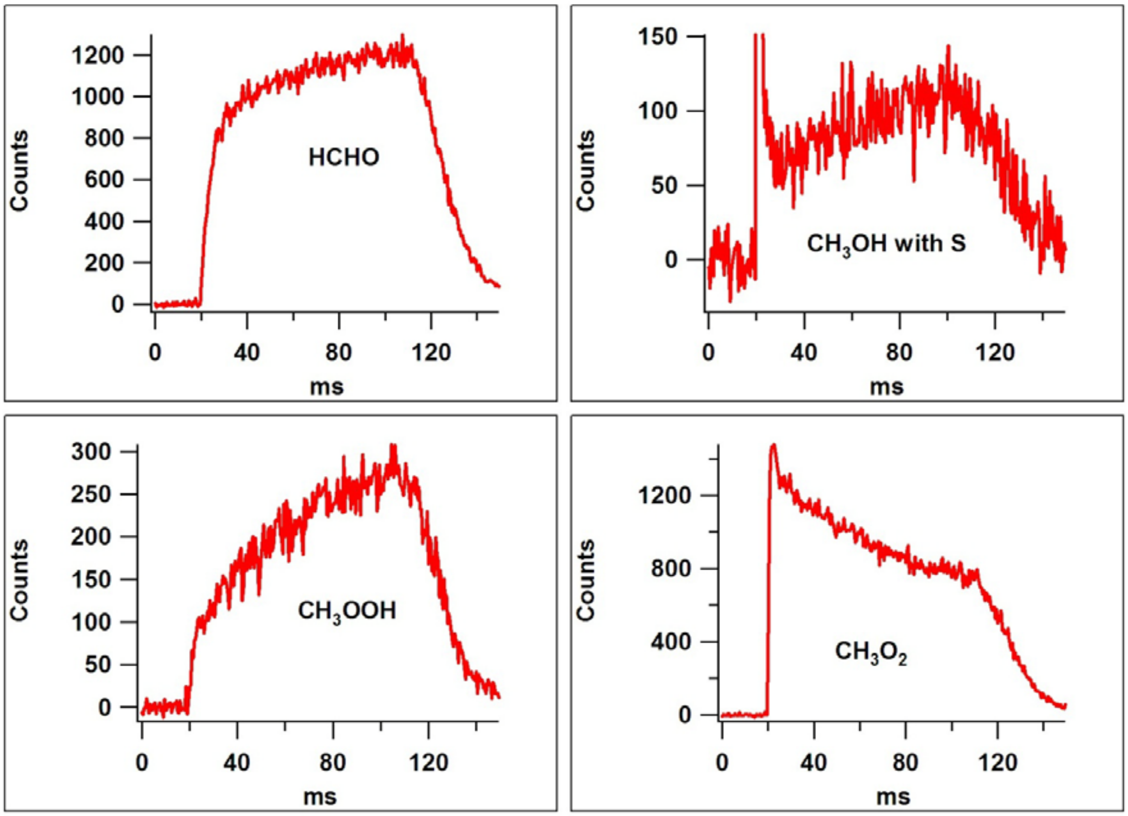

Figure 3-17. The three major products – HCHO, CH_3OH, and CH_3OOH – along with the reactant CH_3O_2 from the methyl peroxy self reaction.

The products were confirmed by their PIE scans and comparison to the literature where possible. Absolute cross sections were not measured, but the PIEs were normalized to the literature value of the cross section at 11.4 eV for comparsion of the overall shapes shown in **Figure 3-18**. There was good agreement between the qualitative shape from the present measurement of HCHO and CH_3OH and the work of Cooper et al. and Cool et al., respectively.[15,16] There are no previously reported PIE curves for CH_3OOH, but from photoelectron spectroscopy Li et al. report a first ionization energy of 9.87 eV.[21] We did not measure low enough in energy to confirm this measurement, but at 10.0 eV the signal was not quite extinguished suggesting that the first ionization is < 10.0 eV. There are no previously reported cross sections for CH_3O_2 either, but the PIE curve measured here was in good agreement with previous work from the same instrument.[27]

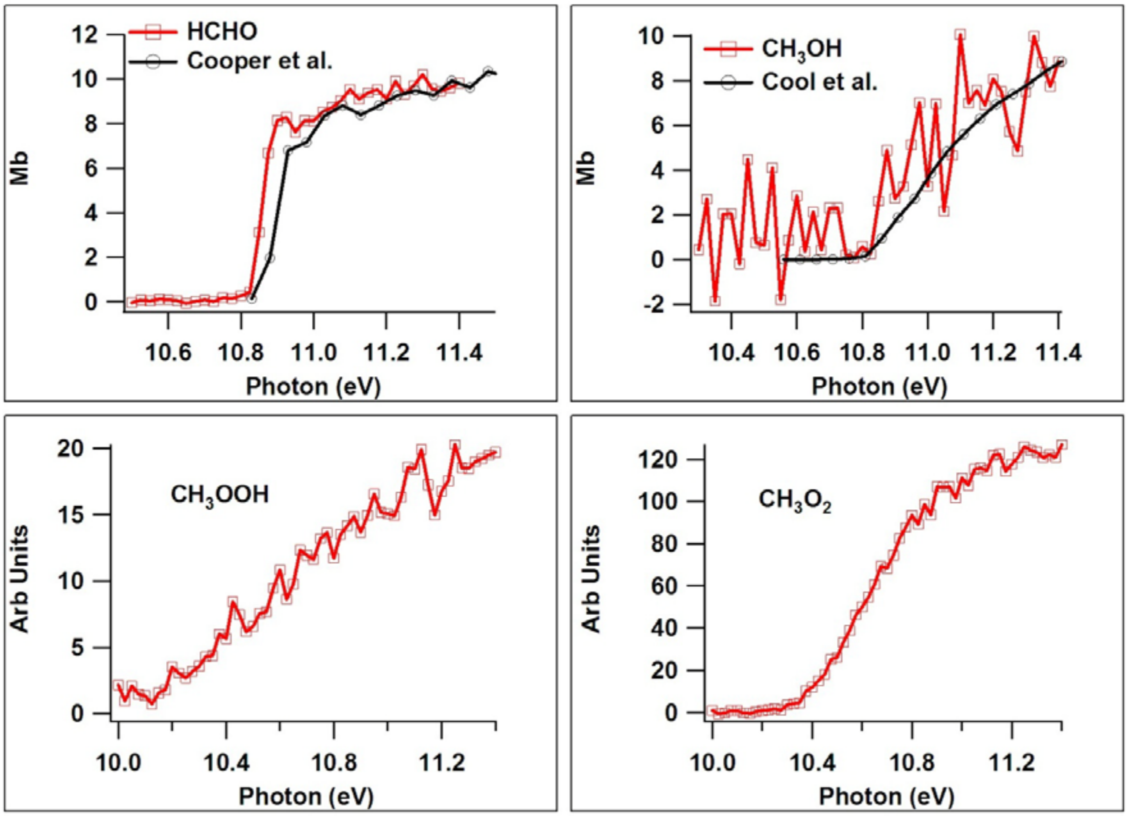

Figure 3-18. PIE scan of major reactants and products of CH_3O_2 self reaction. Absolute cross sections were not measured, but scans were normalized to literature value at 11.4 eV for comparison where possible.

There was good mass resolution for these data sets as is shown in panel A of **Figure 3-19**. The small peak at m/z 31 between HCHO and CH_3OH has a magnitude corresponding to the expected isotope ratio of HCHO. A depletion was observed as expected at the CH_3CO fragment from dissociative ionization of the acetone precursor. Masses larger than m/z 58, where the precursor acetone was found, could not be reliably measured because the ion optics were adjusted to move m/z 58 to the edge of the detector to prevent signal saturation.

3.3.2.2 Measurement of α

For the CH_3O_2 self reaction *R* = [HCHO]/[CH_3OH]. Unfortunately only the data taken at 4 Torr had sufficient signal-to-noise to determine α so only the one measurement shown in panel B of **Figure 3-19** was made. From this data $\alpha = 0.53 \pm 0.03$.

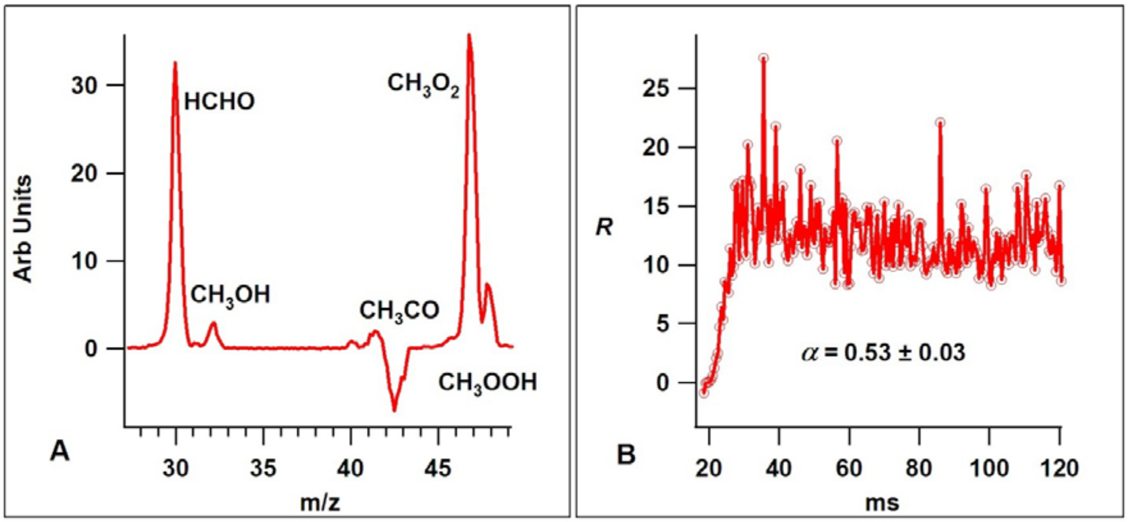

Figure 3-19. A. Mass resolution of the major reactants and products was good. B. *R* = [HCHO]/[CH_3OH] for the CH_3O_2 self reaction and allowed measurement of α.

3.3.3 $C_3H_7O_2$

Both OxCl and DPK chemistries were used to generate $C_3H_7O_2$ radicals, and both had problems with product identification. The OxCl chemistry also had high molecular weight species and differing pump out traces for different products. Neither chemistry provided a reliable measurement of α.

3.3.3.1 Run 1A (OxCl chemistry)

3.3.3.1.a Observed Products

The results from the OxCl chemistry for the $C_3H_7O_2$ self reaction show the expected major products and reactants. **Figure 3-20** shows the time traces for the carbonyl (C_2H_6CO) , alcohol (C_3H_7OH), hydroperoxide (C_3H_7OOH) and propyl radical (C_3H_7) from the dissociative ionization of propyl peroxy ($C_3H_7O_2$). The pump out portion of the time traces for C_3H_7OH and C_3H_7OOH were very different from the C_2H_6CO and the C_3H_7. Over the time period observed there was almost no removal of the former compared with almost complete removal of the latter. The data shown is for the 6 Torr data set, but the 4 Torr and 1 Torr data also mimicked this behavior.

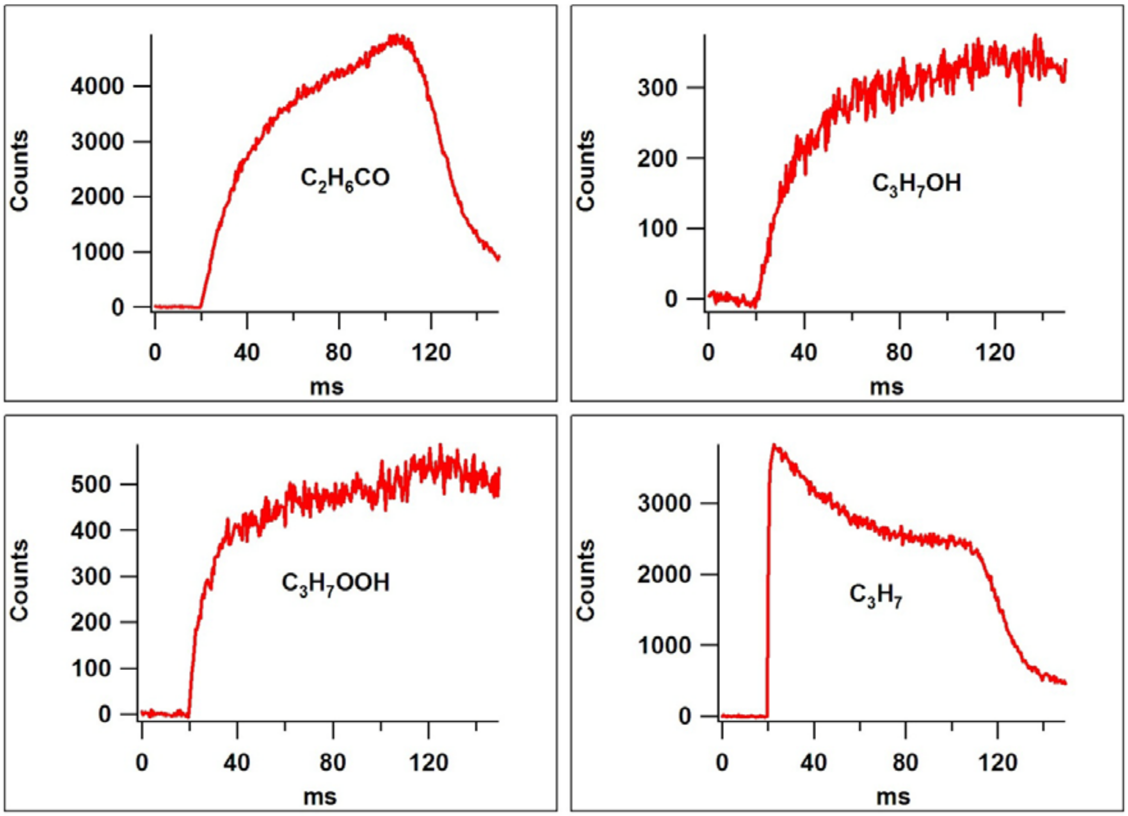

Figure 3-20. Major products and reactants for $C_3H_7O_2$ self reaction using the OxCl precursor chemistry.

Identification by PIE was more complicated in this case because both C_2H_6CO and C_3H_7OH were most likely a combination of isomers from the two different propyl peroxy radicals. The C_2H_6CO (m/z 58) PIE could be reasonably well reproduced by a

10:1 mixture of the propanal and acetone PIE curves as shown in **Figure 3-21**. Another way to determine the acetone contribution would have been through its dissociative ionization at m/z 43. However whatever product signal may have been there was swamped by the dissociative ionization of the reactant $C_3H_7O_2$, as can be seen in the reactant time trace in **Figure 3-20**. The identification of m/z 43 as C_3H_7 was further confirmed by the PIE curve which started well before 10.3 eV, the beginning of the dissociative ionization of acetone. It was not possible to get as good agreement for the C_3H_7OH (m/z 60) PIE curve by combining the PIE curves of 1 and 2-propanol. The data appeared at lower energy than either alcohol isomer indicating a possible mass contamination from another source. At higher energy the upward curvature strongly suggested the presence of at least 1-propanol. There is no literature data for C_3H_7OOH, but the PIE resembles that of CH_3OOH and C_2H_5OOH (first I.E. 9.87 and 9.65 eV, respectively)[21], and with an appearance energy of ~ 9.6 eV it followed the trend of decreasing appearance energy with larger alkyl group.

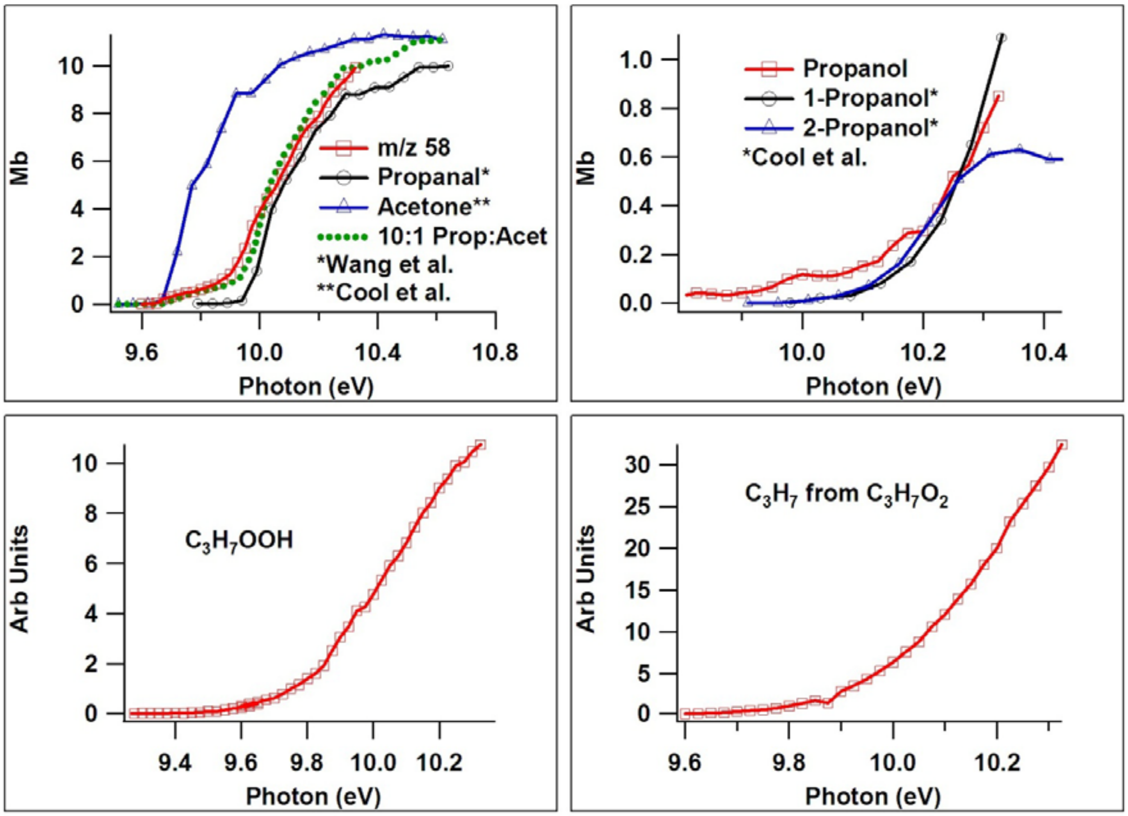

Figure 3-21. PIE of major products and reactants from $C_3H_7O_2$ self reaction using OxCl precursor chemistry.

There were additional masses of interest using this chemistry, some similar to those seen in Run 1A of the $C_2H_5O_2$ work. There was a significant product mass at m/z 44, and from the time trace and PIE curve shown in **Figure 3-22** it appeared that it was largely acetaldehyde. A contribution from dissociative ionization of 2-propanol could not be ruled out, and it was not clear why the appearance energy appeared shifted to lower energy. Also in **Figure 3-22** CH_3O_2 was clearly observed and so was a product at m/z 120. The mass calibration at as large a mass as m/z 120 may have not been accurate, and this product may be the hemi-acetal formed from the reaction of propanal with 1-propanol at m/z 118.

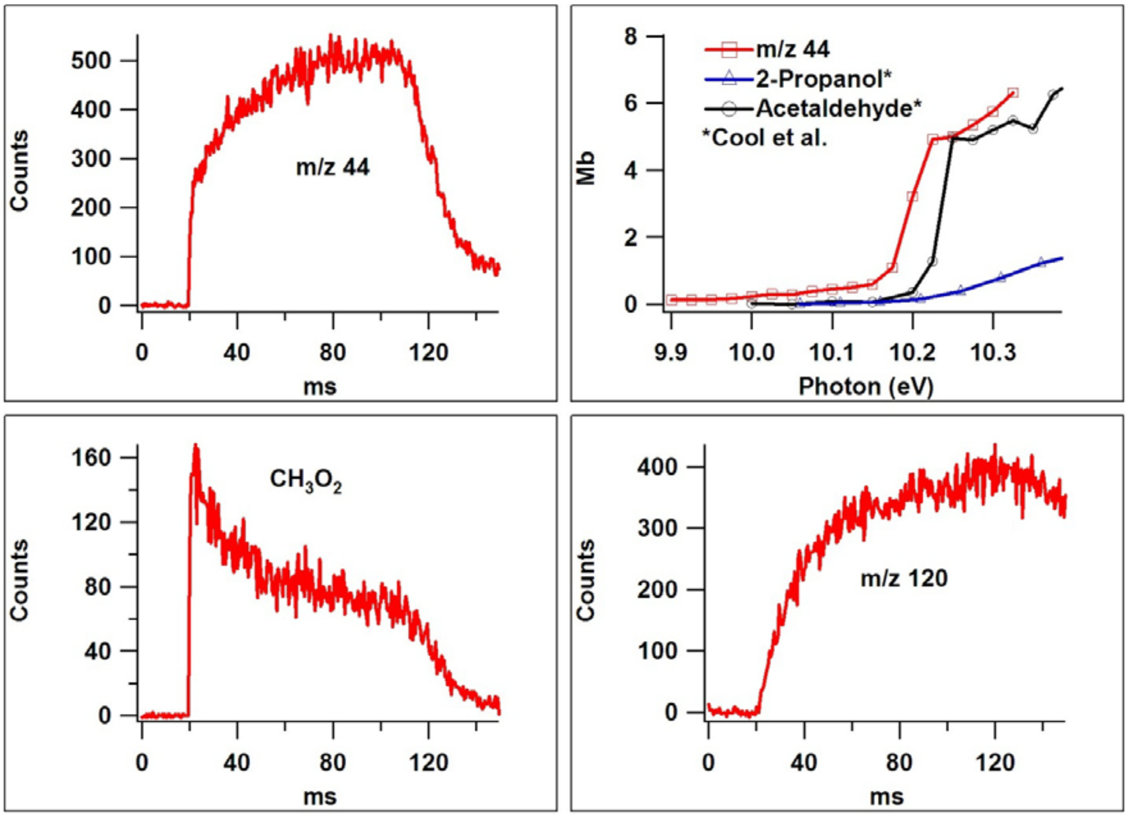

Figure 3-22. Other masses of interest from the propyl peroxy reaction using OxCl precursor chemistry.

3.3.3.1.b Measurement of α

The inability to confidently determine the species asignments at the expected product masses made it impossible to determine α. A more definitive PIE measurement would allow determination of the amount of each product, as would a combination of single point runs at energies that would select for one or other isomer.

3.3.3.2 Run 1B (DPK chemistry)

3.3.3.2.a Observed products

The DPK precursor chemistry was used to avoid the isomer problems of the OxCl precursor chemistry. It was surprising when all the major products were not observed. There was no evidence of C_3H_7OH at m/z 60 as shown in **Figure 3-23**. There was also an interesting correlation between the rapid rise in C_2H_5CHO and the rapid decline in C_3H_7 both of which qualitatively appear to occur faster than the $C_3H_7O_2$ self reaction.

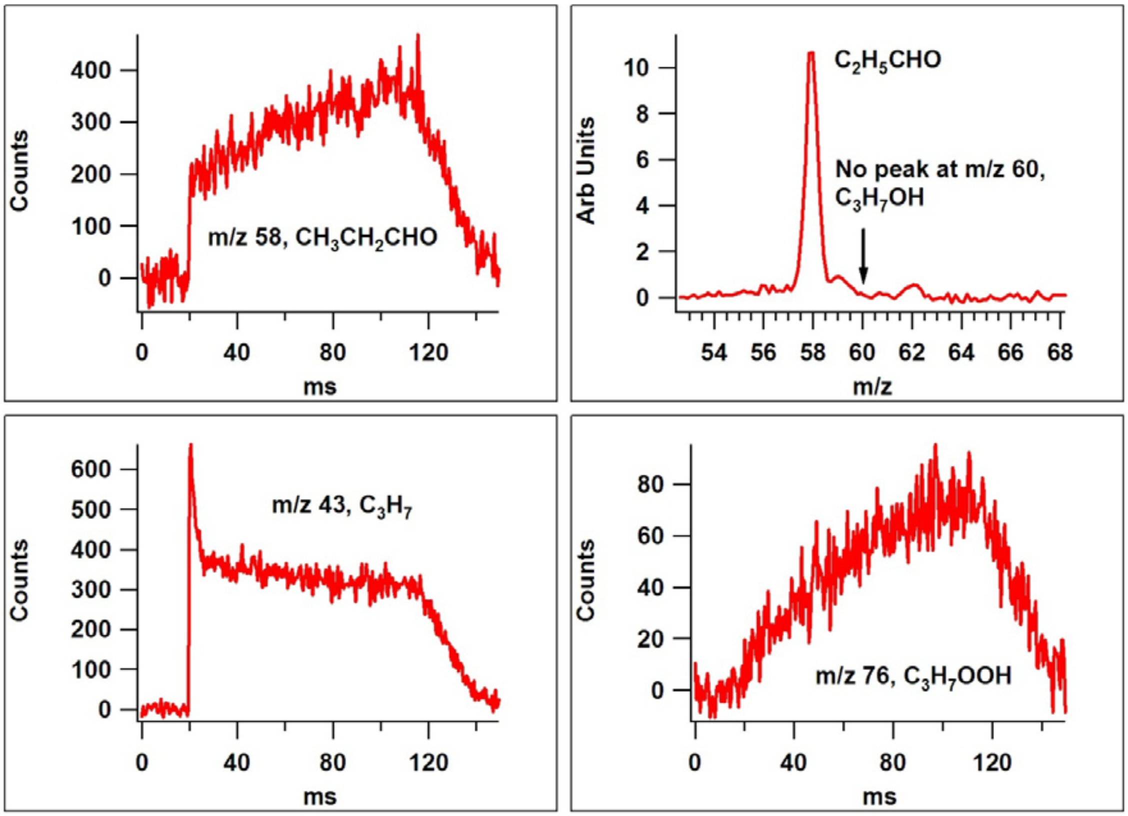

Figure 3-23. Major products and reactants using the DPK chemistry for propyl peroxy.

The PIE curves for these products shown in **Figure 3-24** also left some uncertainty as to their exact assignment. C_2H_5CHO still had the early appearance energy that it had in the OxCl chemistry, making it appear that acetone was contributing as well. The inclusion of acetone still did not resolve the mismatch at higher energies between the PIE curves, suggesting some unknown chemistry was occuring. The C_3H_7OOH PIE curve was similar in shape to the PIE taken with the OxCl chemistry, but had a slightly earlier appearance energy. Poor mass resolution for the PIE was a problem at some m/z as shown for C_3H_7, but the shape of C_3H_7 was similar to that from the OxCl chemistry.

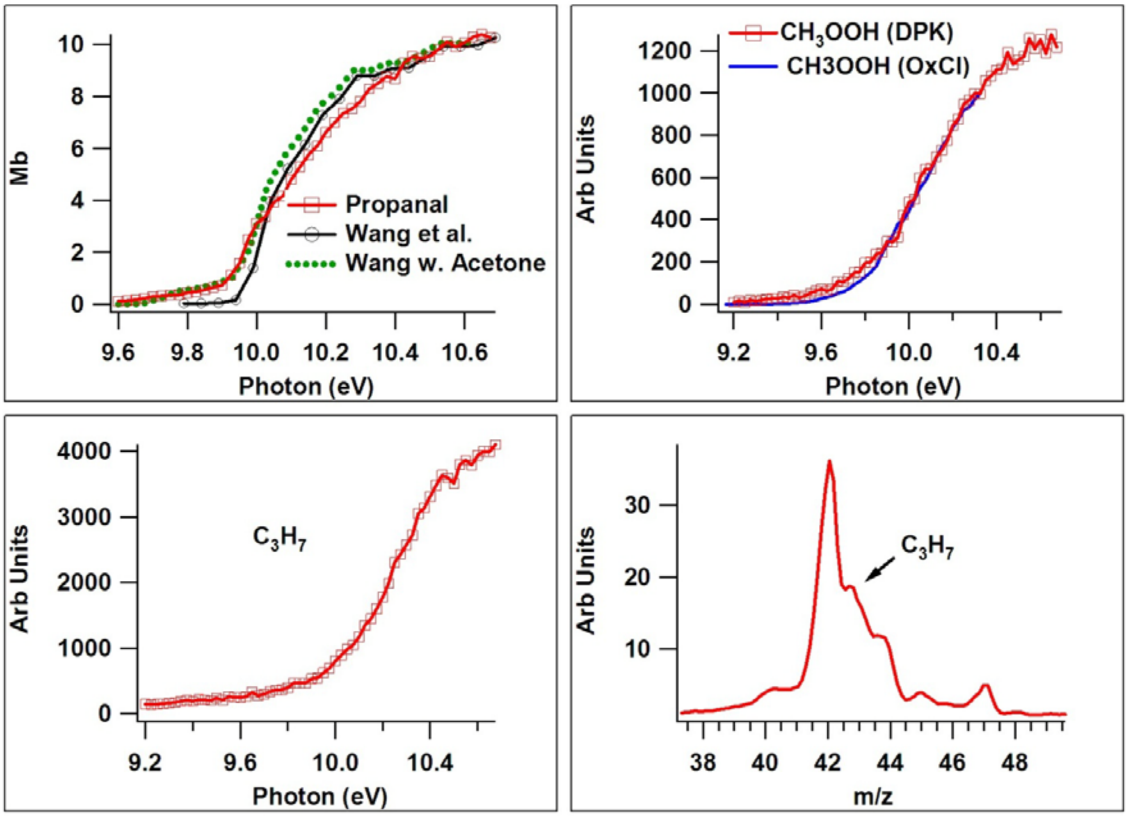

Figure 3-24. PIE identification using the DPK precursor chemistry for $C_3H_7O_2$

Larger molecular weight products were not observable because of the need to avoid signal saturation due to the DPK precursor similar to the acetone and DEK chemistry.

3.3.3.2.b Measurement of α

Without a confident determination of the major products it was not possible to measure α. Assuming that C_2H_5CHO was detected at m/z 58 and that no C_3H_7OH was detected, would imply an $\alpha = 1$. Further experiments are needed before this can be reliably stated given the unknown masses observed.

3.4 Discussion

3.4.1 $C_2H_5O_2$ self reaction

In this work α for the $C_2H_5O_2$ self reaction was measured during Run 1A and Run 2. The measured value for each run was different. Run 2 was the stronger set of data and was the basis of the overall results. Run 1A had complications resulting from secondary chemistry of the products on the walls of the flow tube. The value of α measured during Run 1A was in agreement with end product studies in the literature so the secondary chemistry that was observed in Run 1A may explain some of the other literature results as well.

3.4.1.1 Run 1A compared with Run 2: Observed Products

The first clear difference between Run 1A and 2 was the pump out portion of the individual mass time traces. By comparing **Figure 3-2** and **Figure 3-11** it is clear that the incomplete pump out of C_2H_5OH and C_2H_5OOH in Run 1A was not a problem in Run 2. In this system wall interactions were unavoidable, and sometimes a clean tube required a certain amount of use before the walls became passivated. Prior to Run 1A a clean tube was inserted, which may have not had enough preliminary runs to passivate it. This could have led to preferential sticking of the hydroxyl and hydroperoxyl species. In one kinetics model fit a wall equilibrium was introduced for C_2H_5OH and α was fixed at 0.30 based on the data from Run 2. K_{eq} values ranged from 0.9 – 1.1 with forward and reverse rates ranging over 300 – 400 s^{-1}. The rate constants needed appear to be a little fast to reasonably explain the data. However the JPL work has found diffusion rates for $C_2H_5O_2$ of 5 – 10 s^{-1} at 50 Torr.[28] Directly proportional diffusion rates would be 68 – 125 s^{-1} at 4 Torr. Given the uncertainty in the absolute rate constants from the data already discussed it is possible that wall loss could have played a role in the α measured.

Wall chemistry also may have played a role in the other noticeable difference between Run 1A and Run 2, the extra mass peaks. Comparing the 1-D mass spectrums in **Figure 3-4** and **Figure 3-12** the data from Run 1A had much larger relative mass peaks at m/z 45 and 47 than in Run 2. **Table 3-1** shows all the additional peaks discussed during the results section of Run 1A that did not appear in Run 2. The peroxy hemiacetal chemistry assigned in Run 1A is supported by the fact that when no m/z 106 peak was seen in Run 2 the m/z 45 dissociation product was also greatly reduced. Some small amount of secondary chemistry was still occurring in Run 2, as evidenced by the occasional detection at m/z 90, but it appeared to play a much smaller role in the overall chemistry. Although much smaller, the peak at m/z 45 in Run 2 was still larger than would be expected from isotopic abundance alone. One other possible source was a small amount of dissociative ionization from C_2H_5OH. Dissociative ionization is not reported to occur until 10.8 eV,[15] but reaction (3.1) is exothermic by 350 kJ/mol so it is possible that some excited C_2H_5OH was cracking during ionization at lower than expected energies. A last possibility was dissociative ionization of C_2H_5OOH, but experimental and theoretical work by Li et al. shows that the first electron removed is a non-bonding electron on the O atom leading to a tighter O-O bond, not dissociation.[21]

The m/z 47 peak was unexplained in both Run 1A and Run 2. As with m/z 45 it was partially due to an isotopic peak of ethanol, but was also larger than expected. The time trace appears almost as a step function indicating a stable product from the formation chemistry. The time trace taken together with the odd mass number means that it was likely to have come from a dissociative ionization process, because a radical would have undergone further reaction.

At higher mass, one complication with a secondary chemistry explanation of the m/z 106 time trace was the speed with which the product grew in. **Figure 3-5** shows the time dependence of m/z 106 to be as fast as that of the primary products. If secondary surface chemistry was responsible a slower appearance would have been expected similar to what was observed at m/z 90. One explanation is that some wall absorption of the ethanol and ethyl hydroperoxide remains between shots helping to jump start the chemistry after the next pulse.

The formation chemistry of the $C_2H_5O_2$ was not affected by the use of 193 nm or 248 nm excimer light for the photolysis of OxCl. No difference was seen between the mass spectrum of the 4 Torr 193 nm and 248 nm photolysis data sets in Run 2. This suggests that reactions of the $ClCO^*$ fragment before it falls apart were not important in the 248 nm photolysis, and that the unexplained mass peaks did not involve $ClCO^*$ chemistry.

Overall the larger mass interferences in Run 1A can be explained by further reactions of the products from the $C_2H_5O_2$ self reaction. This additional chemistry combined with the observed wall interactions skewed the measured amounts of the stable products.

3.4.1.2 Run 1A compared to Run 2: Measurement of α and other R

In both runs the absolute kinetics determined rate constants which could be as much as 2 – 4 times that of the literature values. This results from the difficult nature of determining the absolute calibration factors for the experiment. As discussed in the Results and Analysis section, in Run 1A the monochromator slits were accidentally adjusted during the calibration run leading to uncertainty in the total photon count. The general quality of the fits in Run 1A was good, as can be seen in **Figure 3-2**, whereas the quality of the fit was not as good for all the time traces simultaneously in Run 2. **Figure 3-11** shows a number of the fits, each of which were able to represent some of the time traces. The C_2H_5OH and C_2H_5OOH time traces appeared more in sync, but the CH_3CHO had a rapid rise not seen in the other masses. An early source of CH_3CHO is not known. Reactions (3.22) and (3.23) have been looked for but are negligible for room temperature experiments.[25,29]

$$\mathrm{C_2H_5} + \mathrm{O_2} \longrightarrow c - \mathrm{C_2H_4O} + \mathrm{OH} \tag{3.22}$$

$$\mathrm{C_2H_5} + \mathrm{O_2} \longrightarrow \mathrm{CH_3CHO} + \mathrm{OH} \tag{3.23}$$

The imperfect time trace agreement between all the stable products in Run 2 was the only outstanding issue with those data sets. For both runs the relative nature of the α measurement meant that it was not affected by the uncertainty in the calibration factor and the values from the kinetics fits were in good agreement with the values obtained from *R*. This agreement helped validate the steady state approximation used in the derivation of *R*.

The other ratios $R_{A/EH}$ and $R_{E/EH}$ showed different behavior in Run 1A and Run 2, potentially shedding further light on why the two runs differ. The most striking feature of a comparison between **Figure 3-8** and **Figure 3-15** is the behavior of $R_{E/EH}$ for Run 1A during the pump out. This displays again the different nature of the pump out process for the different stable products. In Run 2 C_2H_5OOH was pumping out more slowly than the other products, but it was not as large a difference as seen in Run 1A.

The value of α measured in Run 2 was the best determination. Problems with additional chemistry probably threw off the value of α in Run 1A. Absolute kinetics were not reliable from either run, so more attention needs to be paid to the calibration runs in the future to determine absolute rate constants.

3.4.1.3 Photoionization cross section of C_2H_5OOH

The photoionization cross section of C_2H_5OOH was measured relative to the values of CH_3CHO, C_2H_5OH, and C_2H_4. Each of these species has known cross sections given in the experimental section. All production of C_2H_5OOH can be quantitatively linked to the concentrations of these three species if you assume that C_2H_5OOH was only produced by reaction (3.5). This means finding all the sources of HO_2 which was produced initially in equal amounts with C_2H_4, and also by reaction of C_2H_5O with O_2. Therefore C_2H_4 determines the initial amount, and the comparison of CH_3CHO with C_2H_5OH determines the amount produced from C_2H_5O, so all sources are covered. One downside is that this value is not entirely independent of the kinetics, which would have been desirable given their inaccuracy, because it does depend on the overall rate of production C_2H_5OOH from the kinetics model. The reported value of 2.57 Mb at 10.7 eV was determined from Run 2 data sets where the chemistry was better understood. The error in this measurement was difficult to determine, but given the uncertainty in the kinetics fits a reasonable estimate is that it is good to within a factor of 2.

3.4.2 CH_3O_2 self reaction

Overall the CH_3O_2 data was very promising, but there were not enough data sets to make a definitive measurement of α. The mass resolution and species assignments were mostly straightforward. An alternative chemistry for producing CH_3O_2 would be useful to allow investigation of larger product masses, but there were no significant product masses at lower weight which appeared as though they might come from a larger parent. The only complication in the data was the transient peak at m/z 32 on top of the CH_3OH signal. If this is persistent, coming perhaps from excited O_2, then it will cause some problems with the data, but it appears that it does not last long in time so it is safe to treat the data later on as free from contamination. More data is necessary to answer these questions, but the approach appears very promising.

3.4.3 $C_3H_7O_2$ self reaction

Neither the OxCl or DPK chemistry provided a clear story of the $C_3H_7O_2$ self reaction. As was expected the non-isomer-specific OxCl chemistry led to challenges with identification of the products. What was not expected was that the 1-$C_3H_7O_2$ isomer-specific DPK chemistry products also did not exactly match the expected PIE curves. In each case it was not exactly clear why the PIE curves could not be matched well. In principle a quantitative fit to the PIE curves at one mass using reference PIEs for the two isomers could determine the contribution of each isomer and allow for determination of α. This assumes they have a nearly identical time dependence, i.e., that the two RO_2 isomers have similar self reaction rate constants. Therefore this data did not make it possible to determine whether a better data set or better chemistry approach is needed. There did appear to be specific difficulties that were common to each initiation chemistry regardless of RO_2, but these will be discussed further below. Overall an approach that separates the isomers by initiation chemistry is more appealing, but it should not be required if other factors are more of a problem.

3.4.4 Ketone initiation chemistry

Acetone, DEK, and DPK were all used as photolytic precursors for their corresponding RO_2 radicals through reactions (3.14), (3.13), and (3.17). The major downside of this production method was the inability to look for the ROOR or other high molecular weight products due to the necessity of avoiding signal saturation from the parent ketone by moving large masses off the detector. This problem aside, the ketone chemistry was expected to be a clean source of alkyl radicals for production of RO_2 by reaction (3.6). The acetone chemistry appeared to work this way, and only an insufficient number of data sets taken prevented a definitive measurement of α from being made. The DEK and DPK chemistries were not as straightforward . This was disappointing especially for the DPK case where the corresponding OxCl chemistry led to multiple isomers. For both DEK and DPK strong signals were obsesrved at the expected aldehyde mass (m/z 44 or m/z 58), but not much product was observed for the corrseponding alcohol product (m/z 46 or m/z 60) as can be seen by comparing **Figure 3-10** and **Figure 3-23**. Another similarity can be seen by looking at the time trace of C_2H_5 and C_3H_7 in **Figure 3-9** and **Figure 3-23**. In both cases there was a fast initial drop in radical followed by a slower reaction trace more indicative of the RO_2 self reaction chemistry. It is possible that some of the initial HO_2 created reacts with still unreacted R.

$$\mathrm{R} + \mathrm{HO_2} \longrightarrow \mathrm{R'CHO} + \mathrm{H_2O} \tag{3.24}$$

This type of reaction has mainly been investigated for R = CH_3 and has been looked at predominantly at higher temperatures for combustion chemistry purposes.[30,31] There has been one experimental study for R = C_2H_5, but it found a relatively slow bimolecular rate constant of $k_{1.24} = 3.1 \times 10^{-13}$ cm^3 molecules^{-1} s^{-1} at room temperature.[32] Large O_2 concentrations mean that reactions (3.6) and (3.7) will be much faster, especially as the size of R increases.[33] These difficult to explain time traces, combined with the skewed product distribution, suggests that except for acetone, the ketone chemistry may not be a good source of alkyl radicals for product analysis of the RO_2 self reaction.

3.4.5 Oxalyl chloride initiation chemistry

There were also similarities among the OxCl chemistry data sets across RO_2. The high radical concentration OxCl chemistry for $C_2H_5O_2$ and $C_3H_7O_2$ both had problems with pump out of the alcohol and hydroperoxide (**Figure 3-2** and **Figure 3-20**). It is not clear if the problem was common to both chemistries because they were done right after each other in time, or whether it was related to the high radical concentrations present. These runs also had evidence of high molecular weight products that appeared to be from wall reactions. In Run 2 of the $C_2H_5O_2$ self reaction the OxCl concentration was reduced an order of magnitude and the reaction chemistry occurred cleanly without any pump out or high molecular weight product issues. Radical concentration was probably an important factor, but so was the overall chemistry because the ketone chemistry just discussed was also of lower radical concentration, but was not as reliable.

3.4.6 Comparison with literature

3.4.6.1 $C_2H_5O_2$

The majority of previous studies on α of the $C_2H_5O_2$ self reaction have been done by end product analysis on the time scale of minutes after the reaction. Chapter 2 described the only previous study to determine α on the time scale of the reaction by detecting the secondary HO_2 produced from the reaction sequence of (3.2) and (3.4). The value of α determined by this method was half the value determined previously by the end product studies. This experiment was able to perform a similar end product analysis as the initial studies, but on the same time scale as the reaction to prevent any unknown secondary chemistry from distorting the observed ratios.

There have been six previous studies that measured α for the $C_2H_5O_2$ self reaction. Two of these, the Kaiser et al.[34] work and the Anastasi et al.[35] were superseded by new work from the same group and never published in the peer reviewed literature, and will not be discussed further. The other studies are all plotted in **Figure 3-25**.[28,36-38]

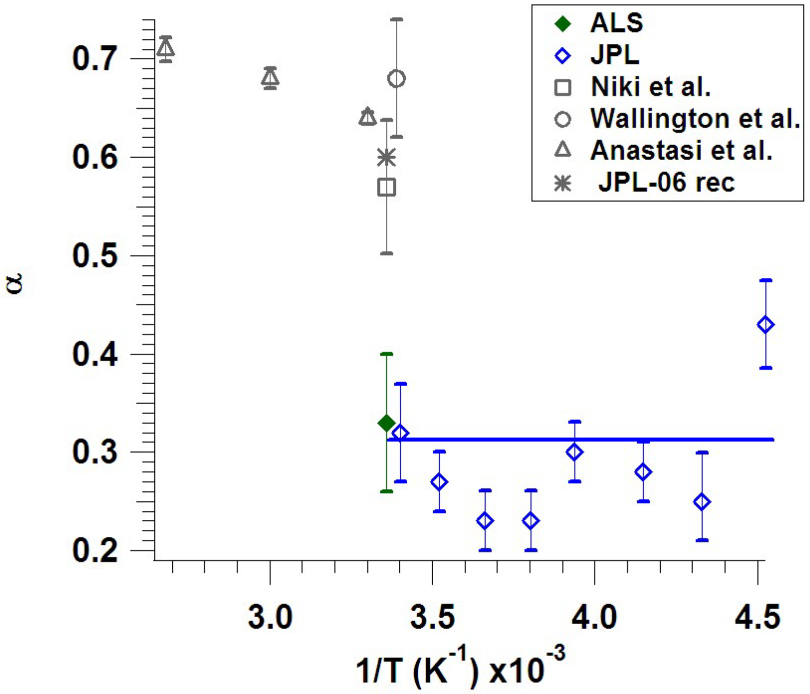

Figure 3-25. Comparison of α measurements. JPL and ALS work both made measurements on the time scale of the reaction.

Chapter 2 summarized the differences between that work and the others.This work provided a bridge between all of the previous work because it was done on the same time scale of the reaction similar to Chapter 2, but detected all of the stable products similar to the end product studies. The Run 1A data measured an α that was in agreement with the older end product studies, but the data plotted in **Figure 3-25** is from Run 2 and is in best agreement with the Chapter 2 measurement (Labeled as “JPL”). Run 2 was settled on as the better data set because of secondary chemistry complications in Run 1A. If the comparison of Run 1A and Run 2 serves as a model for what might lead to the difference between the Run 2 result and the other end product studies, then additional secondary chemistry could be the reason for the higher values of α measured by the end product studies. As an example, the flash photolysis experiment from the Chapter 2 work was immune to surface chemistry so it would not have been affected by hemi-acetal reactions (3.18) and (3.19), but The FTIR studies of Niki et al. and Wallington et al. would have been prone to these interfering reactions.[37,38] The different values from Run 1A and Run 2 show that under certain conditions this work was also susceptible to wall chemistry, but suitable conditions could be achieved where the interference was negligible.

One further type of wall chemistry not previously considered is the conversion of hydroperoxides to aldehydes through the dehydration shown in reaction (3.25). Evidence for this has been found both in the original synthetic studies on hydroperoxides and in more recent work investigating the raman spectroscopy of the hydroperoxides.[39,40]

$$\mathrm{C_2H_5OOH} \longrightarrow \mathrm{CH_3CHO} + \mathrm{H_2O} \tag{3.25}$$

Production of water would have been a signature of this occuring, but the IP of water was above the energy at which we took data so it could not be identified. Still, the simplest and most plausible explanation for the differences observed are that higher radical concentrations of the literature and Run 1A work allowed for wall chemistry that interfered with the main products.

3.4.6.2 CH_3O_2

A full comparison with the literature for the CH_3O_2 self reaction is premature given the single measurement made with this work. Still that measurement ($\alpha = 0.53$) is outside the range of previous measurements and the recommended value, $\alpha = 0.28 – 0.43$, 0.37 recommended.[1] The $C_2H_5O_2$ value was also outside the range of previous measurements, but it was lower rather than higher. If this value were to hold up it might indicate a completely different trend with alkyl group than anticipated. As discussed last chapter, the uncertainty in the mechanism of the RO_2 self reaction raised by recent theoretical work makes it difficult to predict what the trend with R group should be.[41] Further experimental work looking at the nascent products may be able to guide the theory as to what pathways are important.

3.4.6.3 $C_3H_7O_2$

No measurement of α was possible with the preliminary data recorded here, but there are only two previous determinations for the self reaction of 2-$C_3H_7O_2$.[2,3] Both these studies are end product studies using GC or GC/MS, so further work would be very useful. If a new trend in α with RO_2 was expected, confirmation from work on a larger RO_2 such as $C_3H_7O_2$ would be essential.

3.5 Conclusion

In this work the RO_2 self reactions for R = CH_3, C_2H_5, and C_3H_7 have been investigated using a time resolved photoionization mass spectrometer to allow for real time detection of the reaction products. Products and reactants of the reactions were identified by both their time traces and their PIE curves. The radical product channel branching fraction, α, was measured to be 0.33 ± 0.08 for the $C_2H_5O_2$ self reaction. This value was in agreement with the work in Chapter 2 that also made measurements of α on the timescale of the reaction, but disagrees with previous end product studies. Preliminary data for the CH_3O_2 and $C_3H_7O_2$ self reactions were also obtained. More data is needed to make a definitive determination of α for these reactions, but a good understanding of complications from different precursor chemistries should make further measurements simpler.

3.6 References

(1) Tyndall, G. S.; Cox, R. A.; Granier, C.; Lesclaux, R.; Moortgat, G. K.; Pilling, M. J.; Ravishankara, A. R.; Wallington, T. J. *Journal of Geophysical Research-Atmospheres* **2001**, *106*, 12157.

(2) Cowley, L. T.; Waddington, D. J.; Woolley, A. *Journal of the Chemical Society-Faraday Transactions I* **1982**, *78*, 2535.

(3) Kirsch, L. J.; Parkes, D. A.; Waddington, D. J.; Woolley, A. *Journal of the Chemical Society-Faraday Transactions I* **1979**, *75*, 2678.

(4) Lightfoot, P. D.; Lesclaux, R.; Veyret, B. *Journal of Physical Chemistry* **1990**, *94*, 700.

(5) Osborn, D. L.; Zou, P.; Johnsen, H.; Hayden, C. C.; Taatjes, C. A.; Knyazev, V. D.; North, S. W.; Peterka, D. S.; Ahmed, M.; Leone, S. R. *Review of Scientific Instruments* **2008**, *79*.

(6) Wu, C. Y.; Lee, Y. P.; Ogilvie, J. F.; Wang, N. S. *Journal of Physical Chemistry A* **2003**, *107*, 2389.

(7) Hall, G. E.; Metzler, H. W.; Muckerman, J. T.; Preses, J. M.; Weston, R. E. *Journal of Chemical Physics* **1995**, *102*, 6660.

(8) Reid, J. P.; Marcy, T. P.; Kuehn, S.; Leone, S. R. *Journal of Chemical Physics* **2000**, *113*, 4572.

(9) Weir, D. S. *Journal of the American Chemical Society* **1961**, *83*, 2629.

(10) NIST Chemistry WebBook, http://webbook.nist.gov/chemistry/, 2009.

(11) Baklanov, A. V.; Krasnoperov, L. N. *Journal of Physical Chemistry A* **2001**, *105*, 97.

(12) Lightfoot, P. D.; Kirwan, S. P.; Pilling, M. J. *Journal of Physical Chemistry* **1988**, *92*, 4938.

(13) Choi, N.; Pilling, M. J.; Seakins, P. W.; Wang, L. *Physical Chemistry Chemical Physics* **2006**, *8*, 2172.

(14) Knyazev, V. D.; Slagle, I. R. *Journal of Physical Chemistry A* **2001**, *105*, 6490.

(15) Cool, T. A.; Wang, J.; Nakajima, K.; Taatjes, C. A.; McIlroy, A. *International Journal of Mass Spectrometry* **2005**, *247*, 18.

(16) Cooper, G.; Anderson, J. E.; Brion, C. E. *Chemical Physics* **1996**, *209*, 61.

(17) Cool, T. A.; Nakajima, K.; Mostefaoui, T. A.; Qi, F.; McIlroy, A.; Westmoreland, P. R.; Law, M. E.; Poisson, L.; Peterka, D. S.; Ahmed, M. *Journal of Chemical Physics* **2003**, *119*, 8356.

(18) Wang, J.; Yang, B.; Cool, T. A.; Hansen, N.; Kasper, T. *International Journal of Mass Spectrometry* **2008**, *269*, 210.

(19) Hsu, W. L.; Tung, D. M. *Review of Scientific Instruments* **1992**, *63*, 4138.

(20) FACSIMILE; 4.0.36 ed.; MCPA Software Ltd. 2002.

(21) Li, Y. M.; Sun, Q.; Li, H. Y.; Ge, M. F.; Wang, D. X. *Chinese Journal of Chemistry* **2005**, *23*, 993.

(22) Tobias, H. J.; Docherty, K. S.; Beving, D. E.; Ziemann, P. J. *Environmental Science & Technology* **2000**, *34*, 2116.

(23) Leach, S.; Schwell, M.; Jochims, H. W.; Baumgartel, H. *Chemical Physics* **2006**, *321*, 171.

(24) Wood, K. V.; Taylor, J. W. *International Journal of Mass Spectrometry and Ion Processes* **1979**, *30*, 307.

(25) Clifford, E. P.; Farrell, J. T.; DeSain, J. D.; Taatjes, C. A. *Journal of Physical Chemistry A* **2000**, *104*, 11549.

(26) Wagner, A. F.; Slagle, I. R.; Sarzynski, D.; Gutman, D. *Journal of Physical Chemistry* **1990**, *94*, 1853.

(27) Meloni, G.; Zou, P.; Klippenstein, S. J.; Ahmed, M.; Leone, S. R.; Taatjes, C. A.; Osborn, D. L. *Journal of the American Chemical Society* **2006**, *128*, 13559.

(28) Noell, A. C. A., L.N.; Robichaud, D. J.; Okumura, M.; Sander, S.P. **Manuscript in preparation**.

(29) DeSain, J. D.; Klippenstein, S. J.; Miller, J. A.; Taatjes, C. A. *Journal of Physical Chemistry A* **2003**, *107*, 4415.

(30) Jasper, A. W.; Klippenstein, S. J.; Harding, L. B. *Proceedings of the Combustion Institute* **2009**, *32*, 279.

(31) Zhu, R. S.; Lin, M. C. *Journal of Physical Chemistry A* **2001**, *105*, 6243.

(32) Ludwig, W.; Brandt, B.; Friedrichs, G.; Temps, F. *Journal of Physical Chemistry A* **2006**, *110*, 3330.

(33) Ruiz, R. P.; Bayes, K. D. *Journal of Physical Chemistry* **1984**, *88*, 2592.

(34) Kaiser, E. W.; Rimai, L.; Wallington, T. J. *Journal of Physical Chemistry* **1989**, *93*, 4094.

(35) Anastasi, C. B., M.J.; Smith, D.B.; and Waddington, D.J. Joint Meeting of the French and Italian Sections of the Combustion Institute, June 1987, Amalfi.

(36) Anastasi, C.; Waddington, D. J.; Woolley, A. *Journal of the Chemical Society-Faraday Transactions I* **1983**, *79*, 505.

(37) Niki, H.; Maker, P. D.; Savage, C. M.; Breitenbach, L. P. *Journal of Physical Chemistry* **1982**, *86*, 3825.

(38) Wallington, T. J.; Gierczak, C. A.; Ball, J. C.; Japar, S. M. *International Journal of Chemical Kinetics* **1989**, *21*, 1077.

(39) Jacob, P.; Wehling, B.; Hill, W.; Klockow, D. *Applied Spectroscopy* **1997**, *51*, 74.

(40) Rieche, A.; Hitz, F. *Berichte Der Deutschen Chemischen Gesellschaft* **1929**, *62*, 2458.

(41) Ghigo, G.; Maranzana, A.; Tonachini, G. *Journal of Chemical Physics* **2003**, *118*, 10575.

4 Photoinduced nucleation of low temperature hydroperoxy radical chemistry

4.1 Introduction

New particle formation events are well known in the atmosphere, occurring on ~ 90% of days in the coastal U.K. as one example.[1] However the contribution these nucleation events make to the total atmospheric aerosol, and all of the associated climate and air pollution effects, still remains unclear.[2,3] New particle formation has been found to occur nearly everywhere in the atmosphere, and a variety of mechanisms including binary, ternary, and ion-induced heteromolecular homogenous nucleation have been proposed.[4] The large amount of sulfate in aerosols suggests the importance of ternary sulfuric acid-water-ammonia heteromolecular homogenous nucleation,[5,6] but the large organic fractions observed in aerosol are not thought to result from homogenous nucleation except in particular circumstances.[7] In order to better understand the mechanism of homogenous nucleation, both theoretical and experimental investigations have begun on the nanoscale ultrafine clusters which are the precursor to these particles.[8,9]

It is clear that the importance of homogenous nucleation will be regime dependent as models predict orders of magnitude differences in new particle formation rates based on chemical sources and local meterology.[5] The coasts appear to be one area that are highly susceptible to influence from homogeneous nucleation. A recent summary of marine aerosol by O’Dowd and de Leeuw focuses on two possible mechanisms for nucleation: Ternary nucleation of sulfuric acid-water-ammonia mixtures and iodine oxide radical reactions.[10] The first mechanism is one of the well established nucleation mechanisms mentioned previously. The second is interesting because it proposes radical chemistry, i.e., photoinduced chemistry, as part of the nucleation mechanism. A number of observational studies have noted the importance of sunlight for nucleation events to occur, but the focus has been on the radical chemistry converting sulfur species to sulfuric acid,[5] rather than a direct role of the radical in nucleation.

While the details of nucleation models still differ, an important step from the molecular point of view is the formation of a critical cluster. The critical cluster size is reached when a fluctuating collection of molecules begins adding more molecules than it loses and experiences runaway growth leading to a particle. In the atmosphere the existence of radical molecule complexes might help create critical clusters for nucleation. Theoretical work investigated how the complex of the hydroperoxy radical (HO_2) with water (H_2O) might affect aerosol and water droplets, but experimental studies are lacking.[11,12] Work in this lab has looked at an analogous hydrogen bonding complex between HO_2 and methanol (CH_3OH), motivated by the fact that CH_3OH is a common precursor for HO_2 in flash photolysis systems.[13,14]

$$\mathrm{Cl_2} \xrightarrow{hv\ 308\ nm} \mathrm{2Cl} \tag{4.1}$$

$$\mathrm{Cl + CH_3OH \longrightarrow CH_2OH + HCl} \tag{4.2}$$

$$\mathrm{CH_2OH + O_2 \longrightarrow HO_2 + HCHO} \tag{4.3}$$

$$\mathrm{HO_2 + HO_2 \xrightarrow{M} H_2O_2 + O_2} \tag{4.4}$$

$$\mathrm{HO_2 + CH_3OH \rightleftharpoons HO_2{\bullet}CH_3OH} \tag{4.5}$$

$$\mathrm{HO_2 + HO_2{\bullet}CH_3OH \longrightarrow H_2O_2 + O_2 + CH_3OH} \tag{4.6}$$

$$\mathrm{HO_2{\bullet}CH_3OH + CH_3OH \rightleftharpoons HO_2{\bullet}(CH_3OH)_2} \tag{4.7}$$

$$HO_2\bullet(CH_3OH)_n + CH_3OH \rightleftharpoons HO_2\bullet(CH_3OH)_{n+1} \qquad (4.8)$$

Previous experimental work initially focused on reactions (4.4) – (4.6) and the role of the HO_2• CH_3OH complex on the kinetics of the HO_2 self reaction. The possibility of further complexation as depicted in reactions (4.7) and (4.8) was proposed due to non-linear kinetic dependences as well as the observation of large absorptions attributed to nucleation. This work has further probed the observed nucleation of the HO_2• CH_3OH system, and also explored whether other hydrogen bonding partners of HO_2 might nucleate.

4.2 Experimental

The infrared kinetics spectroscopy (IRKS) apparatus was used during these experiments. Briefly, it consisted of a two meter glass flow cell that was jacketed to allow for temperature control. Chemistry in the cell was initiated by flash photolysis with an excimer laser that made one pass down the length of the cell. Two optical probes, one in the UV and one in the NIR, monitored the time behavior of species in the cell. UV light from a deuterium lamp made one pass through the cell co-aligned and counter-propagating with the photolysis beam. A NIR diode made 30 passes through the cell using spherical Herriott mirrors. A full description of the apparatus has been given previously,[15,16] and it will also be discussed further in Chapter 5.

Two significant changes have been made in the experimental procedures and data analysis. First, wavelength modulation of the NIR probe was not used. Direct absorption provided sufficient sensitivity and a more physically meaningful measurement of the total light extinction. Second, a temperature correction was applied to the data. Chapter 5 discusses the measurements which revealed a discrepancy between the measured temperature and the true temperature. Data originally thought to be at temperatures ranging from 221 – 234 K were actually at 210 – 225 K. This difference is important because [CH_3OH] used was constrained by the vapor pressure of CH_3OH at that particular temperature. In order to compare the [CH_3OH] being used at different temperatures we defined the relative humidity of CH_3OH in equation (4.9) ,

$$RH_{CH3OH} = \frac{[\mathrm{CH_3OH}]}{[\mathrm{CH_3OH}]^*} * 100\% \tag{4.9}$$

where $[CH_3OH]^*$ was the vapor pressure of CH_3OH at a particular temperature expressed as a concentration in molecules cm^{-3}. For one or two data sets the temperature offset meant that $RH_{CH3OH} > 100\%$ was used. No difference in the nucleation behavior was observed under these circumstances, but it was suspected that some condensation of CH_3OH on the walls of the flow cell was occurring due to the continued evidence of chemistry and nucleation after the CH_3OH flow had been shut off.

Reagent and bulk flows were all monitored with mass flow controllers. The vapor from liquid reagents was introduced into the flow cell by bubbling nitrogen gas through the reagent as it was held at a fixed temperature. Methanol (V.P. 30 Torr @ 273K), water (V.P. 5.3 Torr at 275 K), and acetone (V.P. 41 Torr @ 263K) were all delivered in this way. Cl_2 (g) was the radical precursor and was also used as a proxy for initial radical concentration ($[HO_2]_0$). Without nucleation present, and at low [CH_3OH] where formation of $HO_2 \bullet CH_3OH$ was negligible, $[HO_2]_0$ could be determined by fitting the self reaction of HO_2. It was a general rule that $[HO_2]_0 \bullet 0.01*[Cl_2]$. This relationship was used when nucleation of high [CH_3OH] made it difficult to directly determine $[HO_2]_0$.

A number of different experiments were conducted to explore the nucleation behavior. The dependence of the nucleation on temperature, [CH_3OH], $[HO_2]_0$, and O_2

was examined. Ethane was also added as a precursor to observe the effect another peroxy radical, i.e., $C_2H_5O_2$, had on the nucleation. H_2O and acetone were also added to see how other hydrogen bonding partners of HO_2 affected the results.

4.3 Results

There was a large extinction of the light from both the UV and NIR probes under the right conditions of temperature, [CH_3OH], and [HO_2]$_0$. The different behavior observed by the two probes provided clues about the size of the particles. Some of the chemical species present, i.e., H_2O_2 and HCl, could be ruled out as important to nucleation by substituting $C_2H_5O_2$ chemistry. Without O_2 much greater nucleation was observed, suggesting a completely different mechanism occurs under those conditions. Nucleation was also observed in the presence of acetone but not with H_2O.

4.3.1 UV absorption

The UV absorption signal for the HO_2 self reaction, at 222 K and $[HO_2]_0 = 1.0 \times 10^{14}$ molecules cm^{-3}, is shown in **Figure 4-1** as a function of [CH_3OH]. The inset shows the standard time window for observing the reaction, and the time trace as the [CH_3OH] was raised to 6.9×10^{15} molecules cm^{-3}. Rather than the signal continuing to return to baseline as the reaction proceeded, a new large absorbance started growing in.

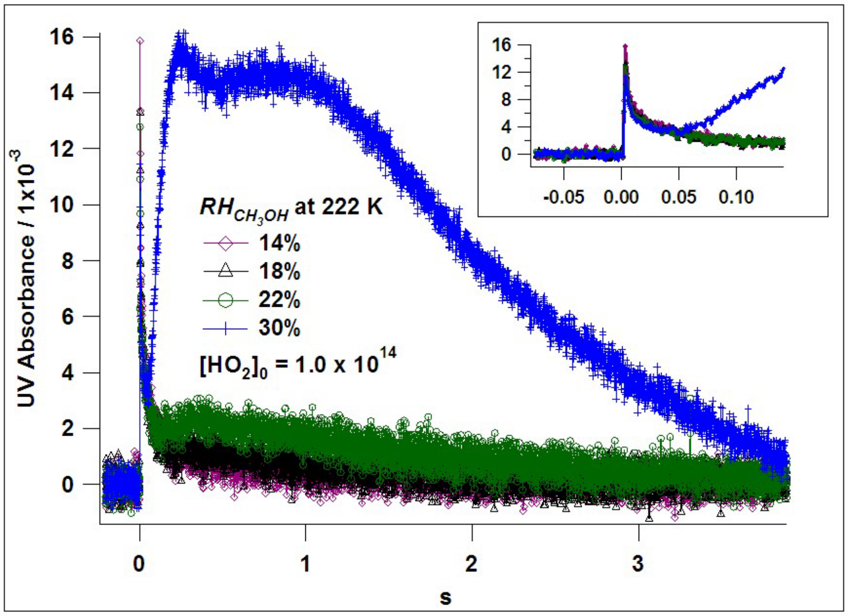

Figure 4-1. UV absorbance from the HO_2 self reaction and the unexpected large absorbance at longer time scales. Inset shows how the same data appeared on the time scale over which the HO_2 self reaction was normally observed.

The rest of the figure shows what the data looked like on a longer time scale; the absorbance continues to grow and remains high for seconds until the pump out of the flow cell starts to remove the absorber. This behavior was also observed at the lower [CH_3OH] of 5.1 x 10^{15} molecule cm^{-3}, only later in time and with less intensity, making it undetectable in the standard time window of the HO_2 self reaction.

4.3.2 Temperature dependence

The large absorption observed in the UV appears to be total extinction due to a phase change, i.e., aerosol formation, than to pure absorption alone. A further study explored whether a temperature change resulted in a sharp or gradual onset of the extinction. A sharp onset would be consistent with a phase change process, while a more gradual dependence might implicate other chemistry. **Figure 4-2** shows the observed extinction in both the UV and the NIR as the temperature of the cell was lowered and then raised from 225 – 216 K and back again at [CH_3OH] = 6.6 x 10^{15} (RH_{CH3OH} varies over 22 – 60% from 225 – 216 K) and $[HO_2]_0 = 1.2 \times 10^{14}$ molecules cm^{-3}. The red 225 K trace showed no sign of nucleation by either probe. In the NIR there was a strange baseline shape at times < 1 s, but it was not related to the aerosol. At 224 K there was an indication of the aerosol in the NIR, but not in the UV. Since the NIR had a much longer pathlength it was more sensitive to the presence of the aerosol. By 223 and 222 K the extinction was very obvious in both probes although the trends were different in the NIR and the UV. Then at 216 K large oscillations appeared that may have been caused by optical resonance between the wavelength and particle size, or by dynamical flow effects. Finally, when the cell was allowed to warm back to 225 K the baselines returned to their original levels, as seen in the blue trace of **Figure 4-2**. There was no evidence of hysteresis or of previously formed particles seeding new particles. This clear temperature dependence and the absence of hysteresis confirmed that aerosol formation was the cause of the light extinction at both wavelengths.

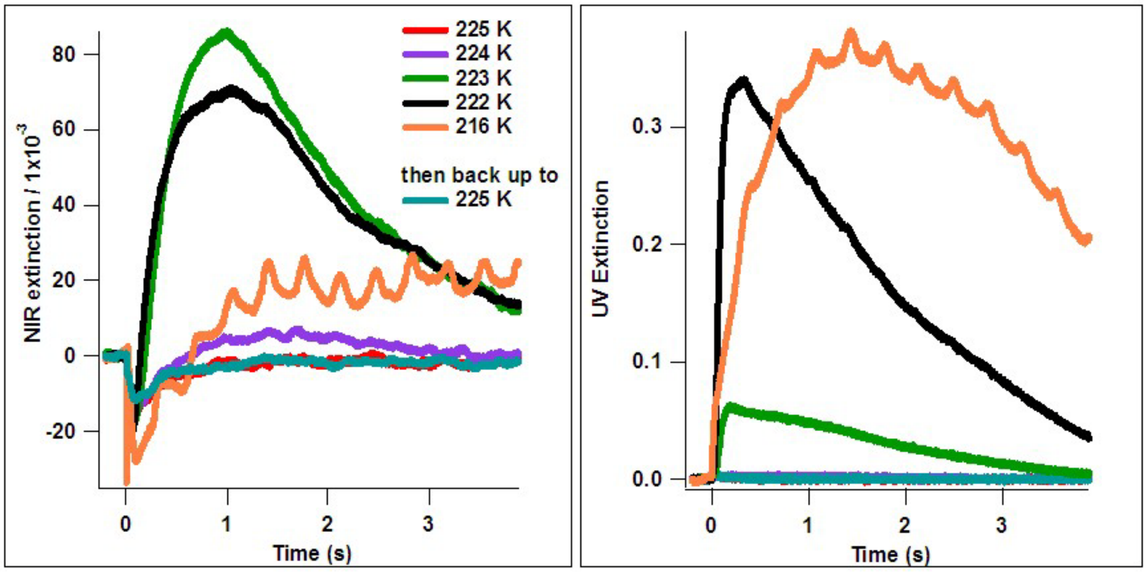

Figure 4-2. Temperature dependence of the extinction in both the NIR and UV. Lowering the temperature one or two degrees led to an immediate appearance of the extinction supporting an aerosol formation hypothesis. No hysteresis was observed in the system as the temperature returned to 225 K.

4.3.3 CH_3OH dependence

Not many species were available to form the bulk of the aerosol; N_2, O_2, Cl_2, and CH_3OH were the only precursors in the system, and only CH_3OH had the ability to condense under the conditions in the cell. **Figure 4-3** shows the UV extinction signal as the [CH_3OH] was increased at a constant temperature of 222 K. A clear dependence on the [CH_3OH] was observed. Additional CH_3OH did not affect the precursor chemistry shown in reactions (4.1) – (4.3) because the reaction of Cl with CH_3OH was already occurring under a large excess of CH_3OH. In order for the additional CH_3OH to influence the observed extinction it had to be contributing to the growth or formation of the aerosol. The strong dependence of the extinction on [CH_3OH] not only indicated that concentration plays a role in determining the number and size of particles, but also that CH_3OH was the major component of the newly formed aerosol.

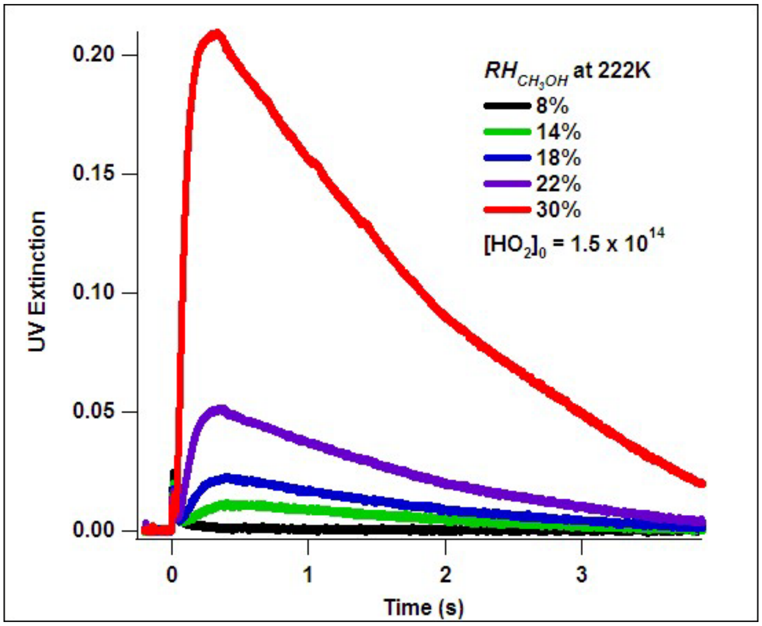

Figure 4-3. Dependence of the UV extinction on CH_3OH concentration. A large increase in extinction was observed for small changes in CH_3OH.

A quantitative interpretation of this data is difficult because both the size and number of particles were changing in time due to growth, agglomeration, and removal from the flow cell by the vacuum pump. Despite this, the large change in extinction observed with only a small increase in [CH_3OH] might provide insight as to the underlying mechanism of the nucleation. **Figure 4-4** shows the dependence of the peak UV extinction on [CH_3OH] at three different initial radical concentrations. Both a power law and 2nd-order polynomial expression fit the data well (the polynomial fit is shown), but no quantitatively consistent dependence was observed under the different radical conditions.

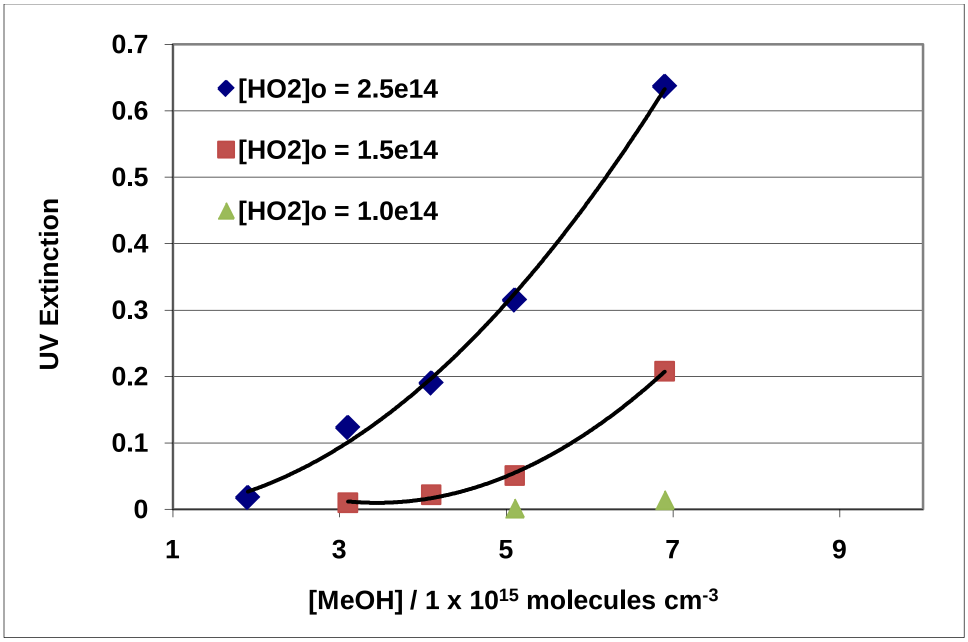

Figure 4-4. Dependence of the peak UV extinction on [CH_3OH] at three different initial radical concentrations

Without further assumptions about either the size distribution or number of particles, no conclusions about the nucleation mechanism were drawn from the quantitative dependence of the extinction on [CH_3OH].

4.3.4 Radical dependence

Nucleation only occurred after the photolysis pulse indicating radical chemistry was a necessary part of initiating particle formation. When starting at low radical concentrations ($[HO_2]_0 < 5 \times 10^{13}$ molecules cm^{-3}), the extinction in both the UV and NIR increased as a function of initial radical concentration, as shown in **Figure 4-5**. The data shown were taken at 224 K and $[CH_3OH] = 3.15 \times 10^{16}$ molecules cm^{-3} (> 100% RH_{CH3OH}), but as mentioned in the experimental section, the nucleation behavior was no different in this case because of the RH_{CH3OH} > 100%. No strange baseline or non-photoinduced nucleation behavior was seen.

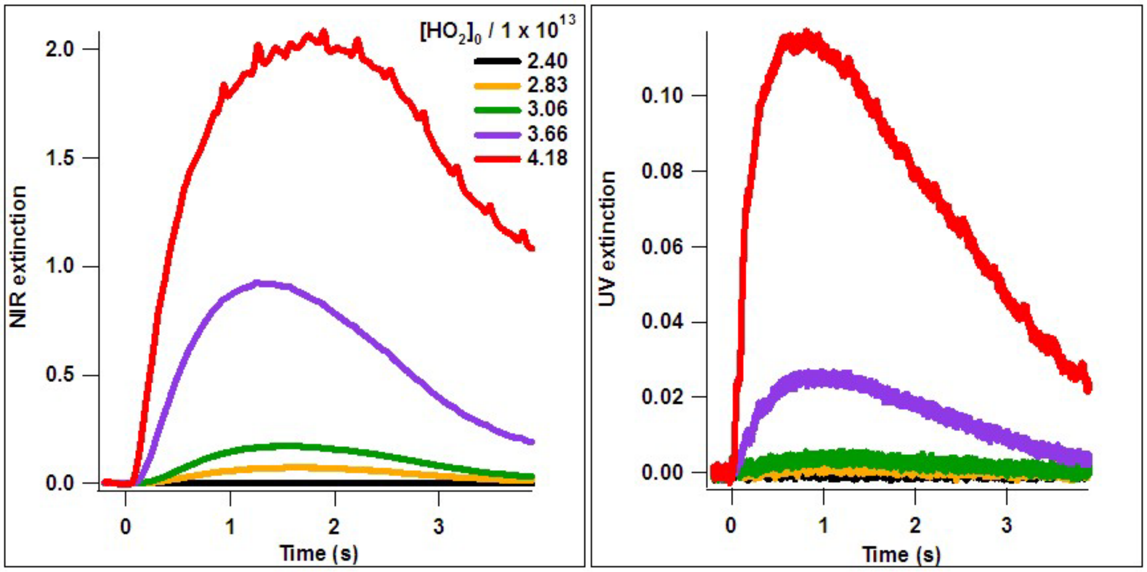

Figure 4-5. Extinction in both the NIR and UV increases as a function of initial radical concentration when radical concentration was < 5 x 10^{13} molecules cm^{-3}.

The peak extinction was very sensitive to $[HO_2]_0$, and **Figure 4-5** shows the large changes in extinction for small changes in $[HO_2]_0$. Unfortunately, as with the $[CH_3OH]$ dependence, no reliable quantitative dependence on $[HO_2]_0$ was determined. **Figure 4-6** plots the peak UV extinction vs. $[HO_2]_0$ for various RH_{CH3OH}. Some of the data appears to have a linear dependence on $[HO_2]_0$, but the trends were not taken over a large enough range to be certain.

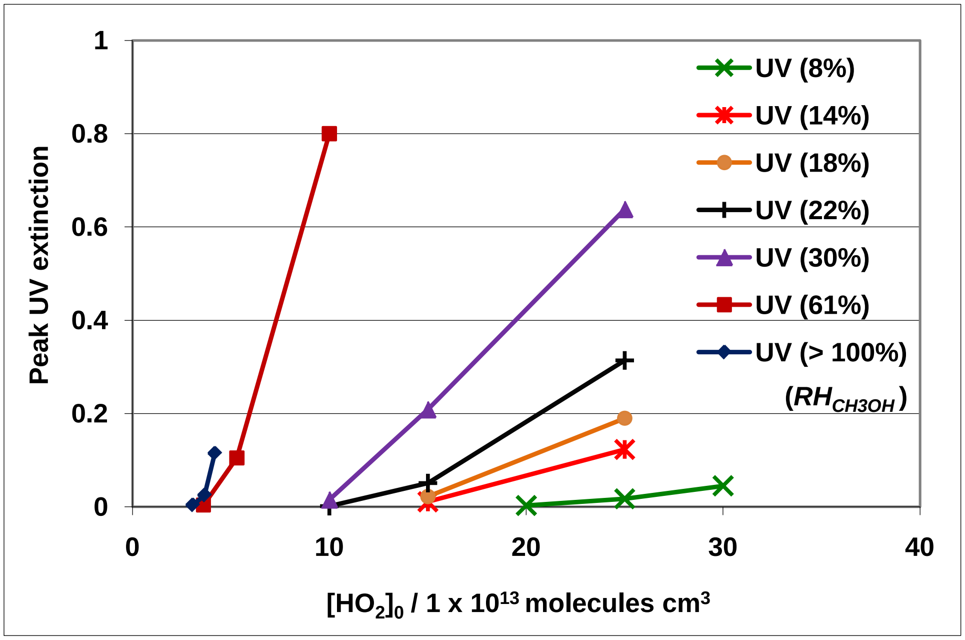

Figure 4-6. Peak UV extinction as a function of initial radical concentration for various RH_{CH3OH}. Lines are only to guide the eye.

The qualitative behavior followed the expected trend; at the lowest RH_{CH3OH} (given in parenthesis in the chart legend) the largest $[HO_2]_0$ was needed to see any nucleation, and as RH_{CH3OH} increased progressively less $[HO_2]_0$ was needed to observe the same amount of extinction. Combining the qualitative observation of increased extinction at increased initial radical with the fact that photolysis was necessary for nucleation, confirmed that radical chemistry was the seed for particle formation.

4.3.5 UV vs NIR dependences

In contrast to data taken at lower $[HO_2]_0$ where the UV and NIR extinctions have a similar dependence on initial radical concentration (**Figure 4-5**), the behavior observed by the two probes started to diverge when $[HO_2]_0$ was raised. **Figure 4-7** compares the UV and NIR extinction as $[HO_2]_0$ was raised above 5 x 10^{13} molecules cm^{-3} at 222 K and

RH_{CH3OH} = 61%. At first both the UV and NIR extinctions increased when $[HO_2]_0$ was raised from 3.6 x 10^{13} → 5.3 x 10^{13}, and the higher sensitivity of the NIR detected nucleation even when the UV did not. But at the highest $[HO_2]_0$ the NIR extinction decreased while the UV increased dramatically and started rippling behavior. The timing of the peak extinction in the UV was also relatively constant while the NIR peak appeared earlier and earlier as $[HO_2]_0$ went up.

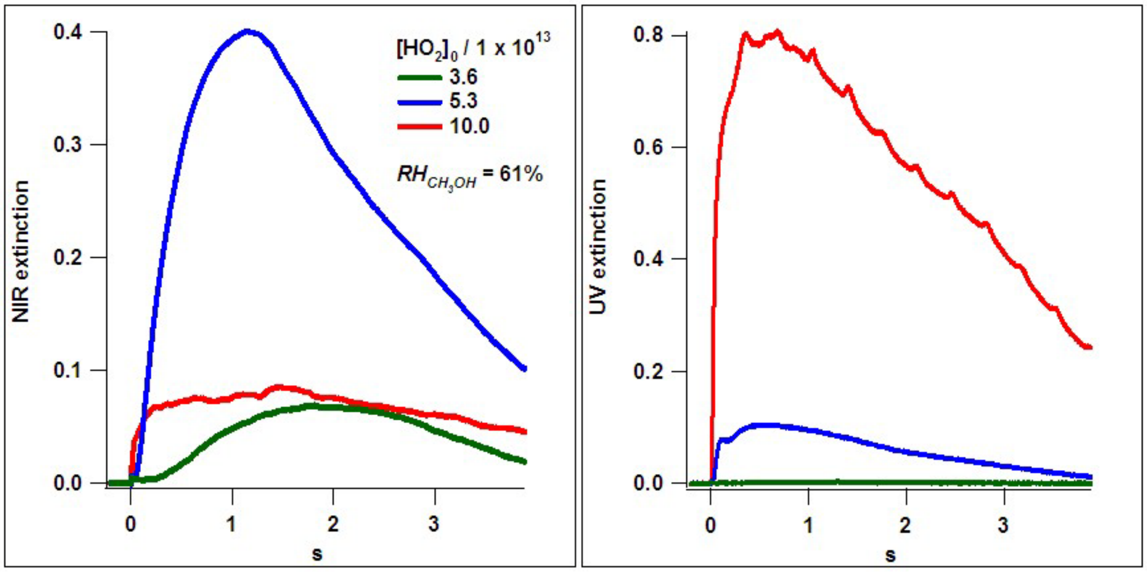

Figure 4-7. Comparison of extinction between the UV and NIR at higher $[HO_2]_0$. NIR extinction was reduced past a certain amount of $[HO_2]_0$.

Increasing the amount of $[HO_2]_0$ seed increases the total number of aerosol possible, but the individual size of each aerosol may decrease. A shift in the size distribution of the aerosol could explain the difference in the extinction observed by the two probes as smaller particles would not extinguish the longer wavelength NIR probe as efficiently as the shorter wavelength UV. Large particles would also take longer to grow, hence the time dependence seen in the NIR as well.

4.3.6 $C_2H_5O_2$

Changing the chemistry of the mixture was a way to probe what was responsible for seeding the particles. **Figure 4-8** shows the effect of adding in ethane (C_2H_6) to create $C_2H_5O_2$ through reactions (4.10) and (4.11).

$$\mathrm{Cl} + \mathrm{C_2H_6} \longrightarrow \mathrm{C_2H_5} + \mathrm{HCl} \tag{4.10}$$

$$\mathrm{C_2H_5} + \mathrm{O_2} \xrightarrow{M} \mathrm{C_2H_5O_2} \tag{4.11}$$

Competition between ethane and CH_3OH for the radical chlorine (Cl) atoms dictates the amount of $C_2H_5O_2$ vs. HO_2 produced. The rate constant for each reaction is very similar (~ 5 x 10^{-11} cm^3 $molecule^{-1}$ s^{-1})[17] so the amount of each product formed is in proportion to the amount of each precursor. A control containing no CH_3OH, 8.0 x 10^{16} molecules cm^{-3} ethane, and an initial radical concentration of 1.0 x 10^{14} molecules cm^{-3} was measured as well. Without CH_3OH no nucleation should have been possible because it made up the bulk of the particle. The yellow trace represents this control run in **Figure 4-8,** and lies behind those containing methanol showing no sign of nucleation in either the NIR or UV. Next CH_3OH was added in and ethane was reduced until it was nine times the concentration of CH_3OH. This data is the purple trace and looks exactly like the control run without CH_3OH; i.e., no nucleation was observed by either probe for this run either. At an ethane concentration of 2.5 x 10^{16} molecules cm^{-3} (~ 3 x [CH_3OH]) the UV still showed no nucleation, but the more sensitive NIR showed a peak at later times. As ethane was reduced again, the NIR reached its largest extinction while the UV was just beginning to be visible. The UV extinction continued to get larger with the further reduction of ethane while the NIR had already peaked and was getting smaller although the rise time of the signal continued to get faster.

These data also provided another good example of the NIR dependence at large $[HO_2]_0$. As the amount of CH_3OH chemistry increased (by reducing the competition from ethane), the amount of radical seed also increased, which led to an initial rise followed by a decline in the NIR peak extinction.

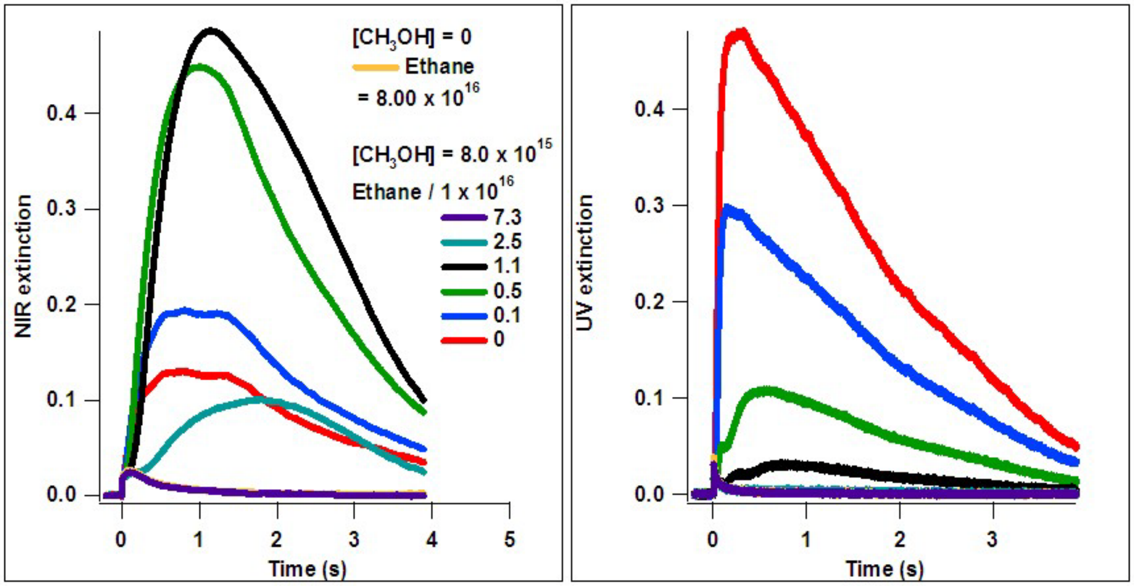

Figure 4-8. Changing the chemistry of the nucleation to include $C_2H_5O_2$ provided some insight into the seed molecule. The different behavior of the UV and NIR at larger radical concentrations was also clearly observed here as well.

The precursor chemistry common to both CH_3OH and ethane are reactions (4.2) and (4.10) where H atom abstraction by Cl forms HCl. Regardless of the precursor ratio of ethane and CH_3OH the same amount of HCl will be produced at a given initial radical concentration. In the data where CH_3OH was present (making nucleation possible), comparing the data at the highest ethane (purple trace) of **Figure 4-8** to all of the subsequent traces showed that HCl was not the nucleation seed. No nucleation was observed in the purple, but it was later on when the only change was the precursor ratio, but as just discussed the precursor ratio does not change the HCl concentration. A further analysis of concentrations from the light blue trace ($[C_2H_6 = 2.5 \times 10^{16}$ molecules $cm^{-3})$

suggests that another species in the HO_2• CH_3OH chemistry can also be ruled out as the nucleation seed: HOOH. For this sample, ~ 1/4 of the 1 x 10^{14} radicals will be HO_2 based on the precursor ratio of ethane and CH_3OH. This $[HO_2]_0$ = 2.5 x 10^{13} was close to the lower limit at which nucleation was observed in any of the previous data, as can be seen in **Figure 4-5**. In this case however ~ 90% of the HO_2 will not self react to form HOOH, but will react instead with $C_2H_5O_2$, lowering the concentration of HOOH by ~ 1 order of magnitude. This suggests that HOOH was also not the radical seed; otherwise data at lower radical concentrations where ethane was not present and all of the HO_2 forms HOOH would have shown nucleation.

4.3.7 Acetone and Water

Nucleation was investigated in the presence of other HO_2 hydrogen bonding partners as well. It is well known that HO_2 forms a hydrogen bonded complex with water,[18-20] and if the HO_2• CH_3OH complex is the seed of the observed nucleation, it is possible that a HO_2• H_2O complex might also prompt nucleation. At both 273 and 254 K, with up to 1.5 x 10^{16} molecules cm^{-3} of H_2O, no nucleation was observed. Theoretical work from a few groups has also suggested that acetone might form a complex with HO_2 at low temperature.[21-23] During work with Professor Fred Grieman, nucleation was observed at high acetone concentrations while measuring the K_{eq} for the reaction of HO_2 with acetone at temperatures of 222 and 213 K.[24] In these experiments nucleation was not observed for samples that only included CH_3OH, the addition of acetone was necessary to observe the nucleation.

4.3.8 Nucleation with no O_2 present

Nucleation from mixtures of Cl_2/CH_3OH, but without O_2, exhibited even greater extinction than those with O_2. The observed nucleation was so much greater that it was likely due to a very different process than the one observed with O_2. In this case it was likely that polymerization reactions of the CH_2OH radical were dominant. Similar behavior with and without O_2 has been observed in photoinduced nucleation of aldehyde systems.[25,26]

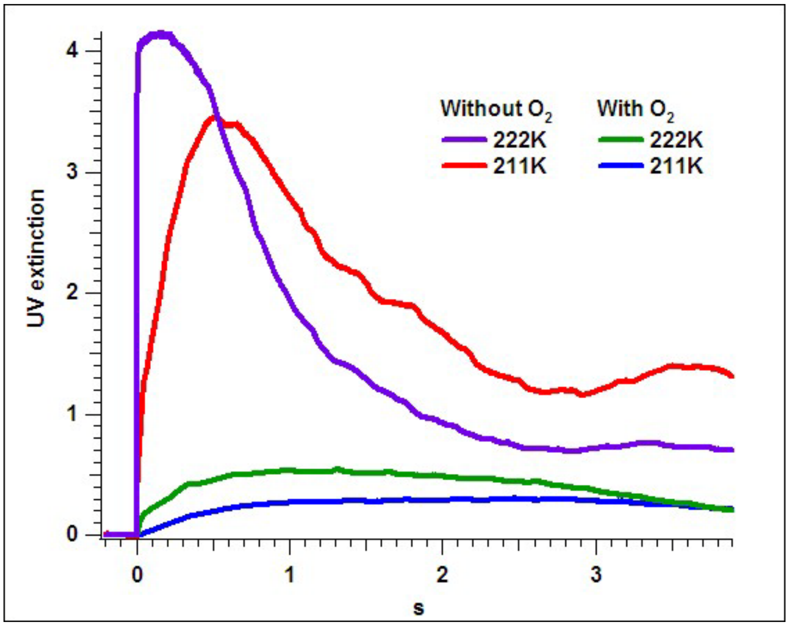

Figure 4-9. Greater extinction was observed in the absence of O_2, suggesting polymerization of the CH_2OH radical.

When O_2 is present at concentrations of ~ 1 x 10^{18} molecules cm^{-3} the reaction of CH_2OH with O_2 happens very quickly (10^7 s^{-1}). Reaction between CH_2OH and CH_3OH would have had to occur at the gas kinetic rate to have any chance of being competitive with the O_2 reaction pathways (10^6 s^{-1}). Therefore it is likely that the observed nucleation had different seeds in the absence and presence of O_2. Rate constants are also not nearly as sensitive to temperature as phase changes. Since even one degree Kelvin can mean a difference between no observed nucleation and large extinctions, it is unlikely the $CH_2OH + CH_3OH$ reaction is suddenly favored over the $CH_2OH + O_2$ reaction.

4.4 Discussion

4.4.1 The nucleation dependence on temperature, [CH_3OH], and [HO_2]$_0$

The large extinctions observed in both the UV and NIR are thought to be caused by aerosol formation due to their strong non-linear dependence on temperature, [CH_3OH], and [HO_2]$_0$. The [CH_3OH] dependence data are convincing evidence that CH_3OH made up the bulk of the particles, and the [HO_2]$_0$ dependence is confirmation that radical chemistry provided the nucleation seed. Increasing the [CH_3OH] provided more material for the aerosol to form and resulted in greater extinction. Likewise increasing [HO_2]$_0$ provided more seeds for nucleating aerosol and led to greater extinction as long as an excess of CH_3OH existed.

Some of the most intriguing potential from these experiments comes from the observed difference in extinction between the UV and the NIR as the nucleation seed increased. The decrease in the NIR extinction as [HO_2]$_0$ increased (shown in **Figure 4-7** and **4-8**) can be explained by a shift in the particle size distribution. More seed leads to the growth of a greater number of smaller particles, but fewer larger ones. The resulting extinctions in the NIR and UV were an example of how different wavelengths of light can be used to probe different size scales of nucleation and particle growth simultaneously. The time delay in the NIR peak at the lowest concentrations of [CH_3OH] and [HO_2]$_0$, in comparison to the uniform time dependence of the UV, is another example of how the different wavelengths can focus on different stages of growth. The different behaviors also suggest that specific aspects of nucleation can be targeted by using different chemistry regimes, i.e., different [CH_3OH] and [HO_2]$_0$.

The strong oscillations observed in the temperature dependence data of **Figure 4-2** were another optical effect that might be exploited to get information about the size distribution of the aerosol. The wiggles in the extinction are expected from Mie theory when particles approach the size of the wavelength of the incident light.[27] The very similar period of the wiggles for both the NIR and UV in **Figure 4-2** might also indicate another explanation, such as a dynamical effect from the flow system. For example, the pump out of aerosols and the pump in of fresh CH_3OH flow lead to an oscillation in the growth and disappearance of the aerosol. However, the fact that the oscillations appear in other data, but not always in both the UV and NIR make a flow explanation less convincing. A true analysis of the data using Mie theory requires some estimation of the particle number and size distribution and proposed experiments are described in the Future Work section.

4.4.2 Chemistry changes and seed possibilities

The work discussed so far reports the growth of already formed aerosol, not the actual nucleation process. Nucleation occurs in clusters too small to observe with the present experiment, so only the already formed aerosols were large enough to cause extinction of the light. A different way to investigate the actual nucleation process was also tried by changing the initiation chemistry leading up to it. The $C_2H_5O_2$ work ruled out HOOH and HCl as the species acting as a nucleation seed, but still left HO_2 and HCHO, as both were made in equal amounts when HO_2 was formed. With these species present there are two possible mechanisms for nucleation. In the first, shown in reaction

(4.8), the HO_2• CH_3OH complex can continue to add CH_3OH until a critical cluster size is passed, leading to particle formation. Another version of this mechanism involves the interaction of multiple complexes to help form the critical cluster, but is otherwise the same. The second mechanism is a binary nucleation process between the HCHO and CH_3OH. In many cases during these experiments RH_{CH3OH} was less than 100% which precludes homomolecular homogenous nucleation from occurring. However the mixture of HCHO and CH_3OH could have a much lower vapor pressure leading to their condensation in heteromolecular homogenous nucleation. It has been observed in the case of H_2O-H_2SO_4 mixtures that even trace amounts of H_2SO_4 can greatly increase nucleation.[28]

The concentrations used in this experiment are not directly applicable to the atmosphere. Even if the HO_2• CH_3OH was proven to be the seed, it might have only limited direct atmospheric importance since no nucleation was observed in the presence of the most important complex of HO_2 in the atmosphere, HO_2• H_2O. Still one interesting part of this work is the incorporation of a very light molecular weight species into aerosol. Atmospheric chemistry models consistently under predict aerosol concentrations in comparison to what is actually measured.[29] One reason for this is that low molecular weight species have been largely ignored based on their Henry's law constants. Work on isoprene oxidation and aerosol formation has shown that low molecular weight glyoxal forms aerosol,[30] and recent work on the photolysis of acetylene shows that it too can form aerosol under the right conditions.[31] Even more species are likely to be important for a variety of reasons, and heterogeneous radical chemistry may provide one way to further incorporate lower molecular weight species into pre-existing particles. The radical-molecule complex of this work may not be relevant to atmospheric nucleation specifically, but it may provide another route for pre-existing particle growth.

4.4.3 Future experiments

Two different experiments could help resolve the nucleation mechanism. The first would be to simply add a small amount of HCHO to the exact same flow and temperature conditions used in this work to see if the trace HCHO leads to binary nucleation. An alternative experiment is to generate HO_2 in such a way that HCHO is not also created. One possibility to generate HO_2 is photolysis of H_2O_2. Another common source of HO_2, $F_2/H_2/O_2$ chemistry, would be complicated by the F atom reacting with the CH_3OH and potentially leading to HCHO again.

Other experiments would also be useful to investigate the number and size distributions of the observed aerosol. For instance, the introduction of a sample from the flow cell exhaust into a particle counter would help to characterize the aerosol. Experimentally it would be difficult to maintain the low temperature throughout the system to prevent evaporation of the aerosol, but information on total particle number would help greatly in interpreting the measured extinctions.

4.5 Conclusion

Low temperature experiments on the HO_2 self reaction led to surprising observations of photoinduced nucleation of aerosols. Varying the precursor chemistry allowed definitive assignment of CH_3OH as the main condensing species, and either HO_2 or HCHO chemistry as the nucleation seed. The different response of the extinction in the UV and NIR probes gave an indication of the size regime of the aerosol being formed. Although the specific system is probably not directly relevant to the atmosphere given the concentrations used, the possibility of radical induced nucleation or binary nucleation of two low molecular weight species could be important analogs to processes currently overlooked in aerosol models.

4.6 References

(1) O'Dowd, C. D.; Hameri, K.; Makela, J. M.; Pirjola, L.; Kulmala, M.; Jennings, S. G.; Berresheim, H.; Hansson, H. C.; de Leeuw, G.; Kunz, G. J.; Allen, A. G.; Hewitt, C. N.; Jackson, A.; Viisanen, Y.; Hoffmann, T. *Journal of Geophysical Research-Atmospheres* **2002**, *107*.

(2) Laakso, L.; Anttila, T.; Lehtinen, K. E. J.; Aalto, P. P.; Kulmala, M.; Horrak, U.; Paatero, J.; Hanke, M.; Arnold, F. *Atmospheric Chemistry and Physics* **2004**, *4*, 2353.

(3) Poschl, U. *Angewandte Chemie-International Edition* **2005**, *44*, 7520.

(4) Kulmala, M. *Science* **2003**, *302*, 1000.

(5) Hegg, D. A.; Baker, M. B. *Reports on Progress in Physics* **2009**, *72*, 21.

(6) Textor, C.; Schulz, M.; Guibert, S.; Kinne, S.; Balkanski, Y.; Bauer, S.; Berntsen, T.; Berglen, T.; Boucher, O.; Chin, M.; Dentener, F.; Diehl, T.; Easter, R.; Feichter, H.; Fillmore, D.; Ghan, S.; Ginoux, P.; Gong, S.; Kristjansson, J. E.; Krol, M.; Lauer, A.; Lamarque, J. F.; Liu, X.; Montanaro, V.; Myhre, G.; Penner, J.; Pitari, G.; Reddy, S.; Seland, O.; Stier, P.; Takemura, T.; Tie, X. *Atmospheric Chemistry and Physics* **2006**, *6*, 1777.

(7) Kanakidou, M.; Seinfeld, J. H.; Pandis, S. N.; Barnes, I.; Dentener, F. J.; Facchini, M. C.; Van Dingenen, R.; Ervens, B.; Nenes, A.; Nielsen, C. J.; Swietlicki, E.; Putaud, J. P.; Balkanski, Y.; Fuzzi, S.; Horth, J.; Moortgat, G. K.; Winterhalter, R.; Myhre, C. E. L.; Tsigaridis, K.; Vignati, E.; Stephanou, E. G.; Wilson, J. *Atmospheric Chemistry and Physics* **2005**, *5*, 1053.

(8) Kathmann, S. M.; Schenter, G. K.; Garrett, B. C.; Chen, B.; Siepmann, J. I. *Journal of Physical Chemistry C* **2009**, *113*, 10354.

(9) Kulmala, M.; Kerminen, V. M. *Atmospheric Research* **2008**, *90*, 132.

(10) O'Dowd, C. D.; De Leeuw, G. "Marine aerosol production: a review of the current knowledge", 2007.

(11) Belair, S. D.; Hernandez, H.; Francisco, J. S. *Journal of the American Chemical Society* **2004**, *126*, 3024.

(12) Shi, Q. C.; Belair, S. D.; Francisco, J. S.; Kais, S. *Proceedings of the National Academy of Sciences of the United States of America* **2003**, *100*, 9686.

(13) Christensen, L. E.; Okumura, M.; Hansen, J. C.; Sander, S. P.; Francisco, J. S. *Journal of Physical Chemistry A* **2006**, *110*, 6948.

(14) Christensen, L. E.; Okumura, M.; Sander, S. P.; Salawitch, R. J.; Toon, G. C.; Sen, B.; Blavier, J. F.; Jucks, K. W. *Geophysical Research Letters* **2002**, *29*.

(15) Christensen, L. Laboratory studies of atmospherically important gas-phase peroxy radical reactions. , California Insitute of Technology, 2003.

(16) Christensen, L. E.; Okumura, M.; Sander, S. P.; Friedl, R. R.; Miller, C. E.; Sloan, J. J. *Journal of Physical Chemistry A* **2004**, *108*, 80.

(17) Sander, S. P.; Finlayson-Pitts, B. J.; Friedl, R. R.; Golden, D. M.; Huie, R. E.; Kolb, C. E.; Kurylo, M. J.; Molina, M. J.; Moortgat, G. K.; Orkin, V. L.; Ravishankara, A. R. "JPL 2006: Chemical Kinetics and Photochemical Data for Use in Atmospheric Studies, Evaluation No. 15, JPL Publication 06-2, Jet Propulsion Lab," 2006.

(18) Hamilton, E. J. *Journal of Chemical Physics* **1975**, *63*, 3682.

(19) Hamilton, E. J.; Lii, R. R. *International Journal of Chemical Kinetics* **1977**, *9*, 875.

(20) Suma, K.; Sumiyoshi, Y.; Endo, Y. *Science* **2006**, *311*, 1278.

(21) Cours, T.; Canneaux, S.; Bohr, F. *International Journal of Quantum Chemistry* **2007**, *107*, 1344.

(22) Hermans, I.; Muller, J. F.; Nguyen, T. L.; Jacobs, P. A.; Peeters, J. *Journal of Physical Chemistry A* **2005**, *109*, 4303.

(23) Hermans, I.; Nguyen, T. L.; Jacobs, P. A.; Peeters, J. *Journal of the American Chemical Society* **2004**, *126*, 9908.

(24) Grieman, F. J., Noell, A.C., Okumura, M., Sander, S.P. **Manuscript in preparation**.

(25) Dubtsov, S. N.; Dultseva, G. G.; Dultsev, E. N.; Skubnevskaya, G. I. *Journal of Physical Chemistry B* **2006**, *110*, 645.

(26) Skubnevskaya, G. I.; Dubtsov, S. N.; Dultsev, E. N.; Dultseva, G. G.; Tsang, W. *Journal of Physical Chemistry B* **2004**, *108*, 11393.

(27) Seinfeld, J. H., Pandis, S.N. Atmospheric Chemistry and Physics; John Wiley and Sons: New York, 1998; pp 82.

(28) Ball, S. M.; Hanson, D. R.; Eisele, F. L.; McMurry, P. H. *Journal of Geophysical Research-Atmospheres* **1999**, *104*, 23709.

(29) Volkamer, R.; Jimenez, J. L.; San Martini, F.; Dzepina, K.; Zhang, Q.; Salcedo, D.; Molina, L. T.; Worsnop, D. R.; Molina, M. J. *Geophysical Research Letters* **2006**, *33*.

(30) Kroll, J. H.; Ng, N. L.; Murphy, S. M.; Flagan, R. C.; Seinfeld, J. H. *Environmental Science & Technology* **2006**, *40*, 1869.

(31) Volkamer, R.; Ziemann, P. J.; Molina, M. J. *Atmospheric Chemistry and Physics* **2009**, *9*, 1907.

5 Experimental work

5.1 Experimental setup

The experimental apparatus was already constructed when I began my research, and has been described in a paper and thesis by Dr. Lance Christensen.[1,2] This chapter provides more details on the operating conditions of the apparatus during the work presented in Chapters 2 and 4, and describes experiments conducted to further characterize the apparatus. **Figure 5-1** presents a schematic overview of the setup.

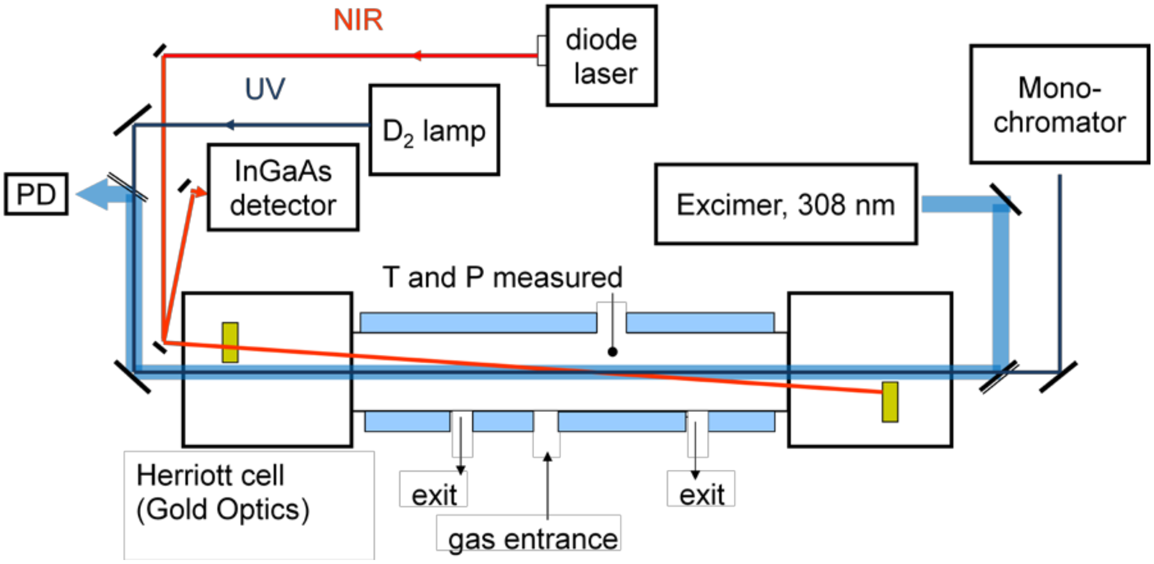

Figure 5-1. IRKS apparatus. A jacketed flow cell is coupled to an excimer laser for flash photolysis kinetics experiments. Two detection probes, near-IR light from a diode laser and UV light from a deuterium lamp are monitored simultaneously. The NIR probe makes 30 passes back and forth through the cell using Herriott mirrors slightly off axis to the photolysis pulse. The UV probe is coaligned, but propagating in the opposite direction of the photolysis pulse.

The main glass cell was jacketed to allow for temperature control using liquid-nitrogen-chilled methanol as a coolant. The cell was connected with O-ring seals to mirror housing boxes on either end where the near infrared (NIR) Herriott cell mirrors were located. Calcium fluoride (CaF_2) windows on the boxes allowed transmittance of the NIR, ultraviolet (UV), and excimer beams. Pre-cooled gasses flowed into the cell through an off-center entrance port and then out of the cell at two exit ports on either side of the cell. The total path length between the centers of the exit ports was 138 cm. Room temperature nitrogen purge gas entered the experiment through each mirror housing box as well (not illustrated above). This purge gas met the reactant gas at the exit ports to confine the reactant gas to the temperature controlled region. The total path length from the window of one mirror box to the window of the other was 208 cm. All flows were monitored using mass flow meters (Hasting HFM-200 series). The volume of the reactant flow region of the cell was ~2900 cm^3. Total flow velocities were calculated to determine the residence time of gas in the cell, i.e., the amount of time elapsed before an entirely new fill of gas occupied the cell. Residence times were typically on the order of 10 s. At a second off center port a Type T thermocouple (Omega) was threaded into the cell to measure the temperature, and a capacitance manometer (MKS-220CA 1000 Torr) was connected to measure pressure. Similar capacitance manometers were used to measure the pressure inside of the bubblers that brought vapor from liquid reagents to the flow cell.

A XeCl excimer laser (308 nm, ~ 100 mJ/pulse) was the photolysis laser, and made one pass through the cell. The laser pulse was recorded by a photodiode in order to signal the data acquisition program that a successful run had occurred. The laser generally operated at a repetition rate which allowed for one whole gas residence time to pass before firing again, e.g., for a residence time of 10 s the excimer operated at 0.1 Hz. Light from a 150 W deuterium (D_2) lamp (Hamammatsu L1314) also made one pass through the cell co-aligned but counter-propagating with the excimer beam. Dichroic mirrors were used to reflect the 308 nm excimer, but allow the deuterium light < 300 nm to pass. NIR light from a distributed feedback diode laser passed through the cell 30 times reflecting back and forth off of two spherical gold mirrors in a Herriott cell configuration. These mirrors were placed slightly off the axis of the photolysis laser to allow the photolysis pulse to pass above and below the mirrors, respectively.

The diode laser was wavelength modulated (WM) to reduce the amount of noise in the absorption signal. A diagram and description of the WM set up and detection electronics are given in Section 5.5.1.

The data acquisition was controlled by a visual BASIC program. Pressures, flows, and the excimer firing signal were recorded with a NIDAQ data acquisition card (National Instruments CB68LP). The data signals from the NIR and UV probes were digitized using a two-channel 16 bit per channel A/D card with a maximum sampling rate of 2.5 MS/s (Gage-CompuScope 1602). The data was low pass filtered (SR560) before collection, and the filter setting was determined by the sampling rate. The Nyquist theorem dictates that signals at frequencies greater than one half the sampling rate will lead to aliasing, so for a typical sampling rate of 200 kSa/s the low pass filter was set to 100 kHz.

5.2 Absorption measurements

The goal of the IRKS apparatus is to measure kinetics and thermodynamics for a variety of peroxy radical (RO_2) chemistry. Experiments are put on an absolute scale by the concentrations determined from absorption in the UV. Beer’s law shown in equation (5.1), relates the absorbance, A, to the concentration, [Conc] (molecules cm^{-3}), of the absorbing species through a proportionality constant made up of the product of the path length l (cm) and the absorption cross section σ (cm^{2} molecule^{-1}).

$$A = [\text{Conc}] * l * \sigma \tag{5.1}$$

Absorbance measurements were performed for a variety of reasons including verifying methanol (CH_3OH) concentrations, verifying the reactant flow path length, measuring absorption cross sections, and verifying acetone concentrations. Work done in collaboration with graduate student Aileen Hui and Professor Fred Grieman also indirectly probed the path length by measuring the temperature profile along the length of the apparatus. Path length and absorption cross section measurements were necessary because both values are central to measuring absolute concentrations and absolute kinetics with the apparatus.

5.2.1 Experimental setup and verification

The initial absorption measurements were done with penray lamps (Hg at 185 nm and Zn at 214 nm). The setups for both penray experiment are shown in **Figure 5-2**. The flow cell was set up the same as it was for kinetics experiments, but the optics for the excimer laser, D_2 lamp, and diode laser were all removed to allow positioning of the penray lamp and photomultiplier tube (PMT) detector. A different PMT with a different photocathode was used depending on the penray lamp; a Cs-I photocathode was used for the Hg penray and a bialkali photocathode was used for the Zn penray. To obtain sufficient signal the Zn setup also required using 6 and 5 cm focal length optics at the entrance and exit of the cell, respectively. A picoammeter was used to read out the signals in both setups.

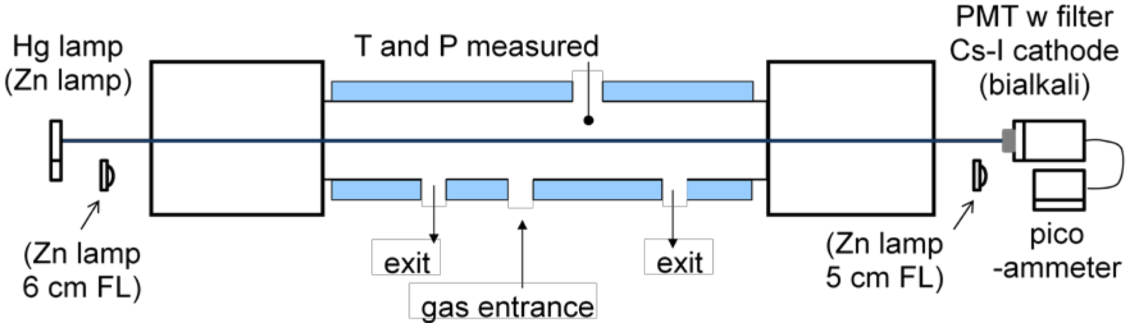

Figure 5-2. Setup for penray lamp experiments. To look at the 185 nm line from the Hg lamp a Cs-I photocathode PMT was used to reduce all light at λ > 190 nm. For the 214 nm line from the Zn lamp it was necessary to use focusing optics before and after the cell with a bialkali photocathode PMT. For both lamps a filter was used at λ = 185 or 214 nm to attenuate other wavelengths.

Absorption experiments were also done using the D_2 lamp as the light source, and were setup exactly as the normal kinetics experiments were in **Figure 5-1**. In a few cases a Cary UV-Vis spectrometer was used to verify absorption cross sections. A list of all the molecules that were studied including the method and λ that they were studied at is given in **Table 5-1**.

Table 5-1. Summary of all the molecules and λ where absorption measurements were made.

Molecule	λ (nm)	source	$\sigma_{\text{full cell}}$ / (cm^2)	σ_{lit} / (cm^2)	Path Length (cm) (100 Torr, 10 s res , 100% purge)
CH_3OH	185	Hg penray		6.30×10^{-19} [b]	
N_2O	214	Zn penray	3.35×10^{-21}	3.60×10^{-21} [b]	
N_2O	214	Cary	3.37×10^{-21} [a]		
N_2O	185	Hg penray	1.27×10^{-19}	1.40×10^{-19} [c]	
N_2O	185	Cary	1.36×10^{-19} [a]		
CF_3Br	185	Hg penray	4.23×10^{-20}	4.45×10^{-20} [c]	
CF_3Br	185	Cary	4.44×10^{-20} [a]		
CF_3Br	220	D_2 lamp	7.45×10^{-20}	7.56×10^{-20} [c]	149
Cl_2	295	D_2 lamp	8.52×10^{-20}	8.85×10^{-20} [c]	149
Acetone	275	D_2 lamp	4.96×10^{-20}	4.96×10^{-20} [b]	161

[a] Measurements were made in a 10 cm cell in the Cary spectrometer, [b] MPI-Mainz UV database,[3] [c] JPL-06 recommendation[4]

Absorption measurements were first attempted to verify the [CH_3OH] in the flow cell. The 185 nm line of the Hg penray lamp was used as a light source because of the suitable absorption cross section of CH_3OH at this wavelength. Measurements of N_2O at 185 and 214 nm, and CF_3Br at 185 nm followed in order to check the experimental setup. CH_3OH was introduced into the cell by bubbling N_2 through liquid CH_3OH held at 0 °C (V.P. 30 Torr)[5] and monitoring the total pressure in the bubbler. The N_2O and CF_3Br were supplied directly from gas cylinders. Nitrogen calibrated flow meters were used to monitor the flows of all gases by using the appropriate correction factors (0.75 for N_2O and 0.37 for CF_3Br) where necessary. The concentrations of each species in molecules cm^{-3} were: [CH_3OH] = $5 \times 10^{14} - 1 \times 10^{16}$, [$N_2O$] (185 nm) = $9 \times 10^{15} - 1.8 \times 10^{17}$, [$N_2O$] (214 nm) = $3 \times 10^{17} - 2 \times 10^{18}$, and [$CF_3Br$] = $3 \times 10^{16} - 3 \times 10^{17}$. The high voltage supplied to the PMTs was typically between 600 and 900 V.

Measurements were performed by measuring the intensity of light coming through the cell without any of the absorbing gas present, and then by measuring the light with a series of 4 – 5 different concentrations of the absorber present. A check of the baseline intensity was performed after evacuating the cell, and the measurements repeated. Fluctuations in the measured signal were a common problem. The estimated precision of the signal measurements from the picoammeter due to these fluctuations was $\pm$ 0.005 μA.

The first attempts at penray measurements using the 185 nm Hg line failed because of light from both 254 and 194 nm lines leaking through the single 185 nm filter being used. Good measurements were made by either using two 185 nm filters (Acton 185-HR-1D-MTD) or one filter and a PMT with a Cs-I photocathode. A Cs-I photocathode attenuates light at λ > 190 nm, and was used in penray measurements done by Cantrell et al. and Creasey et al on N_2O absorption.[6,7] **Figure 5-3** shows the absorbance plots for N_2O at 185 nm with the bialkali and Cs-I PMTs. The curvature was obvious in the bialkali case.

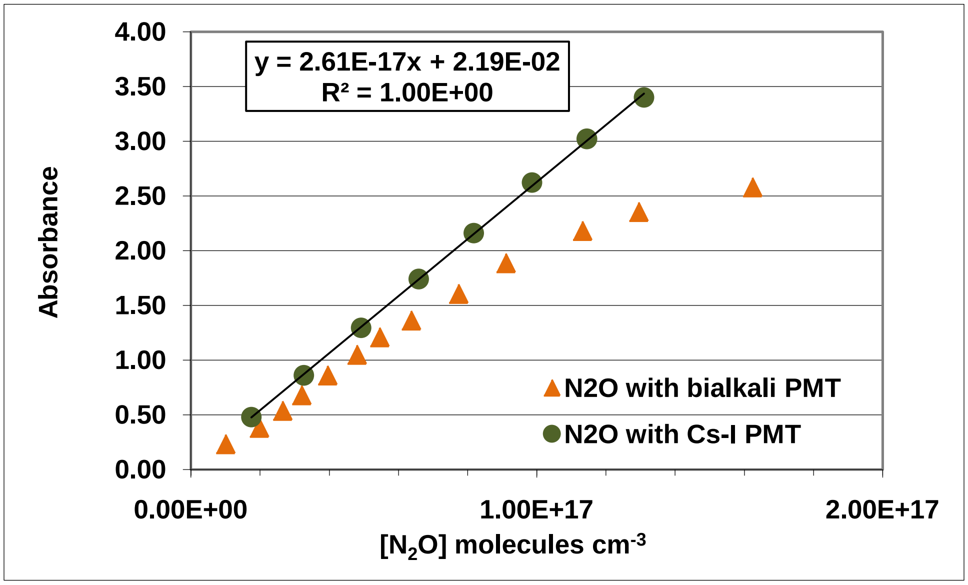

Figure 5-3. Curvature in the absorbance plot for N_2O was seen when using the PMT with the bialkali photocathode, but not when using the Cs-I photocathode.

Static cell and Cary spectrometer measurements of the absorption cross sections for N_2O and CF_3Br were made to verify the values from the literature. The static cell measurements used the 208 cm path length that was fixed by the window – window distance of the kinetics cell. Each gas was allowed to fill the cell, and the total concentration was determined from the pressure in the cell by using the ideal gas law. For the Cary measurements a 10.5 cm cell with NaCl windows was attached to the main kinetics cell to fill, and then was taken to the Cary. For each concentration 15 s averages were recorded 10 times and then those 10 recordings were averaged. The spectral bandwidth was 0.5 nm. Some clear nonlinearity could be observed in the Cary absorbances, but these could be fit with equation (5.2) to give good cross section values.

$$I_t = I_0\left(e^{-(\sigma * l * c)} + \mathrm{E}\right) \qquad (5.2)$$

E is the error term associated with the nonlinearity and was usually around 0.05. All of the measured cross sections and their literature values are shown in **Table 5-1**. Good agreement was seen between the CF_3Br and N_2O cross sections measured and their literature values, verifying the overall absorption measurements.

5.2.2 [CH_3OH] measurements

Using the procedure for the 185 nm absorption measurements established with N_2O and CF_3Br, measurements of [CH_3OH] were made under normal flowing conditions for the kinetics flow cell. Concentrations of CH_3OH measured by absorption agreed with the concentrations calculated from the flows when the total pressure in the CH_3OH bubbler was kept above 300 Torr. At pressures < 300 Torr, [CH_3OH] measured was larger than the calculated value. The 300 Torr mark was true for a variety of temperatures as can be seen in **Figure 5-4**. At 222 K, the lowest temperature on the plot, the absorption measurements became nonlinear at 1×10^{16} molecules cm^{-3}. This was also true at 210 K at ~ 1×10^{15} molecules cm^{-3}. Condensation or dimer formation of CH_3OH was probably occurring, making these conditions approximate limits of temperature and CH_3OH for this experiment.

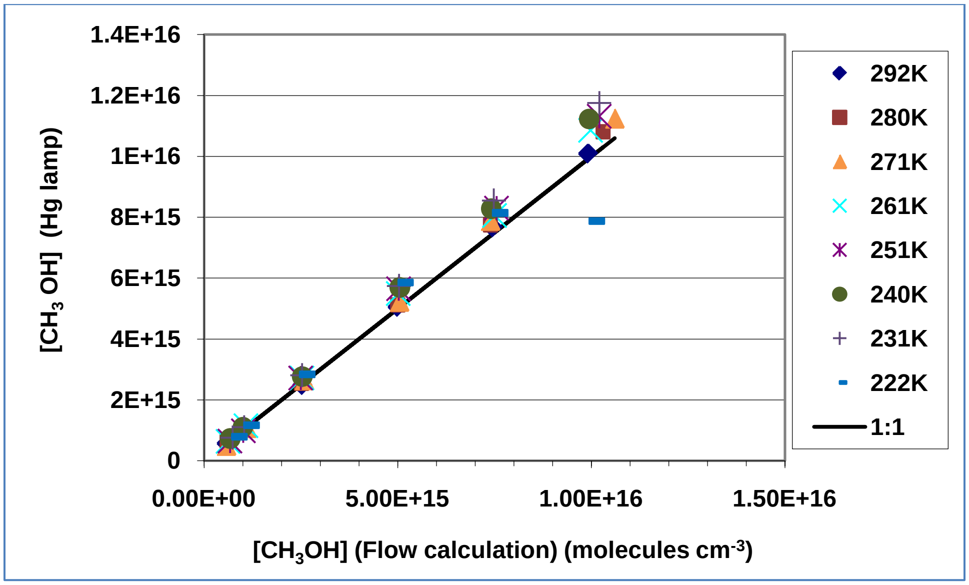

Figure 5-4. [CH_3OH] measured by the Hg lamp agrees with the concentration determined by the flows when the bubbler pressure is above 300 Torr.

The measured values were still slightly larger than the predicted ones. This data was analyzed with a path length of 138 cm, however most of the data fit even better using a path length between 145 and 155 cm. This is in agreement with the path length data discussed next, and is consistent with the current understanding of the flow system.

5.2.3 Path length measurements: Cl_2 and CF_3Br

After observing some counterintuitive kinetics results it was necessary to investigate the reactant path length and how it was affected by pressure, residence time, and the amount of purge flow as a percentage of the total reactant flow. Both Cl_2 and CF_3Br were investigated using the D_2 lamp as a light source so that the absorption measurements could be made in the same optical configuration as the kinetics measurements. Static cell measurements were performed to check the Cl_2 and CF_3Br cross section at 295 and 220 nm, respectively; **Table 5-1** displays the good agreement in those values. Cl_2 measurements were important because Cl_2 was the radical precursor in the kinetics experiments so it was a direct proxy for the radical path length. Agreement between the measured path lengths of Cl_2 and CF_3Br allowed most of the measurements to be carried out with CF_3Br, a safer gas to work with. All of the measurements made with CF_3Br at different flow conditions are shown in **Table 5-2**.

Table 5-2. Path length measurements at different residence times, pressures, and amount of purge flow as a percentage of the total reactant flow.

Residence Time (s)	P (Torr) % purge	50	100	200	400
5	10	156.1	150.8		
5	25	150.8	149.5		
5	50	152.1	149.5		
5	100	150.8			
10	10	152.1	154.8		
10	25	152.1	150.8	*153.4	
10	50	150.8	146.8	*150.8	
10	100	148.1	144.2	*145.5	
15	10	161.4	162.7		
15	25	157.4	156.1	153.4	
15	50	154.8	152.1	149.5	
15	100	149.5	148.1	144.2	
20	15				165.3
20	50				150.8

*Purge flows are not exactly as stated. High pressure and short residence times required flows too large for the system.

The measured path lengths vary over 144 – 165 cm. A number of trends were observed both from the table and from the absorbance plots. The longer the residence time the more important the purge flow became in confining the reactant flow. The same trend was observed for increasing pressure, but it was less dramatic. To place the previous [CH_3OH] measurements in context, they were taken at 100 Torr, 5 s residence time, and 15% purge. From the table they should have shown a path length of ~ 150 cm, in agreement with what was noted as providing the best fit to the data. From **Table 5-2** the best condition for confining the reactant flow to the 138 cm exit port distance was 100

Torr total pressure, 10 s residence time and 100 % purge. These conditions were adopted as the ones to use for kinetics experiments.

5.2.4 Path length measurements: Acetone

A different path length was measured for acetone than for Cl_2 and CF_3Br. These measurements were made during collaboration with Professor Fred Grieman on work investigating the reaction of HO_2 with acetone. Acetone was introduced to the cell in a manner similar to the CH_3OH. A glass bubbler filled with liquid acetone was held at constant temperature and nitrogen gas was bubbled through at a known total pressure. Acetone concentrations ranged from ~ $5 \times 10^{15} – 2 \times 10^{16}$ molecules cm^{-3}. Initial measurements were done to double check the Cl_2 and CF_3Br cross sections using the D_2 lamp in the kinetics setup. Then the acetone cross section at 275 nm was measured in a flowing experiment (not a static experiment), but purge gas was not used so that the reactant flow filled the entire cell path length. Concentration was calculated from the flows and pressures, a method that was previously validated in the CH_3OH measurements. Static cell measurements were not done because of concern that the acetone might stick to the walls of the cell. Concentrations were allowed to stabilize for a few minutes each time the flow was changed during these measurements. **Table 5-1** shows the cross section for acetone and its agreement with the literature value. This further validated the bubbler method for acetone as well as the flow system calculations of concentrations. Path length measurements using acetone were then made under the flowing conditions of choice, i.e., 100 Torr, 10 s residence time, and 100% purge. These measurements consistently saw a path length of 162 cm, ~ 10 cm longer than what the Cl_2 and CF_3Br measured under identical conditions. This path length was consistent over the temperature range 229 – 296 K. No obvious explanation for the path length difference could be found until the next experiments, that used temperature measurements as path length proxies, were able to provide one.

5.2.5 Path length measurements: Temperature probe

The current understanding of the path length was determined by work performed with Aileen Hui and Professor Fred Grieman to measure the temperature profile of the gas along the length of the flow cell. A thermocouple probe was attached to the end of a movable steel rod and a temperature was taken at each point as it was moved throughout the cell. Purge gas flow was at room temperature and the reactant gas flow was at 213 K. By measuring where in the cell the temperature gradient from 296 to 213 occurred it was possible to determine both the length and the absolute location of the mixing between the purge and reactant flows. Under the conditions of 100 Torr, 10 s residence time and 100 % purge, the total path length including the entire mixing region on both sides was ~ 160 cm. The path length connecting the midpoints of the mixing region was ~ 150 cm.

An explanation for the path length difference between acetone and Cl_2/CF_3Br was provided by the difference in the “total” and “midpoint” lengths. A sticky molecule like acetone that can build up concentration on the walls of the cell as a reservoir will have a path length along the whole range of the mixing region even if the initial gas phase amount is diluted. Molecules such as Cl_2 and CF_3Br that do not interact with the walls will appear to have a length that stretches from the midpoint of one mixing region to the other because the more dilute portions of the mixing region do not contribute significantly to the measured path length.

Another measurement was made at 300 Torr that showed the same qualitative behavior, but this time the total length had reached ~ 170 cm and the size of the mixing regions was larger than at 100 Torr. This confirmed doubts about higher pressure kinetics measurements that had been made on HO_2 and RO_2 self reactions (Discussed next in section 0), suggesting that the data was probably unreliable due to the large mixing regions where concentration gradients would lead to different reaction rates occurring. In general the temperature probe measurements provided a much better understanding of the purge and reactant gas dynamics, as well as the measured reactant flow path lengths.

The probe measurements also revealed a temperature offset in some of the data due to misplacement of the fixed thermocouple in the cell. Within a small radius of the port that allowed for the thermocouple and capacitance manometer to be attached to the cell the temperature was higher due to the lack of coolant flowing in that region. When the thermocouple was threaded further down the cell it then agreed with the temperature probe. A calibration was determined and was applied to the data affected during the nucleation experiments described in Chapter 4.

5.3 Pressure dependence of the HO_2 and RO_2 self reactions

One of the motivating factors for more carefully determining the path length was to investigate the pressure dependence of HO_2 and RO_2 self reactions. Initial studies with this system did not observe a pressure dependence for the HO_2 self reaction and actually saw an inverse pressured dependence for the $C_2H_5O_2$ self reaction when looking at data taken with the D_2 lamp (UV) probe. The HO_2 self reaction has a reported pressure dependence, and $C_2H_5O_2$ has been measured as having no pressure dependence so something appeared wrong with the measurements.[4]

The procedure for studying the pressure dependence was to set the bulk flows and pressure at one value, then adjust the Cl_2 concentration from ~ 3 x10^{15} – 1.5 x 10^{16} leading to initial RO_2 concentrations of ~ 3 x 10^{13} – 1.5 x 10^{14} molecules cm^{-3}. The data was analyzed over a variety of different time scales, but the procedure that was settled on was to analyze all the data over a consistent number of half lives for every concentration. Frequently 2 half lives were used, but when possible 3 half lives were used as well.

5.3.1 HO_2 + HO_2

From the data shown in **Figure 5-5** what immediately stood out was the dependence of the UV rate constant for the HO_2 self reaction, $k_{HO2}(UV)$, on initial radical concentration.

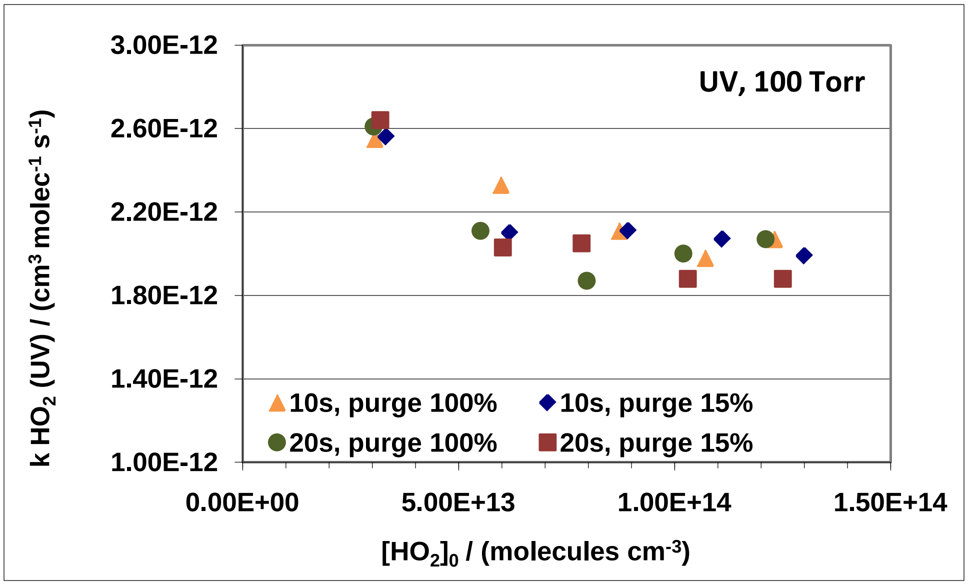

Figure 5-5. Initial radical dependence of the HO_2 self reaction observed by the UV. Concentrations < 5 x 10^{13} were influenced by other removal processes.

At concentrations < 5 x 10^{13} molecules cm^{-3} the $k_{HO2}(UV)$ increased for all of the flow conditions shown indicating that another removal process was important. This was not observed in **Figure 5-6** for $k_{HO2}(NIR)$.

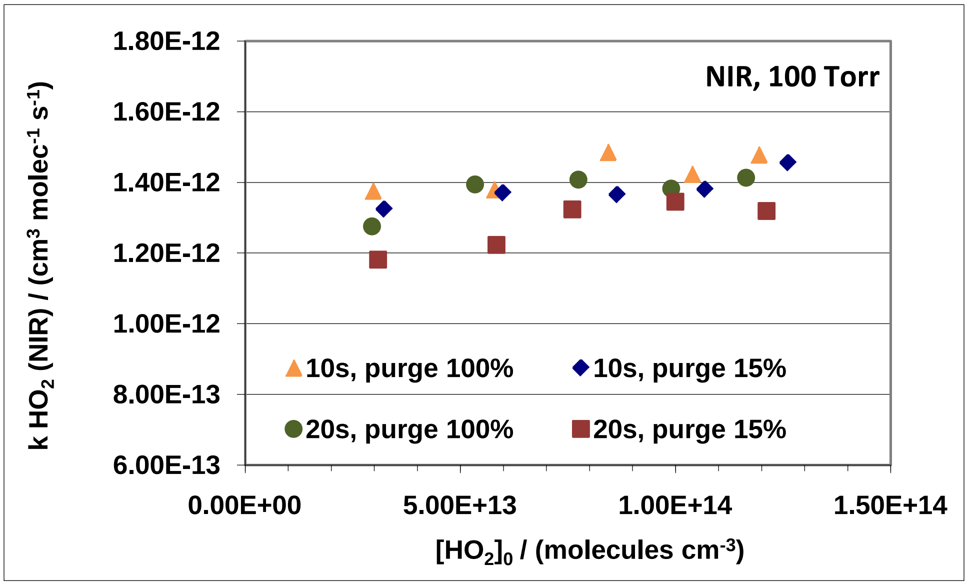

Figure 5-6. Initial radical dependence of the HO_2 self reaction observed by the NIR.

At much lower radical concentrations this was eventually seen in the NIR as well, but at those concentrations the UV signal-to-noise was very low so comparison was difficult. The pressure dependence of both $k_{HO2}(UV)$ and $k_{HO2}(NIR)$ are shown in **Figure 5-7**. The data were taken using the flow conditions determined by the absorption measurements to best contain the reactant flow in **Table 5-2**. The NIR behavior was not always consistent, but did show a dependence on pressure while the UV was consistently independent of pressure.

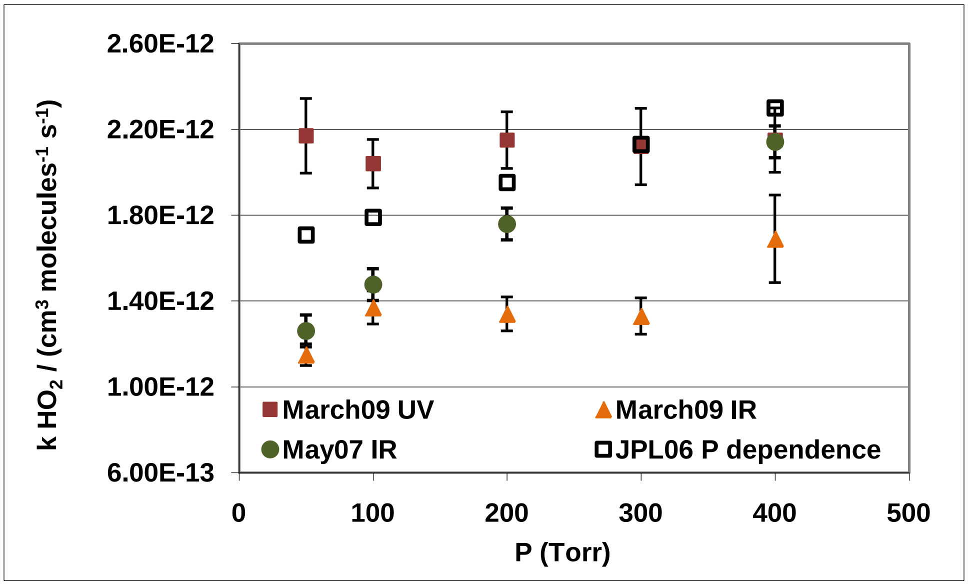

Figure 5-7. Pressure dependence of k_{HO2} in both the UV and NIR compared with the literature value. The NIR behaved differently at different times.

The lack of pressure dependence in the UV prompted further UV experiments that were done completely without purge gas. Similar to the flowing absorption cross section measurements of acetone, path length was physically fixed by the window – window distance of the reaction cell. These results, shown in **Figure 5-8**, did show pressure dependence. They also show a similar initial radical dependence to the 100 Torr measurements of $k_{HO2}(UV)$.

The UV setup was very straightforward due to the coalignment of the D_2 beam with the excimer laser. At first thought any deviations in the pressure dependence and behavior with radical concentration would be expected in the NIR, where the off-axis overlap could lead to more complicated behavior. By comparing the results in **Figure 5-7** and **Figure 5-8** it is clear that the presence of the purge flow must be what eliminated the observed pressured dependence. Without a purge the $k_{HO2}(UV)$ agrees very well with the literature. The comparison also shows that the behavior of $k_{HO2}(UV)$ at low radical is not related to the purge because it is present in both figures. One explanation is that removal by diffusion out of the D_2/excimer beam path is also a significant loss process at concentration < 5 x 10^{13} molecules cm^{-3}, but this will be discussed further in Section 5.3.2.

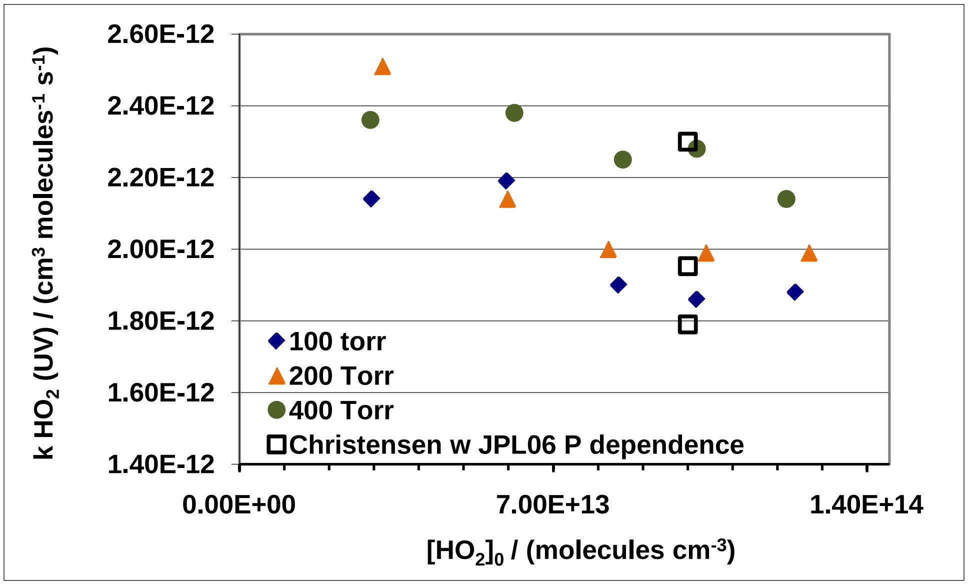

Figure 5-8. Pressure dependence of $k_{HO2}(UV)$ under conditions where no purge gas was used and the path length was fixed by the window – window distance.

Another issue was that the $k_{HO2}(UV)$ and $k_{HO2}(NIR)$ values at 100 Torr were different. The $k_{HO2}(UV)$ was somewhat high as shown because it was analyzed with the absorption path length determined from the CF_3Br etc. absorption measurements described above, i.e., 148 cm. However it may be that a “kinetics” path length was more appropriate for the analysis of the data. The kinetics path length was determined by fixing $k_{HO2}(UV)$ to the value measured in the non-purge case (where path length was known), and then fitting the path length. Path lengths determined in this way for the 100 Torr data were equal to ~ 138 cm. In these fits path length and $k_{HO2}(UV)$ are proportional so lowering one will lower the other. The kinetics path length agrees with measurements from the thesis of Dr. Christensen, which also used absorption measurements, but primarily relied on a kinetics determination to come up with a path length of 138 cm.[1]

Given the uncertain nature of the path length from the temperature probe observations, a kinetic path length may best measure the effective path length of the chemistry.

The low value of $k_{HO2}(NIR)$ was harder to explain and appeared to come from the off axis geometry of the NIR beam overlap with the radicals produced in the excimer laser. The off axis alignment means that as diffusion causes some molecules to leave the NIR beam path in the center it causes others to enter the beam path at the extremes where previously no radicals have been. This leads to an elongated path length at longer times and artificially higher signal at these times, i.e., it appears to slow the reaction down. To some extent it was sensitive to the alignment of the two lasers, as can be seen from the two different sets of pressure-dependent data. As expected it was not sensitive to the purge flow, unlike the UV, because the main overlap of the NIR laser with the excimer beam was in the center of the cell away from the purge regions. Further implications of the $k_{HO2}(UV)$ and $k_{HO2}(NIR)$ are discussed in Section 5.3.3 when discussing the CH_3OH effect on the HO_2 self reaction.

The NIR geometry effect also explained the lack of an $[HO_2]_0$ dependence for $k_{HO2}(NIR)$ over the same concentration range where there was one observed for $k_{HO2}(UV)$. This was handled in the fitting of the data by including a unimolecular loss term for the UV signal but not the IR. At the higher radical concentrations generally used for kinetics experiments this term had a negligible impact on fast reactions like the HO_2 self reaction, but was included for consistency. The determination of the unimolecular loss term is discussed next.

5.3.2 $RO_2 + RO_2$

RO_2 self reactions are considerably slower than the HO_2 self reaction and therefore more susceptible to interference from other loss processes. **Figure 5-9** shows the k_{obs} for the CH_3O_2 and $C_2H_5O_2$ self reactions plotted against the inverse of initial radical concentration. A clear linear dependence was observed unlike the $k_{HO2}(UV)$ data.

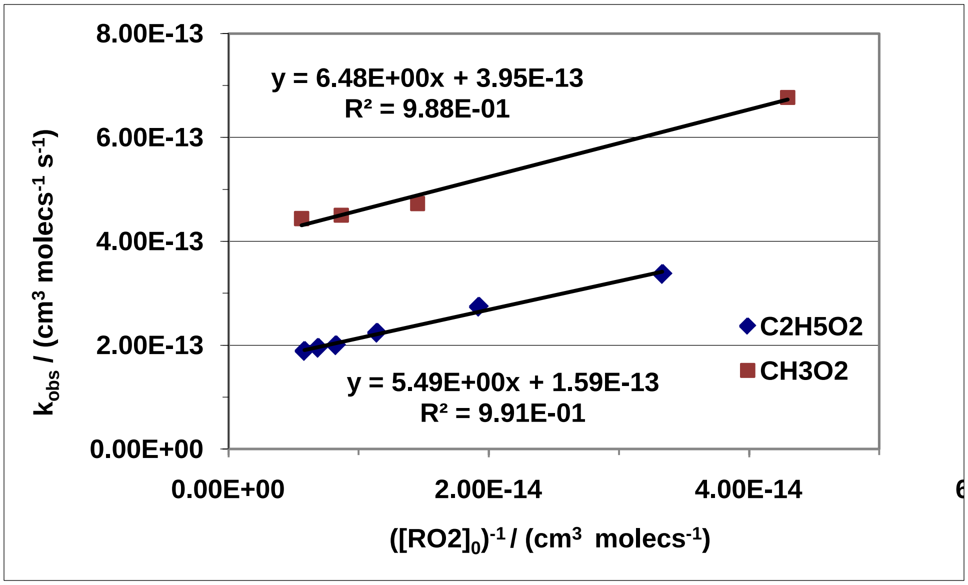

Figure 5-9. RO_2 self reaction dependence on initial radical concentration. A unimolecular diffusion loss was nonnegligible.

The initial radical dependence of the RO_2 self reactions was attributed to a larger impact from competing unimolecular loss, e.g., diffusion, because of the smaller k_{obs}. The effect of this loss was determined in two different ways. The kinetics of the RO_2 self reaction including a unimolecular loss term are described by equation (5.3).

$$\frac{d[\mathrm{RO_2}]}{dt} = -2k_{RO2}[\mathrm{RO_2}]^2 - k_D[\mathrm{RO_2}] \tag{5.3}$$

This chemistry was modeled by the FACSIMILE program,[8] but needed a fixed value of k_D. The model could not successfully fit both k_{RO2} and k_D without either returning unphysical values or determining that the data was not dependent on k_D. The IGOR software package was also used to fit the data using the analytical solution for bimolecular self reaction kinetics in equation (5.4).

$$\frac{1}{[\mathrm{RO_2}]_t} = \frac{1}{[\mathrm{RO_2}]_0} + 2k_{obs}t \qquad (5.4)$$

The fits and residuals from the data looked good indicating that the analytical solution adequately described the time dependence of the concentrations. However k_{obs} was not consistent with initial radical showing that all losses were not being described. The fact that FACSIMILE could not determine a dependence of the data on k_D, the analytical solution fit well, but k_{obs} was inconsistent suggested that the unimolecular loss had a small but non-negligible effect on the reaction. By assuming that the effect is small, an analytical method for determining k_D was used, based off of the work from Thiebaud et al,[9] and shown in equation (5.5). Unimolecular loss is approximated without disturbing the analytical solution in equation (5.4), except that the expression in parenthesis of (5.5) is equal to k_{obs}.

$$\frac{d[\mathrm{RO_2}]}{dt} = -2\left(k_{RO2} + \frac{k_D}{[\mathrm{RO_2}]_0}\right)[\mathrm{RO_2}]^2 \qquad (5.5)$$

Plotting k_{obs} vs. $([\mathrm{RO_2}]_0)^{-1}$ led to the linear fits seen in **Figure 5-9**, with k_D as the slope and k_{RO2} the intercept. FACSIMILE fits using the k_D from this method determined an identical k_{RO2} verifying the approximation of (5.5). The only exception was at some of the very lowest radical concentrations the points did not lay on the line. The low signal to noise in these cases made the data less reliable, and the increased importance of the diffusion loss meant the approximation in equation (5.5) was no longer valid.

The pressure dependence of the $C_2H_5O_2$ self reaction did not display the expected results. Similar to the HO_2 self reaction showing no pressure dependence when a positive dependence was expected, this reaction showed a negative pressure dependence when no dependence was expected. Unlike the HO_2 self reaction removing the purge gas did not change things. **Figure 5-10** shows the pressure and initial radical dependence under both purge and full cell condition for the $C_2H_5O_2$ self reaction. It appeared from this that unimolecular loss was of larger importance than any purge effects. The 100 and 200 Torr k_{obs} led to similar k_{RO2}, but the 50 Torr k_{RO2} was larger. As discussed in Chapter 2, adjusting the k_D value to scale with pressure, (e.g., scale the measured 50 Torr k_D = 5 s^{-1}, to a 100 and 200 Torr k_D of 2.5 and 1.25 s^{-1}, respectively) led to better agreement.

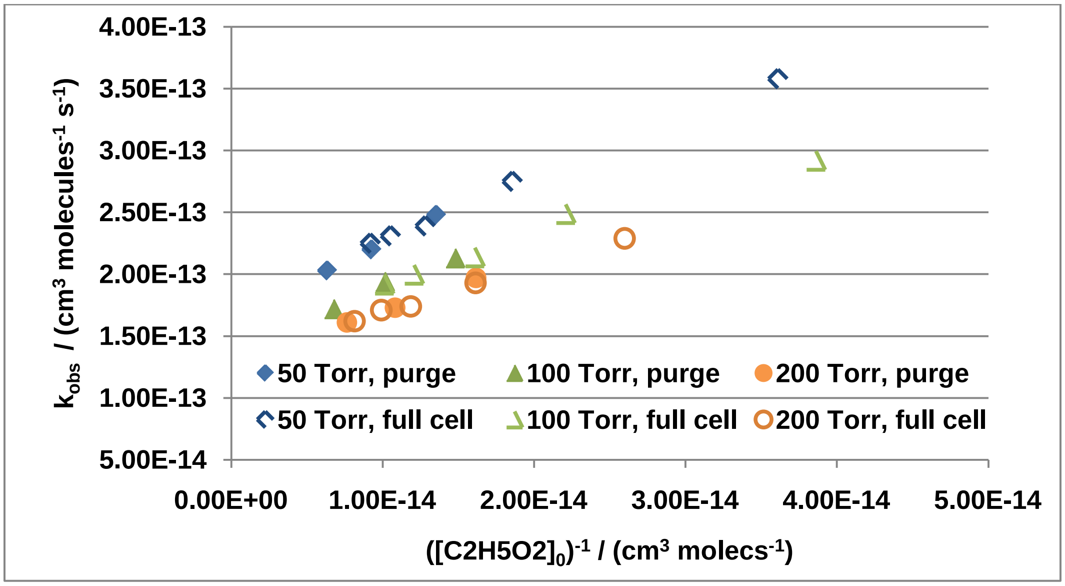

Figure 5-10. Pressure dependence of $C_2H_5O_2$ self reaction did not change with or without the purge gas.

The exact nature of the unimolecular loss, whether it is diffusion or due to a flow effect, is difficult to determine. In his thesis, Dr. Lance Christensen assigned the dominant loss to turbulent mixing as opposed to diffusion because of a dependence on the residence time of the flow.[1] In this work flow changes and faster residence times also appeared to be able to increase the apparent removal rate at both 100 and 200 Torr (but not their extrapolated k_{RO2} values), but further slowing of the flow did not change the 50

Torr data. One explanation is that there are flow effects that dominate at the higher pressures when diffusion is slower, hence the lack of reduction in measured k_D at higher pressure, but that at some point diffusion loss becomes comparable or greater than the flow loss at lower pressure. Pushing the upper limit of the radical concentration at higher pressure would show that it stops obeying equation (5.5), and reaches a constant value of k_{RO2} at a larger value than expected if the flow loss really is the culprit. Alternatively, the unimolecular loss may somehow be under predicted at 50 Torr leading to values of k_{RO2} that are too large, but as also previously mentioned in Chapter 2, increasing k_D above the values determined leads to worse fits to the data. Overall the combined unimolecular loss processes are well fit for the slower k_{RO2} measurements and have a negligible effect on the higher concentration k_{HO2} measurements.

5.3.3 HO_2 + HO_2 and the CH_3OH effect

The HO_2 self reaction was more complicated to study because of interference from the CH_3OH precursor chemistry. HO_2 was generated by the following reactions:

$$\mathrm{Cl_2} \xrightarrow{h\nu\ 308\ nm} \mathrm{2Cl} \tag{5.6}$$

$$\mathrm{Cl} + \mathrm{CH_3OH} \longrightarrow \mathrm{HCl} + \mathrm{CH_2OH} \tag{5.7}$$

$$\mathrm{CH_2OH} + \mathrm{O_2} \longrightarrow \mathrm{HO_2} + \mathrm{HCHO} \tag{5.8}$$

This chemistry worked very well because it generated only HO_2 and the stable products HCl and HCHO, except for one known problem, HO_2 and CH_3OH form a hydrogen bonded complex at low temperature. This complex increases the observed rate of the HO_2 self reaction and must be accounted for when trying to determine the actual rate coefficient of the self reaction for the atmosphere.[10-13]

$$\mathrm{HO_2 + HO_2 \xrightarrow{M} H_2O_2 + O_2} \tag{5.9}$$

$$\mathrm{HO_2 + CH_3OH \rightleftharpoons HO_2 - CH_3OH} \tag{5.10}$$

$$\mathrm{HO_2 + HO_2 - CH_3OH \longrightarrow H_2O_2 + O_2 + CH_3OH} \tag{5.11}$$

At higher concentrations of CH_3OH reaction of the complexes may occur or additional CH_3OH may complex with one HO_2, e.g., $HO_2 – (CH_3OH)_2$, as was discussed in Chapter 4 during the nucleation experiments.

The effect of the complex on the observed kinetics was also temperature dependent because the complex becomes much more heavily favored at low temperature. **Figure 5-11** shows the k_{HO2} values obtained while taking the data in for the $C_2H_5O_2$ system in Chapter 2. As just shown at room temperature the $k_{HO2}(UV)$ is a little bit larger than $k_{HO2}(NIR)$, but overall there was acceptable agreement until ~ 230 K. At low temperature $k_{HO2}(NIR)$ was much larger. In this regime the NIR and UV probes were starting to observe different overall kinetics due to the HO_2-CH_3OH complex. In the UV the complex absorption cross section is likely to be similar to the HO_2 absorption cross section because the absorption is a B←X transition of a non-bonding O atom electron not involved with the hydrogen bond of the complex. Therefore total HO_2 is seen in the UV. In the NIR the frequency of the O–H stretch overtone of the HO_2 will likely be shifted because the H atom helps form the complex, and would not be observed at the same wavelength as the uncomplexed HO_2. Total HO_2 is then not observed in the NIR. This could lead to a larger measured rate constant because the faster disappearance is wrongly attributed to the rate coefficient rather than the unseen additional concentration of radicals. The $k_{HO2}(UV)$ agree with the Christensen et al. values also measured by the UV in the same apparatus.[12] A complete and thorough data set reinvestigating the CH_3OH dependence of $k_{HO2}(UV)$ has not been completed, but after resolving the issue with the CH_3OH bubbler pressure and applying the temperature correction from the temperature probe experiments, the most recent $k_{HO2}(UV)$ CH_3OH dependence and zero CH_3OH values taken with Professor Fred Grieman were in agreement with the Christensen values.

One problem with the hypothesis that the NIR and UV are different because of the complex is the relatively small amount of complex predicted for the CH_3OH concentrations and temperatures in the values for **Figure 5-11**. Using the K_{eq} from the Christensen et al. work,[11] the amount of HO_2 in complex form from starting values of $[HO_2]_0 = 1.0 \times 10^{14}$ and $[CH_3OH] = 1.0 \times 10^{15}$ at 231 K, is ~ 5%. This seems like too small an amount to cause the divergence in $k_{HO2}(UV)$ and $k_{HO2}(NIR)$ observed.

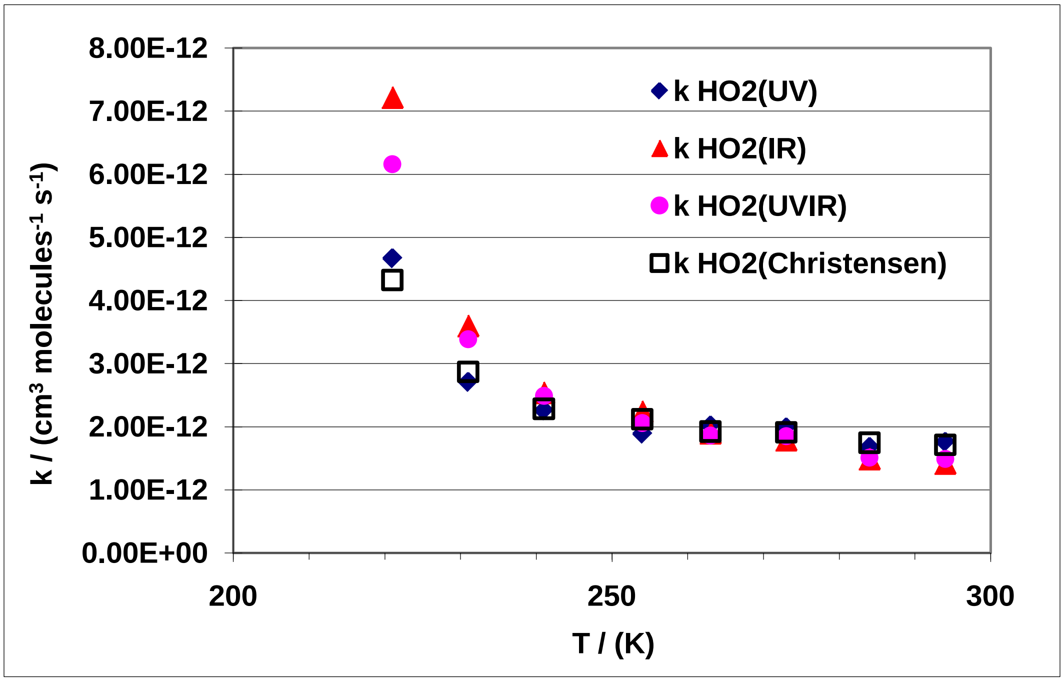

Figure 5-11. A comparison of the different k_{HO2} values from the work in Chapter 2 depending on whether the UV, IR, or UV and IR together were fit.

Work from other labs has measured a larger dependence on temperature for k_{HO2} actual than was measured by Christensen et al. in this lab.[12-14] A careful examination of the $k_{HO2}(NIR)$ would be interesting because of the stronger dependence on temperature just described. Purge flow might contribute to the differences between the NIR and UV because as also discussed the purge does not affect $k_{HO2}(NIR)$, but does affect $k_{HO2}(UV)$. The purge interference could be especially problematic at low temperature where the gas mixing regions will react more slowly because they are at higher temperature, thus potentially causing $k_{HO2}(UV)$ to appear lower than it actually is.

A simulation to test for a purge influence on $k_{HO2}(UV)$ was attempted based on the mixing profile measured using the temperature probe. The simulation was done in the following way: First, linear mixing of the room temperature purge (296 K) and the cold reactant gas (213K) was assumed to be responsible for the temperatures measured in the mixing region. The amount of each flow was assumed proportional to the temperature mixing, i.e., $T_{meas} = T_{room}*X + T_{cell}*(1-X)$, where X is the fraction of purge in the mixture. Using these fractions and a typical HO_2 initial of 7×10^{13} molecules cm^{-3} in the pure reactant flow, the appropriate fractional-initial concentrations in the mixing regions were determined. A FACSIMILE simulation of the HO_2 self reaction at each initial concentration was then run. Each of these simulations (HO_2 time profiles) was then multiplied by the HO_2 cross section and the path length over which that fraction exists to come up with an absorbance. The path length was determined by the spacing between temperature measurements, so it was somewhat arbitrary. However in the mixing regions measurements were generally made every 1–2 cm leading to a reasonably fine grid within the rapidly changing region. A similar procedure was followed for the H_2O_2 product and was added into each absorbance. All the absorbances for the entire cell path length were then added together to form a simulated HO_2 absorbance trace, and then fit using the standard model like conventional data. This was done for 100 Torr and 300 Torr at room temperature and 100 Torr at 213 K. (In the 213 K case the only additional difference was that the rate coefficient at each fraction was also adjusted for the temperature at that fraction). The results are shown in **Table 5-3**. The simulations predict a clear lowering of the measured $k_{HO2}(UV)$ value at low temperature, and this value was not far from the value that would be extrapolated from the Christensen et al. measurements. On the other hand the simulation showed that although both 100 and 300 Torr would be lower than expected a clear pressured dependence would still exist. This was not observed in the actual experiment, leaving questions about the usefulness of the simulations given that they were not clearly validated by the measurements.

Table 5-3. Simulation of purge effect on $k_{HO2}(UV)$ at low temperature and high pressure.

T (K)	P (Torr)	CH_3OH (molecules cm^{-3})	$k_{HO2}(UV) / 10^{-12}$		
			Input	Output	Measured
298	100	2.00×10^{15}	1.78	1.57	1.70
298	300	2.00×10^{15}	2.09	1.83	1.80
213	100	2.00×10^{15}	3.48†	2.74	2.48*

* Extrapolated from the Christensen et al. value. †Taken from JPL06 recommendation.

In addition, the temperature dependent work for the $C_2H_5O_2 + HO_2$ reaction in Chapter 2 was in agreement with the literature, which suggests that the purge mixing might contribute only a small error to the overall kinetics. A final note on the $k_{HO2}(UV)$ and $k_{HO2}(NIR)$ comparison is that the $k_{HO2}(NIR)$ value was always dependent on the UV probe for it absolute calibration. This makes it difficult to totally separate the analysis when comparing trends. Two ways this might become relevant are through a greater than expected temperature dependence of the HO_2 UV cross section, or a greater than expected shift in the HO_2–CH_3OH complex cross section. Both would affect the amount of $[HO_2]_0$ and the NIR calibration.

5.4 Summary of path length, pressure dependence, and CH_3OH effect

A number of experiments were carried out to better determine the effect of the flow conditions on the observed kinetics of HO_2 and RO_2 reactions. The calculated concentrations of the flow system have been verified by absorption measurements although the nature of the absorbing molecule (i.e., how sticky it is) will determine whether an absorption path length of 150 or 160 cm is correct for measuring concentration by absorbance. The most reliable flow conditions for containing the reactant flow were 100 Torr, 10 s residence time, and 100% purge. Cl_2 absorption (a good estimate of the true reactant path length because Cl_2 was the radical precursor) under these conditions had a path length of 150 cm, but kinetic determinations of the path length agreed with the 138 cm value determined previously. At this point an average of the two values, or simply the kinetics value, may be most appropriate.

The $k_{HO2}(UV)$ was also sensitive to purge and path length issues when examining the pressure dependence, but the unimolecular loss effects at low radical concentration occurred with or without purge. The disagreement between $k_{HO2}(UV)$ and $k_{HO2}(NIR)$ at low temperature may be accounted for by the spectroscopy of the HO_2-CH_3OH complex, but there may also be an effect due to the mixing region influencing the UV.

For the slower RO_2 self reaction k_{obs} was affected by unimolecular loss regardless of purge flow, but some residence time effects were also observed. The k_D measured did not show the expected dependence on pressure that a pure diffusion term would, leaving some uncertainty in the cause of the loss. A unimolecular loss term that is a combination of diffusion and flow losses, the dominant loss depending on the regime of the flow, would describe the observed behavior.

5.5 NIR probe

The primary work of the IRKS apparatus has been kinetics measurements of RO_2 reactions by combining the sensitivity and specificity of the NIR probe with the absolute absorbance measurements of the UV probe. Spectroscopic measurements that took advantage of the sensitivity of the NIR probe were also possible. In this work the identification of molecular species and the optimization of the wavelength modulation (WM) signal were done by looking at the NIR spectroscopy. Other experimental noise issues in the NIR probe were also addressed.

5.5.1 NIR wavelength modulation setup

The NIR probe was a 1.5 μm distributed feedback diode laser made by the JPL microdevices laboratory. A 30 pass Herriott cell increased the path length of the NIR probe, shown schematically in **Figure 5-1**, and led to greater signal. WM spectroscopy was used to reduce the signal noise by allowing detection of the absorbance signal at higher frequency away from low frequency noise sources, and by measuring at a smaller overall bandwidth. The electronics of this system were setup by Dr. Lance Christensen and fully described in his thesis.[1] **Figure 5-12** shows the configuration of the electronics during the work of this thesis.

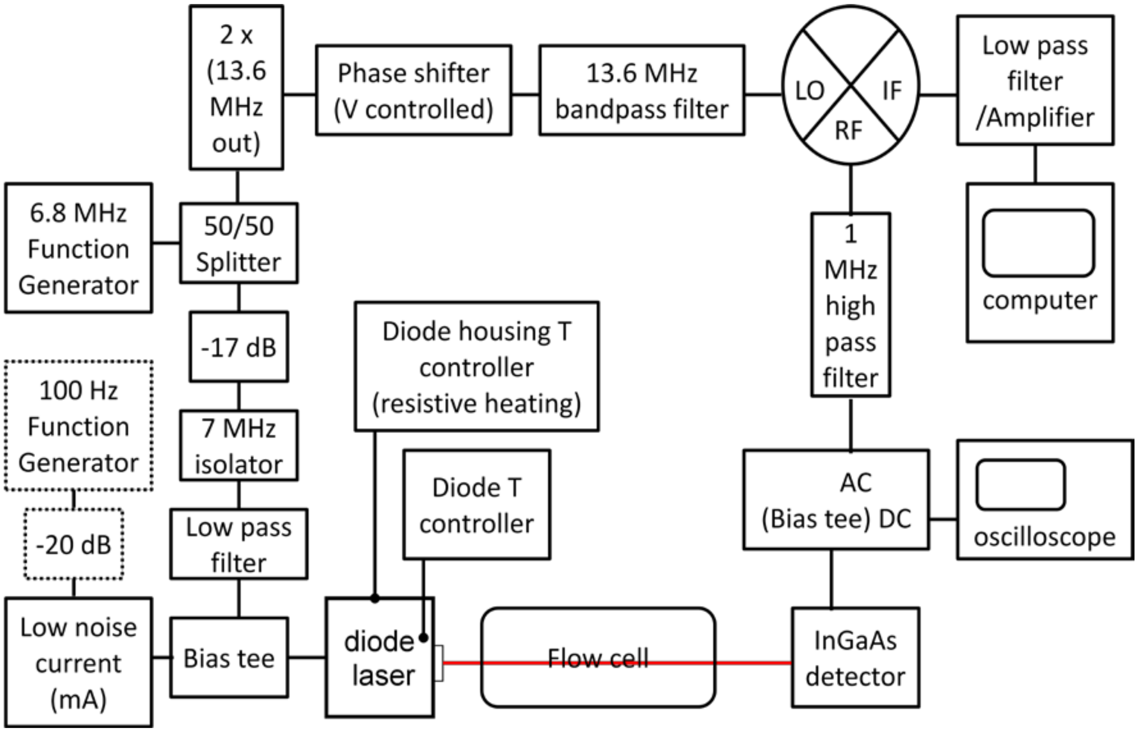

Figure 5-12. Diagram of the wavelength modulation setup for the NIR diode laser

The diode laser input current was modulated by at 6.8 MHz and the 2f signal was detected at 13.6 MHz. A 6.8 MHz, 10 Vpp, sine wave from a function generator (Agilent 33120A) was split (Mini-Circuits ZFSC-2-6), attenuated (Mini-circuits, various fixed attenuators), sent through a 7 MHz isolator (unknown manufacturer), and a low pass filter (Mini-Circuits SLP-5) before joining the DC current from the low noise current supply (ILX-Lightwave 3620) at a bias tee. The other half of the signal was doubled to 13.6 MHz (Mini-Circuits MK-3), phase shifted (Mini-Circuits SPH-16+) so that the signal at the mixer would be 90° out of phase with the original signal, and then sent through a 13.6 MHz bandpass filter (TTE KC4-13.6M) before ending at the LO of the mixer (Mini-Circuits ZFM-3+). Absorption in the flow cell converted the wavelength modulation of the diode laser to an amplitude modulation at the detector (New Focus 1811). A bias tee (Mini-Circuits PBTC-1GW) then removed the DC signal for monitoring on an oscilloscope (Tektronix TDS 3054) and sent the AC signal to the mixer after passing through a high pass filter (TTE H93-1.0M). The output of the mixer was low pass filtered and amplified by a factor of 100 (SR560), and then the signal was sent to the computer. The low pass filter setting was determined by the data acquisition program and experimental conditions described in Section 5.1. For spectroscopy experiments a function generator (SRS DS340) was also used to ramp the current of the diode current source at 100 Hz, shown as dashed boxes in **Figure 5-12**.

5.5.2 HO_2 spectroscopy

Spectroscopy of HO_2 in the NIR has been looked at by a number of groups. Rovibrational lines in the A←X electronic transition have been investigated mainly in the 1.4 μm region.[15-18] The overtone of the O – H stretch ($2\nu_1$) was mapped out in work by Tuckett et al. and DeSain et al.[19,20] Line strengths in this region were also investigated by a number of groups primarily for use in kinetics studies.[9,11,21,22] The strongest transition observed so far is at 6638.2 cm^{-1}, the frequency used for detection of HO_2 in this apparatus. Frequency calibration of the NIR laser was done with a wavemeter borrowed from Dr. Pin Chen at JPL, and by comparison of the observed spectrum with a spectrum provided in a private communication by Dr. John DeSain at Sandia National Lab. **Figure 5-13** shows the observed HO_2 spectra as it changed in time at 6638.2 cm^{-1}, under the conditions $[HO_2]_0 \sim 9 \times 10^{13}$ molecules cm^{-3} and total pressure of 100 Torr. The data here has been divided by the background trace, shown in the figure as being taken in negative time. Without dividing the data by the background trace a sloping background was observed, partially due to the change in diode laser power with current. The background also appeared to be somewhat dependent on the alignment of the Herriott cell because it changed from day to day.

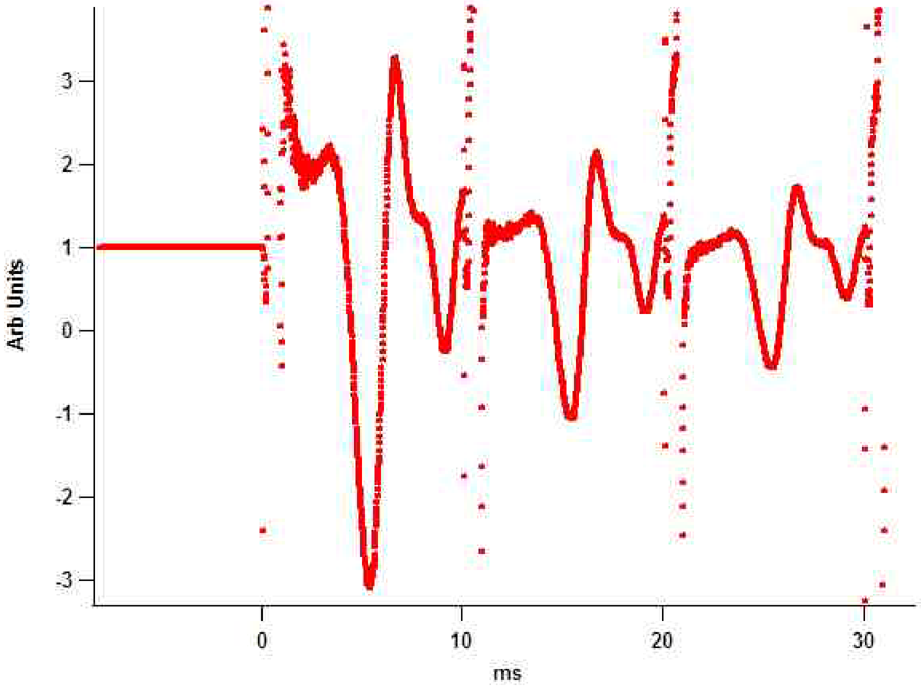

Figure 5-13. HO_2 spectrum after background ratio. The HO_2 self reaction reduces the signal as the scans are taken at progressively longer times after the excimer pulse. Two peaks are observed along with the characteristic 2f lineshape.

At certain alignments an etalon was the dominant source of noise in the spectroscopic experiments. In these cases adding a slight vibration (a foam damped personal foot massager was used as the vibration source) to one of the beam optics was found to reduce the noise from the etalon. A neutral density filter placed in front the detector to reduce the NIR beam power was also found to increase this etalon if placed perfectly perpendicular to the detector.

5.5.3 NH_3, CH_3CHO and C_2H_5OH

Spectra of ammonia (NH_3), acetaldehyde (CH_3CHO), and ethanol (C_2H_5OH) were all taken in the NIR as well. NH_3 came in pure form from a lecture bottle and its flows were monitored using a mass flow controller. CH_3CHO/N_2 gas bulb mixtures were prepared on a vacuum line after freeze/pump/thaw purification of 95% pure CH_3CHO. The presence of pure CH_3CHO in the bulb was verified by using FTIR spectroscopy on a small sample from the bulb. Nitrogen bubbled through liquid C_2H_5OH held at 0 °C (V.P. 11.7 Torr) delivered C_2H_5OH to the cell. Concentrations in molecules cm^{-3} for each species were $[NH_3] = 1 \times 10^{14} – 4.5 \times 10^{16}$, $[CH_3CHO] = 1 \times 10^{14} – 3.0 \times 10^{16}$, and $[C_2H_5OH] = 3.5 \times 10^{15} – 3.5 \times 10^{16}$. In each case the laser current was scanned over ~ 15 mA which corresponded to ~ 0.75 cm^{-1}. Data acquisition was done directly with the digital oscilloscope since the excimer laser was not needed. Each scan was averaged 128 times.

The NH_3 work was undertaken as a frequency calibration. Strong lines were observed but the spectrum appeared congested and hard to interpret. Frequency calibration was then done using the wavemeter as already discussed. The confusing spectra were due to the fact that the modulation depth of the WM electronics was too large so individual transitions were being blended together. The modulation depth was corrected while observing the HO_2 spectra. No further work on NH_3 was done, but there are strong lines within the tuning of the diode laser bandwidth if needed in the future.

Measurements of CH_3CHO and C_2H_5OH were made to determine if either had an absorption that would interfere with HO_2 detection because both are products from the $C_2H_5O_2$ work in Chapter 2. No lines were observed within the tuning range even at concentrations as high as ~ 1 Torr.

5.5.4 NIR Baseline work

The NIR signal had an alignment-dependent baseline problem when following reactions for many milliseconds. Work investigating faster time scale processes such as the forward rate of the HO_2 – CH_3OH equilibrium constant was not affected by this, but longer time scale measurements of RO_2 self reactions were susceptible to interference. **Figure 5-14** shows this baseline problem for a HO_2 self reaction experiment. The dip was clearly related to the interaction of the excimer and diode laser beams as evidenced by the stable pre-photolysis baseline. Adjusting the Herriott cell alignment made it possible to achieve a stable baseline, but unfortunately no reproducible alignment procedure for removing the baseline was established.

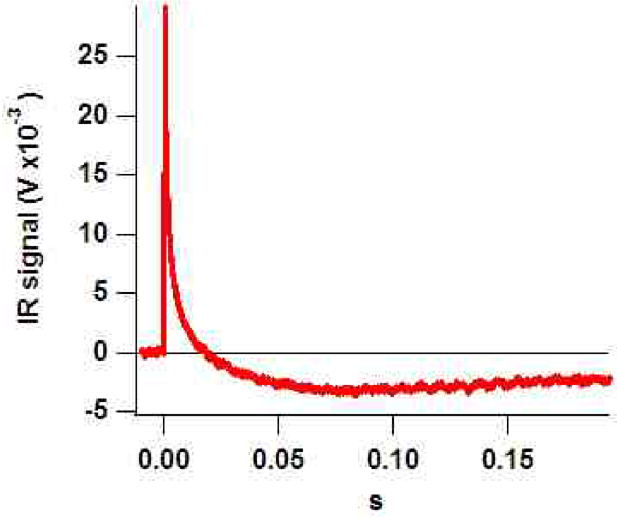

Figure 5-14. Baseline dip in HO_2 + HO_2 chemistry

An examination of the DC signal from the detector shows unequivocally the relationship between the NIR problems and the excimer laser. **Figure 5-15** shows two DC signals, one with only Cl_2 and O_2 and the other where ethane was also added to the mix. In both cases ringing in the signal can be observed, but it was even larger with ethane added. It appears that the exothermic initiation chemistry contributes to the coupling seen. This ringing could also sometimes be observed in the WM signal, depending again on the alignment of the Herriott cell. The ringing occurred consistently at a frequency very close to 8 kHz. In fact this 8 kHz signal never completely disappeared, but with the correct alignment it was reduced to levels where other sources of noise dominated.

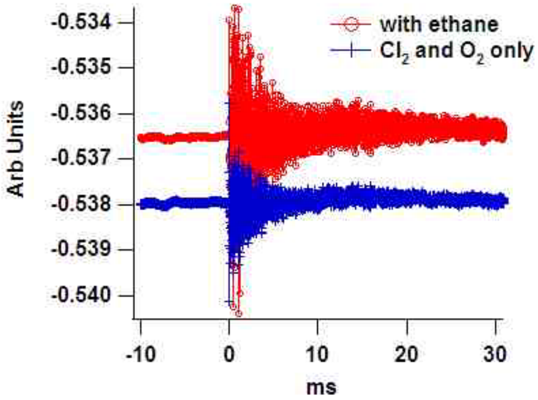

Figure 5-15. DC signal from the detector after the excimer fires. Energy released during the chemistry increases the noise, as can be seen by the larger noise when ethane was added to Cl_2 and O_2 mixtures.

When looking at the small secondary HO_2 signal from the $C_2H_5O_2$ self reaction it was critical that a stable baseline exist; it was unavoidable that the alignment always contained a bit of luck, but a straightforward diagnostic was possible. Because the source of the problem was the interaction of the excimer, the diode laser, and the chemistry it was likely that the dip was not wavelength dependent over the small tuning range of the laser. This allowed closer scrutiny of the baseline by tuning the laser off the HO_2 absorption line where no signal interference would occur. This was especially important because it allowed investigation of the baseline with the full chemistry in the cell which clearly led to larger noise in the DC signals of **Figure 5-15**. The "off HO_2 line" trace in **Figure 5-16** is an example of a good baseline signal that was measured by tuning the diode laser off the HO_2 absorption line. More traces at other wavelengths displayed similar baselines verifying the assumption that wavelength changes would not change the baseline. Using this technique the criteria determined for a good alignment were that the baseline remain stable throughout the post photolysis time period, and that it not shift more than 500 μV.

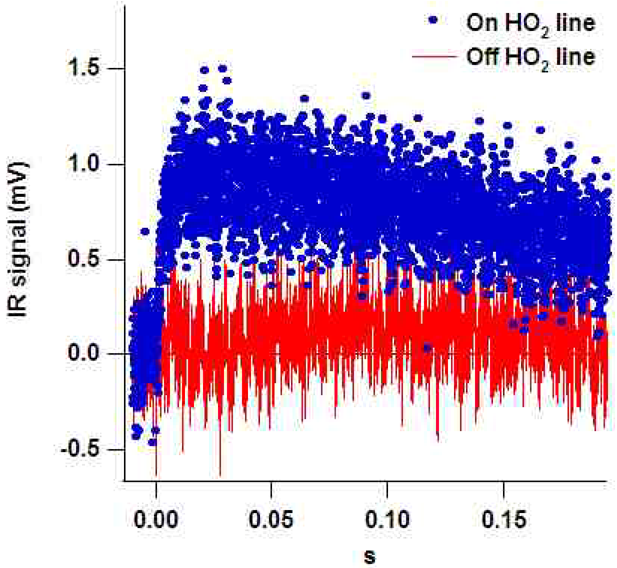

Figure 5-16. A signal is evident at the HO_2 frequency with only Cl_2 and O_2 present. A good baseline is also shown, determined by looking at its behavior while not on the HO_2 absorption line.

Also shown in **Figure 5-16** is the signal observed when only Cl_2 and O_2 are present in the cell and the laser is tuned to the HO_2 line. A real signal, not a baseline change, was observed. The species responsible was not known, but the signal was phase dependent indicating an actual absorption. This interference was initially mistaken for a baseline problem, and was another reason it was necessary to observe the baseline at a frequency other than the HO_2 line.

In general the quality of the WM signal was highly dependent on the alignment of the Herriott cell. The WM signal root mean square noise (RMS), the long time scale baseline, 8 kHz noise signal, and the stability of the DC signal all were sensitive to optical alignment of the Herriott cell. With patience good quality signals in all categories simultaneously were possible.

5.6 Sensitivity of UV and NIR probes

The minimum detectable absorbance per Hz$^{1/2}$ (md$A$ Hz$^{-1/2}$) for the UV and NIR probes allows comparison of the probes detection sensitivities. In the UV this was straightforward because absorbances are directly measured. The RMS noise of the UV absorbance signal taken with a 10 kHz bandwidth was ~ 2.8 x 10^{-3}. Using a signal to noise ratio (SNR) of 2 leads to md$A$ Hz^{-12} = 5.5 x 10^{-5}. The calculation in the NIR required a few approximations because the WM modulation signal was not an absolute absorbance. NIR signals were converted to concentration by a daily calibration in comparison to the absolute concentration measured by the UV. A simultaneous fit to the UV and IR time traces for the HO_2 self reaction chemistry allowed a voltage multiplier (VM) calibration factor to be established that converted the NIR signal in V to concentration in molecules cm^{-3}. The RMS noise of the NIR signal taken with a 10 kHz bandwidth was 2.47 x 10^{-4} V. Using a 100 Torr VM = 3.6 x 10^{14} molecules V^{-1} cm^{-3}, an estimated NIR path length of 2700 cm, and an estimated absorption cross section of 4 x 10^{-20} cm^{2}, the md$A$ Hz$^{-1/2}$ = 1.9 x 10^{-7} (Cross section and path length estimates come from Christensen et al.[2]). For day-to-day work with the apparatus the most straightforward diagnostic of the quality of the NIR signal was the VM. Due to pressure broadening of the line, sensitivity was almost directly proportional to pressure, i.e., a VM = 1.8 x 10^{14} molecules V^{-1} cm^{-3} at 50 Torr scales to VM = 3.6 x 10^{14} molecules V^{-1} cm^{-3} at 100 Torr. In general the signal in the NIR was good if VM • 4.0 x 10^{14} molecules V^{-1} cm^{-3} was measured at 100 Torr.

5.7 References

(1) Christensen, L. Laboratory studies of atmospherically important gas-phase peroxy radical reactions. , California Insitute of Technology, 2003.

(2) Christensen, L. E.; Okumura, M.; Sander, S. P.; Friedl, R. R.; Miller, C. E.; Sloan, J. J. *Journal of Physical Chemistry A* **2004**, *108*, 80.

(3) Keller-Rudek, H., Moortgat, Geert K. MPI-Mainz-UV-VIS Spectral Atlas of Gaseous Molecules, 2009.

(4) Sander, S. P.; Finlayson-Pitts, B. J.; Friedl, R. R.; Golden, D. M.; Huie, R. E.; Kolb, C. E.; Kurylo, M. J.; Molina, M. J.; Moortgat, G. K.; Orkin, V. L.; Ravishankara, A. R. "JPL 2006: Chemical Kinetics and Photochemical Data for Use in Atmospheric Studies, Evaluation No. 15, JPL Publication 06-2, Jet Propulsion Lab," 2006.

(5) NIST Chemistry WebBook, http://webbook.nist.gov/chemistry/, 2009.

(6) Cantrell, C. A.; Zimmer, A.; Tyndall, G. S. *Geophysical Research Letters* **1997**, *24*, 2195.

(7) Creasey, D. J.; Heard, D. E.; Lee, J. D. *Geophysical Research Letters* **2000**, *27*, 1651.

(8) FACSIMILE; 4.0.36 ed.; MCPA Software Ltd. 2002.

(9) Thiebaud, J.; Crunaire, S.; Fittschen, C. *Journal of Physical Chemistry A* **2007**, *111*, 6959.

(10) Andersson, B. Y.; Cox, R. A.; Jenkin, M. E. *Int. J. Chem. Kinetics* **1988**, *20*, 283.

(11) Christensen, L. E.; Okumura, M.; Hansen, J. C.; Sander, S. P.; Francisco, J. S. *Journal of Physical Chemistry A* **2006**, *110*, 6948.

(12) Christensen, L. E.; Okumura, M.; Sander, S. P.; Salawitch, R. J.; Toon, G. C.; Sen, B.; Blavier, J. F.; Jucks, K. W. *Geophysical Research Letters* **2002**, *29*.

(13) Stone, D.; Rowley, D. M. *Physical Chemistry Chemical Physics* **2005**, *7*, 2156.

(14) Tyndall, G. S., Orlando J. J., Personal communication.

(15) Fink, E. H.; Ramsay, D. A. *Journal of Molecular Spectroscopy* **1997**, *185*, 304.

(16) Freedman, P. A.; Jones, W. J. *Journal of the Chemical Society-Faraday Transactions Ii* **1976**, *72*, 207.

(17) Hunziker, H. E.; Wendt, H. R. *Journal of Chemical Physics* **1974**, *60*, 4622.

(18) Kanno, N.; Tonokura, K.; Tezaki, A.; Koshi, M. *Journal of Molecular Spectroscopy* **2005**, *229*, 193.

(19) DeSain, J. D.; Klippenstein, S. J.; Miller, J. A.; Taatjes, C. A. *Journal of Physical Chemistry A* **2003**, *107*, 4415.

(20) Tuckett, R. P.; Freedman, P. A.; Jones, W. J. *Molecular Physics* **1979**, *37*, 379.

(21) Johnson, T. J.; Wienhold, F. G.; Burrows, J. P.; Harris, G. W.; Burkhard, H. *Journal of Physical Chemistry* **1991**, *95*, 6499.

(22) Taatjes, C. A.; Oh, D. B. *Applied Optics* **1997**, *36*, 5817.